9-2021

Characterization of Anisotropic Materials using Scattered Field Measurements

Hirsch M. Chizever

CHARACTERIZATION OF ANISOTROPIC MATERIALS USING SCATTERED FIELD MEASUREMENTS

DISSERTATION

Hirsch M. Chizever

AFIT-ENG-DS-21-S-004

DEPARTMENT OF THE AIR FORCE
AIR UNIVERSITY

AIR FORCE INSTITUTE OF TECHNOLOGY

Wright-Patterson Air Force Base, Ohio

AFIT-ENG-DS-21-S-004

CHARACTERIZATION OF ANISOTROPIC MATERIALS USING SCATTERED FIELD MEASUREMENTS

DISSERTATION

Presented to the Faculty

Department of Electrical Engineering

Graduate School of Engineering and Management

Air Force Institute of Technology

Air University

Air Education and Training Command

In Partial Fulfillment of the Requirements for the

Degree of Doctor of Philosophy in Electrical Engineering

Hirsch M. Chizever, B.S.E.E., M.S.E.E., Th.M.

September 2021

AFIT-ENG-DS-21-S-004

CHARACTERIZATION OF ANISOTROPIC MATERIALS USING SCATTERED FIELD MEASUREMENTS

DISSERTATION

Hirsch M. Chizever, B.S.E.E, M.S.E.E., Th.M.

Committee Membership:

Dr. Peter. J. Collins
Chair

Dr. Michael. J. Havrilla
Member

Dr. William. P. Baker
Member

Dr. Adedeji B. Badiru
Dean, Graduate School of Engineering and Management

AFIT-ENG-DS-21-S-004

Abstract

The ability to synthesize designer anisotropic materials using additive manufacturing techniques has exceeded the capabilities of many traditional material characterization methods. Such methods require precision machining of samples to exploit incident field configurations to be used in conjunction with tailored measurement fixtures. This machining process may cause structural damage for some candidates, while for others it may alter their anisotropic properties. In addition, traditional schemes are limited in their ability to provide sufficient independent data for anisotropic estimation. A free space method of material characterization that exploits far-zone scattered fields as a function of frequency, illumination angle, and polarization provides independent information not available from traditional methods.

This research uses monostatic far-zone scattered field measurements to estimate the permittivity of anisotropic materials at X-band. In contrast with traditional subsample illumination methods, this effort examines the efficacy of whole-sample transverse electromagnetic (TEM) illumination in the estimation of anisotropic permittivity using radar cross section (RCS) measurement techniques. The research examines the impact that dielectric supports have on measurement error and uncertainty in permittivity estimates. The research follows an incremental approach, first demonstrating successful estimation of permittivity for isotropic spheres followed by a Teflon isotropic cube. The method is then applied to uniaxial and biaxial cubes with an estimated permittivity that is validated through comparisons with published data.

The method showed success for a material with high contrast between tensor axes but had increased uncertainty with materials of low real and imaginary permittivity. The research also indicated that uncertainty increases in lower loss tangent estimates due to mutual coupling between the dielectric support structure and the material under test. Finally, the method demonstrated that estimates of lossy biaxial permittivity is possible in a free space far-field context without the use of costly measurement facilities or complex hardware.

To Him who is able to keep me from stumbling…

Acknowledgments

I would like to thank Dr. Peter Collins, Dr. Michael Havrilla, and Dr. William Baker for their extended patience, kindness, and counsel as I wrestled with my research amidst the unforgiving realities of life. I want to offer my heartfelt thanks to the following friends and colleagues who made this work possible: Dr. Alexander Knisely whose willingness to make his research data available to me was a tremendous help; Dr. Tri Van for his help in understanding the physics of scattering and for making computational electromagnetics accessible to the masses; Dr. Gregory Wilson who continues to teach me the unyielding laws of mathematics; Dr. Peter Munk for making electromagnetics theory look easy; Dr. Brian Kent, Dr. Leanne Young, and Dr. Eduardo Moas who made it possible for me to take time away from my duties to focus on my research; Mr. Dave Kuhl for his machining acumen and willingness to give me all I needed from his shelves at DaveWave; and Ms. Amy Stiffler whose technical writing and editing capabilities were indispensable. A special thanks to Applied Research Associates for use of their state-of-the-art measurement facilities and numerous computational electromagnetics codes. Finally, there are no words I can give to my wife who endured my absence in mind and body for so long and whose love and confidence gave me the courage and motivation to complete this journey; and to my sons, both here and in glory, your presence in my life brings me unspeakable joy.

Hirsch M. Chizever

Table of Contents

Abstract iv

Acknowledgments vii

List of Figures x

List of Tables xviii

I. Introduction 1

1.1 Problem Statement 1
1.2 Scope and Research Goals 4
1.3 Limitations and Challenges 10
1.4 Resource Requirements 10
1.5 Organization 11

II. Background and Motivation 12

2.1 Isotropic Permittivity Estimation using RCS Measurements 13
2.2 Anisotropic Permittivity Estimation using RCS Measurements 18
2.3 Motivation 18

III. Methodology 20

3.1 Free Space Permittivity Estimation using Spheres 20

Sphere Scattering Review 21
Measurement Configuration and Calibration 23
Sphere Permittivity Estimation. 44
Explanation of Sphere Results. 45
Uncertainty Considerations for Spheres. 49
Sphere Permittivity Summary 51

3.2 Estimation of Permittivity using Dielectric Cubes 51

Legacy and Traceability with Prior Work. 58
Use of FEKO as a Forward Solver. 59
Range Configuration and Calibration 59
Measurement and Inversion Methodology 62
Permittivity Estimation Summary 63

IV. Results and Analysis 65

4.1 Measured Scattered Field Comparisons 65

The Use of Measured Phase in Inversions 69
Isotropic Teflon Permittivity Estimate 72
Uniaxial Low Contrast Permittivity Estimate. 73
Uniaxial High Contrast Permittivity Estimate. 77
Biaxial Low Contrast Permittivity Estimate 79

4.2 Summary of Results 80
4.3 Uncertainty Considerations 82

Target-Mount Coupling Errors 83
Root Mean Square Error Estimate 85
Error Comparison with Focused Beam System 91

V. Conclusion 95

5.1 Discussion 95
5.2 Future Work 97

Appendix: Inversion Convergence History 99

Bibliography 101

List of Figures

Figure **Page**

1. Map of common dielectric measurement techniques spatially distributed according to material category, specimen preparation, fixture type, and accuracy [6]. Note: a dark blue oval and accompanying blue text have been added to the graphic indicating the efficacy of the proposed method within the greater context of material characterization techniques. 3

2. Comparison of dielectric measurement techniques as a function of complex permittivity and frequency [7]. Note: fonts with white backgrounds have been added for presentation purposes. 4

3. Available target illumination choices. Monostatic far-field illumination (top left), monostatic near-field illumination (top right), bistatic far-field illumination (bottom left), and bistatic near-field illumination (bottom right). 9

4. Dielectric cubes used in research, each having a side 22.86 mm: (1) Teflon/Solid: Isotropic – no contrast, (2) Nylon/Low Loss Occlusions: Uniaxial - Low Contrast, (3) Nylon/Air Occlusions: Biaxial – Low Contrast, and (4) Nylon/ESD-PETG Occlusions: Uniaxial - High Contrast. 10

5. Biaxial Knisely Cube unit cell orientations with respect to incident field. For all orientations shown, the incident field originates from Port 1 (Knisely, 40). 15

6. 3D printed homogeneous isotropic sphere comprised of dielectric cylinders in a triangular patch format (Saleh [30]) 17

7. Normalized RCS ($\sigma/\beta_0 a$) comparison between PEC sphere and Teflon sphere as a function of free space $\beta_0 a$. 23

8. Teflon sphere mounted on low density foam structure (foreground) with broadband feed antenna (background). Mylar tape used for stability to prevent background movement upon sphere removal. 24

9. Linear Systems representation of an RCS measurement system. The top diagram represents the corruption of the uncorrupted target scattered field caused by the system response resulting in the measured target scattered field. The bottom diagram represents the corruption of

the uncorrupted reference scattered field caused by the same system response resulting in the measured reference scattered field. 27

10. Computed RCS (left) and far-zone scattered field phase (right) for a 190.5 mm diameter calibration squat cylinder. 28

11. Sphere RCS measurement configuration and error source identification. Blue represents range hardware or structure. Green represents sphere and desired scattered field. Red represents undesired signals: transmit-receive coupling through broadband circulator, antenna mismatch at feed point, antenna mismatch at antenna – free space interface, sphere-foam mount scattered field, and side and back wall absorber scattered field. 29

12. Sample high-speed RF pin diode switch. Image and component courtesy of Fairview Microwave (www.fairview.com). 30

13. Demonstration of subtraction between two independent circularly Gaussian random variables N_1 and N_2, generated with 1000 samples from the MATLAB Gaussian random number generator. As expected, the variance of the subtracted random variables (N_2-N_1) is twice that of only one random variable (N_1). 33

14. Sample software gate applied in either the time domain as a Hadamard product (left) or in the frequency domain as a convolution (right). The time domain plot (left) is shown in decibel format while the real portion of the frequency domain gate is shown to be consistent with traditional nomenclature for each domain. 35

15. Simulated frequency domain (left) and time domain (right) responses from two scattering sources illuminated from 8.2-12.4 GHz, one located at t=0 ns with a magnitude 0.0 dB and the second source at t=2 ns with a magnitude of -10 dB compared to the first. In both plots, the black curve corresponds to the original signal while the red curve corresponds to the application of a multiplicative Finite Impulse Response (FIR) low pass filter or gate in the time domain. This filter excludes the secondary lower response from the combined signal. Note the slight degradation in the frequency response due to coupling between the two signals in time. 36

16. Illustration of the impact of vector subtraction on calibration using (3.12) and (3.16) in the frequency domain. Four curves are presented with their calibration function to the right. The magenta curve shows the Teflon sphere plus the background without any subtraction or gating applied to (3.12). The black curve shows the Teflon sphere with background subtraction but without any gating applied to (3.16). The

red curve shows the Teflon sphere with both vector subtraction and gating applied to (3.16). The blue curve shows the optimal subtracted background with gating applied to (3.16), providing practitioners with the minimum RCS (noise or clutter limit) under the current measurement configuration and the maximum possible separation between the signal of interest and the noise or clutter limit. 37

17. Illustration of the impact of vector subtraction on calibration using (3.12) and (3.16) in the time domain. Four curves are presented with the Fourier Transform of their calibration function to the right. The magenta curve shows the Teflon sphere plus the background without any subtraction or gating applied to (3.12). The black curve shows the Teflon sphere with background subtraction but without any gating applied to (3.16). The red curve shows the Teflon sphere with both vector subtraction and gating applied to (3.16). The blue curve shows the optimal subtracted background with gating applied to (3.16), providing practitioners with the minimum RCS (noise or clutter limit) under the current measurement configuration and the maximum possible separation between the signal of interest and the noise or clutter limit. Letters at the bottom of the time domain plot indicate the location of identifiable structures in chamber with respect to the position of the target: A: Antenna Interface, B: Absorber Wall Near Antenna, C: Teflon Sphere, D: Back Wall Absorber, and E: Transmit/Receive Coupling. 38

18. Measured RCS of 50.8 mm Teflon sphere using vector background subtraction and time domain gating in the frequency domain (left-black) and time domain (right-black). The Mie series for the Teflon sphere in the frequency and time domain is shown by the red curve. The visible bias error in the frequency domain is caused by imposed loss due to the presence of the foam support. 40

19. FEKO representation of a Teflon sphere (ε_r=2.05-j0.00041) 0.508 mm above a Polystyrene disk (ε_r=2. 5-j0.00041) with thickness of 1.651 mm and a diameter of 69.85 mm (left) and RCS vs Frequency (right) of the measured sphere (black), FEKO prediction of the sphere alone (red), and FEKO prediction of the sphere on top of the Polystyrene (blue). 41

20. Measured RCS of Teflon sphere (εr=2.05-j0.00041) mounted on Polystyrene disk (εr=2. 5-j0.00041) (black) with an estimated effective permittivity of the same sphere using the Mie series (εr=2.05-j0.0123) (red). 42

21. FEKO RCS of Teflon sphere mounted on Polystyrene disk (black), FEKO RCS of Teflon sphere alone (red), and FEKO RCS of Polystyrene disk alone (blue). 43

22. Inverse objective function mapping of low loss Teflon (left) and high loss Shungite (right). Mappings reveal the presence or absence of a global minimum along the real and imaginary axes. 46

23. Sensitivity of RCS magnitude for dielectric sphere $\varepsilon_r=2.0\text{-}j10^{-4}$ versus $\Delta\varepsilon'_r$ (left) and $\Delta\varepsilon''_r$ (right). 47

24. Comparison between measured and inverted RCS (left) and far-zone scattered field phase (right) for a Teflon sphere a=25.4 mm. 48

25. Comparison between measured and inverted RCS (left) and far-zone scattered field phase (right) for a Polystyrene Foam 2# sphere a=124.65 mm 48

26. Comparison between measured and inverted RCS (left) and far-zone scattered field phase (right) for an Alumina Oxide (99.5%) sphere a=12.7 mm. 48

27. Comparison between measured and inverted RCS (left) and far-zone scattered field phase (right) for a Neoprene Rubber sphere a=25.4 mm. 49

28. Comparison between measured and inverted RCS (left) and far-zone scattered field phase (right) for a Shungite sphere a=18.56 mm. 49

29. Monte Carlo 1000 trial uncertainty flow diagram reflecting percent difference between 2 Std Dev dielectric constant and loss tangent with same published values for the material shown in red. 50

30. Biaxial cube showing three degrees of freedom. 52

31. Global presentation of measured RCS of Knisely low contrast biaxial cube as a function of frequency and azimuth. Above and below the global plot are the orientations of the cube with respect to the incident field. 55

32. Measured global RCS presentations VV (left) and HH (right) from top to bottom: Teflon, low contrast uniaxial, low contrast biaxial, and high contrast uniaxial. Color axis the same for all except high contrast uniaxial for presentation purposes. 56

33. Fixed frequency azimuth-dependent slices from global measured RCS presentation of Knisely biaxial low contrast cube. 6, 10 and 14 GHz (left) and 8 and 12 GHz (right). 57

34. Fixed azimuth frequency-dependent slices from global measured RCS presentation of Knisely biaxial low contrast cube. 0 and 90 degrees (left) and 45 and 135 degrees (right)..... 57

35. Measured RCS of high contrast uniaxial cube vs isotropic Teflon cube of same dimensions. Fixed frequency azimuth-dependent slice at 8 GHz (left) and fixed azimuth frequency-dependent slice at 90 degrees. Magnitude differences and similarities at specific angles (left) reflect excitation of primary tensor parameters for each material. Magnitude differences and frequency response contraction at 90 degrees azimuth (right) reflect excitation of primary tensor parameters for each material. 58

36. Comparison of measured RCS of canonical PEC targets to predicted RCS using FEKO: squat cylinder VV (upper left) and HH (upper right), squat cylinder VV (middle left) and HH (middle right), sphere VV (lower left) and HH (lower right). 61

37. FEKO RCS of arbitrary dielectric cube (L=22.86 mm) demonstrating shifts in global minimum in frequency and magnitude for variances in real and imaginary permittivity. 64

38. Measured frequency-dependent RCS comparison between Teflon, low contrast uniaxial, and low contrast biaxial cubes. The in-plane tensor axes O-1 and O-5 are shown left and middle respectively with out-of-plane axis O-4 shown right. 66

39. Measured frequency-dependent RCS comparison between Teflon and high contrast uniaxial cubes. The in-plane tensor axes O-1 and O-5 are shown left and middle respectively with out-of-plane axis O-4 shown right. 66

40. Measured azimuth dependent RCS comparison at 8 GHz using VV (left) and HH (right) polarization for Teflon, low contrast uniaxial, low contrast biaxial, and high contrast uniaxial cubes. 68

41. FEKO RCS and scattered field phase of arbitrary dielectric cube (L=22.86 mm) demonstrating shifts in global minimum magnitude and phase for variances in real and imaginary permittivity. RCS shifts (top left) and scattered field phase (top right) versus real permittivity and RCS shifts (bottom left) and scattered field phase (bottom right) versus imaginary permittivity 68

42. RCS of Teflon cube measured versus inverted at 8 GHz VV (left) and HH (right). Inversion used RCS only without phase. 69

43. Measured scattered field phase compared to FEKO inverted phase for Teflon at 8 GHz using VV polarization (left) and HH polarization (right). Comparison reveals rotational procession and offset in the Styrofoam support superimposed on azimuth rotation. A two-step phase correction scheme mitigates most rotational errors. 70

44. RCS of Teflon cube measured versus inverted at 8 GHz VV (left) and HH (right). Inversion used RCS and phase data. 72

45. Estimated Teflon permittivity real (left) and imaginary (right) for VV and HH polarizations using azimuth-dependent measured RCS. 73

46. Configuration of uniaxial occlusions [8]. 75

47. Diagram of permittivity tensors for each anisotropic cube. Knisely orientations O-1, O-3, and O-5 (left) and O-2, O-4, and O-6 (right). The base molecule shown is an extruded rectangle representing a biaxial configuration whereas the uniaxial molecule is an extruded square. 75

48. Comparison between measured and inverted RCS of low contrast uniaxial cube: O-1 (left), O-5 (middle), and O-4 (right)..... 76

49. Low contrast uniaxial (occlusion-filled) inverted permittivity (real) overlaid with Knisely (occlusion air-filled) square waveguide results [8]. A frequency of 10 GHz was selected as a representative frequency over which the permittivity was estimated. Original plot courtesy of Alexander Knisely. Y-axis has been expanded for presentation purposes. 77

50. Comparison between measured and inverted RCS of high contrast uniaxial cube: O-1 (left), O-5 (middle), and O-4 (right)..... 78

51. High contrast uniaxial inverted permittivity (real) overlaid with Knisely square waveguide results [8]. A frequency of 10 GHz was selected as a representative frequency over which the permittivity was estimated. Original plot courtesy of Alexander Knisely. There is a known discrepancy between the original plot legend (right) and published Knisely orientation definitions. 78

52. Three-dimensional FEKO model including air-filled occlusions used to compute RCS in the O-1, O-5, and O-4 orientations. 79

53. Comparison between measured, predicted, and inverted RCS of low contrast biaxial cube: O-1 (left), O-5 (middle), and O-4 (right). 80

54. Representative RCS impact of Teflon cube mounted on Polystyrene support disk as a function of frequency using HH polarization. RCS of Teflon cube on disk, disk alone, and complex subtraction (left). Expanded view of teflon cube mounted on cube and subtracted RCS (right). 84

55. Representative RCS impact of Teflon cube mounted on Polystyrene support disk as a function of frequency using VV polarization. RCS of Teflon cube on disk, disk alone, and complex subtraction (left). Expanded view of teflon cube mounted on cube and subtracted RCS (right). 84

56. Representative RCS impact of Teflon cube mounted on Polystyrene support disk as a function of azimuth at 10 GHz using HH polarization. RCS of Teflon cube on disk, disk alone, and complex subtraction (left). Expanded view of teflon cube mounted on cube and subtracted RCS (right). 85

57. Representative RCS impact of Teflon cube mounted on Polystyrene support disk as a function of azimuth at 10 GHz using VV polarization. RCS of Teflon cube on disk, disk alone, and complex subtraction (left). Expanded view of Teflon cube mounted on cube 85

58. Change in RCS for baseline Teflon RCS versus 0.2-degree alignment error. Note: Y-Axis is in thousandths of one dB. 87

59. Teflon permittivity uncertainty bounds real (left) and imaginary (right) at 8 GHz for VV and HH polarizations. 90

60. Low contrast biaxial permittivity uncertainty bounds real (left) and imaginary (right) at X-band for O-1, O-5, and O-4 orientations. 90

61. Low contrast uniaxial permittivity uncertainty bounds real (left) and imaginary (right) at X-band for O-1, O-5, and O-4 orientations. 91

62. High Contrast uniaxial permittivity uncertainty bounds real (left) and imaginary (right) at X-band for O-1, O-5, and O-4 orientations. 91

63. Notional absorber-lined transmission tunnel. 92

64. Typical focused beam system (FBS) configuration showing lenses, feed antennas, and sample mounting structure (left). Same system showing material coupon mounted within support frame (right). Used by permission. Photo courtesy of the Compass Technology 92

65. Teflon inversion convergence history under VV and HH polarizations for real permittivity (left), imaginary permittivity (middle), and the inversion objective function (right). 99

66. Low contrast uniaxial inversion convergence history for orientations O-1, O-5, and O-4 for real permittivity (left), imaginary permittivity (middle), and the inversion objective function (right). 99

67. High contrast uniaxial inversion convergence history for orientations O-1, O-5, and O-4 for real permittivity (left), imaginary permittivity (middle), and the inversion objective function (right). 100

68. Low contrast biaxial inversion convergence history for orientations O-1, O-5, and O-4 for real permittivity (left), imaginary permittivity (middle), and the inversion objective function (right). 100

List of Tables

Table **Page**

1. Dielectric spheres selected for analysis. 21

2. Estimated permittivity of five dielectric spheres from inversion process with percent difference from various published sources and compared with Von Hippel. 45

3. Monte Carlo uncertainty of measured dielectric constant and loss tangent of six dielectric spheres expressed as a percentage from the inverted complex permittivity. 50

4. Qualitative analysis of estimated permittivity for each tensor axis, in-plane (O-1 and O-5) and out-of-plane (O-4). Unknown permittivity is compared to Teflon (T) based on null frequency and null level. 66

5. Comparison of inverted Teflon permittivity at 8 GHz using RCS alone versus the addition of phase information at both VV and HH polarizations. 72

6. Estimated permittivity comparison between Knisely low contrast biaxial cube and current research inversion for all three measured orientations O-1, O-5, and O-4. 80

7. RMS Error in real and imaginary permittivity for each cube and their respective in-plane orientations (O-1 and O-5) and out-pf-plane orientation (O-4). LCB=Low Contrast Biaxial. LCU=Low Contrast Uniaxial. HCU=High Contrast Uniaxial. 89

CHARACTERIZATION OF ANISOTROPIC MATERIALS USING SCATTERED FIELD MEASUREMENTS

I. Introduction

1.1 Problem Statement

The materials community exists as a four-member fraternity comprised of those who design, synthesize, characterize, and apply materials across multiple disciplines. In the electromagnetics context, additive manufacturing and the ability to create microstructure arrays have opened the application space to new antennas, radomes, and artificial mediums not previously available [1]. Despite these advances, the ability to characterize the electromagnetic properties of these new materials has not appreciably changed in decades. The reason for this lag is the inherent limitation in exploiting the requisite material properties at the microscopic level using available macroscopic measurement techniques. As an example, consider the need to characterize the permittivity of a dielectric material (i.e., dielectric constant and loss tangent) which requires a minimum of n independent measurements. This can be accomplished through multiple realizations of frequency, angle of incidence, polarization, sample geometry, and S-parameters. For isotropic materials, $n = 2$, uniaxial materials, $n = 4$, and for biaxial materials, $n = 6$ [2]. Beyond the biaxial case, the inclusion of off-diagonal tensor parameters (e.g., gyrotropic materials), permeability, or bi-anisotropy rapidly increases the number of required independent measurements to as many as $n = 72$. The ability to synthesize designer anisotropic materials has exceeded the measurement diversity that can be achieved using common S-

parameter methods. Successful anisotropic characterizations using modified S-parameter techniques have been reported by Knisely [3], Amert [4], and Scott [5].

Free-space scattered field measurements offer the potential for added data independence by varying target illumination, configuration, frequency, and polarization, all of which are fixed commodities in traditional methods. In addition, such a method may relieve the need to precisely machine samples to accommodate geometric- and field-specific requirements of sample holders. To isolate where a scattered field approach to permittivity estimation fits within the larger context of dielectric characterization, consider the graphic shown in Figure 1. Here, the most common methods of dielectric material characterization are spatially distributed according to material category, specimen preparation, fixture type, and accuracy. The graphic has been modifed to include a blue oval and accompanying blue text which identifies the anticipated region of applicability for anisotropic scattered field measurements as compared to other methods, including focused beam systems (FBS) and transmission tunnels. The blue region of this graphic was selected since the accuracy for these methods are not anticipated to be greater than filled waveguide and, while they are broadband, they also require little if any sample preparation. However, FBS and transmission tunnel methods depart in similarity to a scattered field approach as their incident fields can significantly change as a function of sample thickness. The anisotropic scattered field approach is well-suited for non-destructive testing of bulk materials and may also provide options for thin films and sheets.

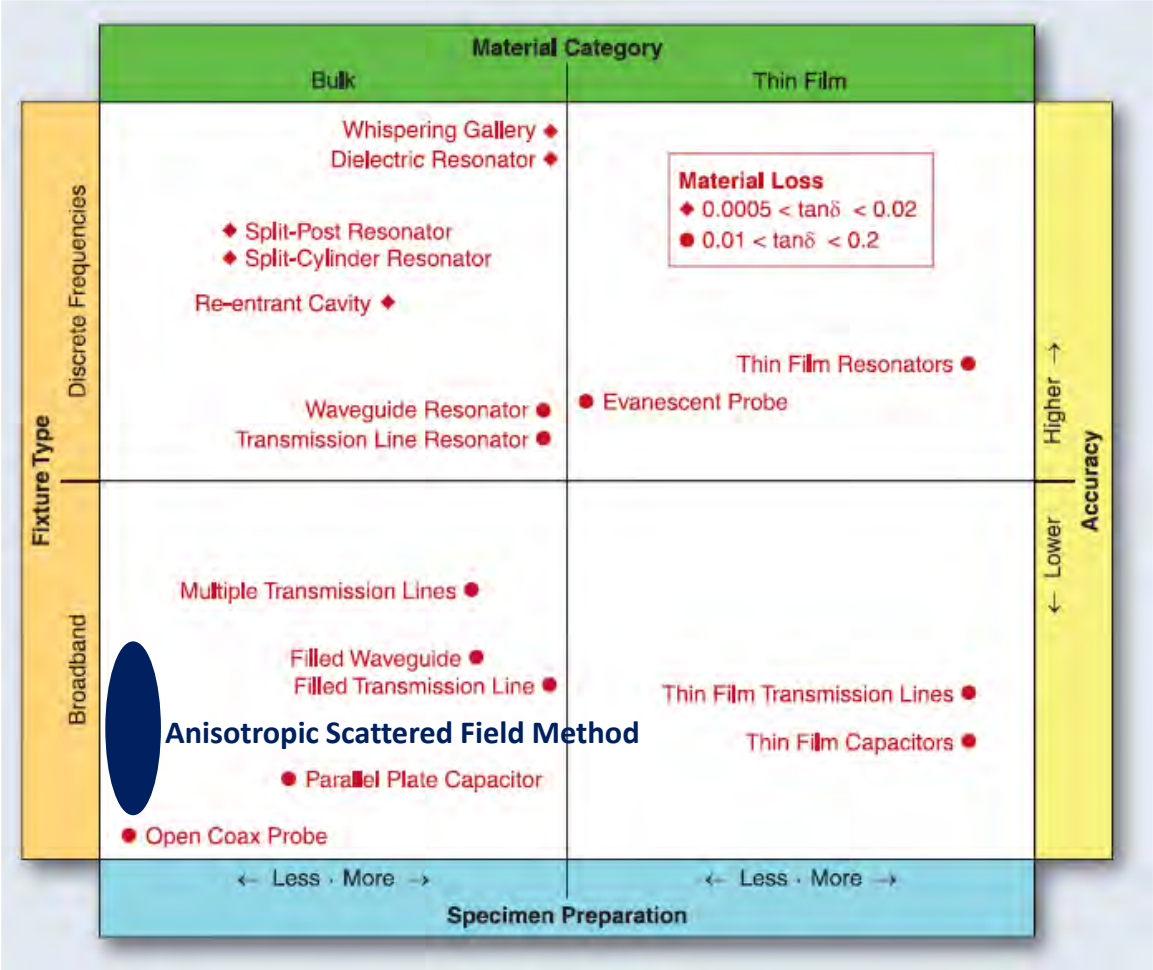

Figure 1. Map of common dielectric measurement techniques spatially distributed according to material category, specimen preparation, fixture type, and accuracy [6]. Note: a dark blue oval and accompanying blue text have been added to the graphic indicating the efficacy of the proposed method within the greater context of material characterization techniques.

While Figure 1 depicts the suitability of various material measurement techniques based on material and fixture type, sample preparation, and general accuracy, it does not provide clarity regarding the connection between measurement technique, permittivity, and frequency as does the graphic shown in Figure 2. Here, the efficacy of free-space methods is shown to be of value over a wide band of frequencies ranging from 1-1100 GHz and over a wide dielectric constant of 1-60. However, the same graphic reveals a narrower

region for loss tangent applicability (0.005-0.5) than other methods such as the two-port waveguide and open-ended coaxial probe.

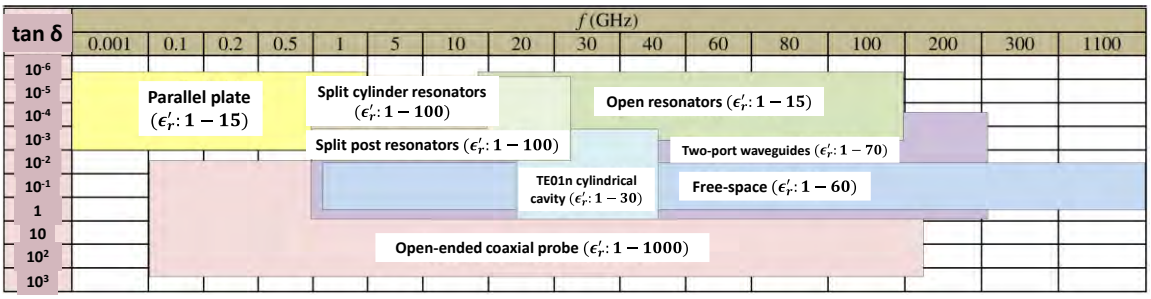

Figure 2. Comparison of dielectric measurement techniques as a function of complex permittivity and frequency [7]. Note: fonts with white backgrounds have been added for presentation purposes.

While it is clear that free-space methods offer diversity in measurements, the question is whether that diversity will produce anisotropic tensor values with non-overlapping uncertainties and offer performance comparable to other free-space approaches such as the FBS and transmission tunnel. The answer lies in the ability to mitigate errors associated with free-space measurements and is dependent on samples of interest providing sufficient scattering behavior to exploit anisotropic scattering phenomena.

1.2 Scope and Research Goals

The principal scope of this research is to extend the work of Knisely [3, 8] in a free-space scattered field context. Knisely demonstrated a square waveguide method of anisotropic estimation that achieved non-overlapping uncertainties for low-contrast biaxial and high-contrast uniaxial dielectric cubes (hereafter referred to as the "Knisely Cubes"). The biaxial representation of permittivity may be defined as

$$\overleftrightarrow{\epsilon_r} = \begin{bmatrix} \epsilon_{xx} & 0 & 0 \\ 0 & \epsilon_{yy} & 0 \\ 0 & 0 & \epsilon_{zz} \end{bmatrix}, \tag{1.1}$$

where $\overleftrightarrow{\epsilon_r}$ is the biaxial complex anisotropic tensor and $\epsilon_{mn} = \epsilon'_{mn} + j\epsilon''_{mn}$ is the component in the m, n directions $x, y, and\ z$. ϵ'_{mn} is the dielectric constant and ϵ''_{mn} is the loss term (also expressed as loss tangent $tan\ \delta = \epsilon''_{mn}/\epsilon'_{mn}$). In the isotropic condition, $\epsilon_{xx} = \epsilon_{yy} = \epsilon_{zz}$, uniaxial condition, $\epsilon_{xx} = \epsilon_{yy} \neq \epsilon_{zz}$, and biaxial condition, $\epsilon_{xx} \neq \epsilon_{yy} \neq \epsilon_{zz}$. Knisley's work was limited to estimating ϵ'_{mn} from 8.2-12.4 GHz based on the internal dimensions of X-band waveguide (22.86 mm x 10.16 mm) and the available additive technology used to create the cubes under test. This research will include the estimation of ϵ''_{mn} and examine broadband scattering from 6-18 GHz while maintaining 8.2-12.4 GHz as a validation band for comparison with prior Knisely results.

Knisely utilized a single waveguide mode to independently excite the biaxial components of the cubes under test. The waveguide provides an infinite sample environment which greatly simplifies the forward and inverse solutions. In a free-space context, the sample is finite, producing scattered fields in all three coordinate directions.

There are four primary radiofrequency (RF) illumination scenarios capable of providing value-added scattering information, as shown in Figure 3. In the monostatic configuration, the transmit and receive antennas are coincident with each other. The bistatic configuration separates the transmit and receive antennas from the target by angle θ. The defining metric for each of the four scenarios at a specific wavelength, λ, is the distance, R, between the transmit antenna (annotated by Tx) and the target, and between the target and the receive antenna (annotated by Rx). The relationship between R, D, and λ in each of the four quadrants of Figure 3 is referred to as the far-field criteria [9, 10][1] when the

[1] Bistatic near-field illumination may also be expressed with one leg as far-field and the other near-field.

phase taper across the target extent, D, at distance, R, is no greater than $\pi/8$ $(\lambda/16)$ as defined by

$$\begin{aligned} R &\gg 2\frac{D^2}{\lambda} \\ R &\gg D \\ R &\gg \lambda. \end{aligned} \tag{1.2}$$

Bistatic illumination is an attractive option for target illumination in that the scattered fields provide independent information not seen in a monostatic configuration. However, the added burden of target-receive mutual coupling and calibration complexities make a monostatic configuration favorable. Near-field illumination simultaneously provides all three scattered field components which are essential to identifying the independent biaxial parameters. Yet, the added complexity of separating the three components simultaneously makes monostatic far-field illumination the configuration of choice for this research. As the scattered field is a vector quantity having magnitude and phase, both are of interest to this research and useful for subsequent permittivity estimates from measured data. While the scattered field phase is measured directly by a coherent receiver, the scattered field magnitude will be converted to radar cross section (RCS), σ, such that comparisons with prior efforts and existing nomenclature are preserved. RCS is defined as

$$\sigma = \lim_{r\to\infty}\left[4\pi r^2 \frac{|E^s|^2}{|E^i|^2}\right], \tag{1.3}$$

where r is the distance from transmitter to target and E^s and E^i represent the scattered and incident fields respectively. In general, E^s and E^i are polarization-dependent and considered vector quantities. Here in (1.3) and for the remainder of this paper, it is assumed that E^s and E^i are co-polarized complex scalar quantities. In the monostatic far-field

context, E^s and E^i are both identically measured at position r. In practice, the asymptotic limit of the distance between the transmit antenna and target is approximated by a finite distance satisfying the far-field criteria. The phase of the scattered field will be preserved as-is in keeping with prior efforts and existing nomenclature.

Having examined the work of Knisely, an incremental extension limits the scope of this research to estimating the complex biaxial permittivity of the Knisely Cubes under monostatic RCS conditions from 6-18 GHz. In addition to the Knisely Cubes, an isotropic Teflon reference cube of equal dimensions to the Knisely Cube will be used to identify and mitigate errors associated with the technique. In addition, this helps to establish an automated scheme for estimating the complex permittivity of the anisotropic samples. A description of the cubes under consideration is shown in Figure 4.

By extending the work of Knisely, this research offers the following contributions to anisotropic estimation:

- Extension of biaxial estimation to a free-space far-field context.
- Established biaxial estimation uncertainty for real and imaginary components.
- Identified conditions for non-overlapping uncertainty among anisotropic axes.
- Demonstrated isotropic inversion of anisotropic axes.
- Defined use of azimuth- and frequency-dependent scattering information.
- Demonstrated biaxial inversion without complex hardware or costly facilities.

The goals of this research include the following:

- Demonstrate the use of monostatic RCS measured data as a means of estimating complex biaxial permittivity.

- Define the advantages and disadvantages of using fixed frequency azimuthal RCS data versus RCS as a function of frequency to estimate biaxial permittivity. This includes the advantages and disadvantages of using the magnitude of the scattered field alone or incorporating phase as an independent contributor to accurate biaxial estimation.
- Determine the conditions under which the method produces non-overlapping uncertainties. If the method produces overlapping uncertainties, then an anisotropic determination cannot be made for any individual material.
- Identify the distinctives between the use of artificial media in waveguide (infinite) versus free space (finite). The inability to individually excite a permittivity tensor axis greatly increases the forward estimation and inverse problems.
- Demonstrate the ability to estimate biaxial permittivity without the use of complex hardware or costly facilities.

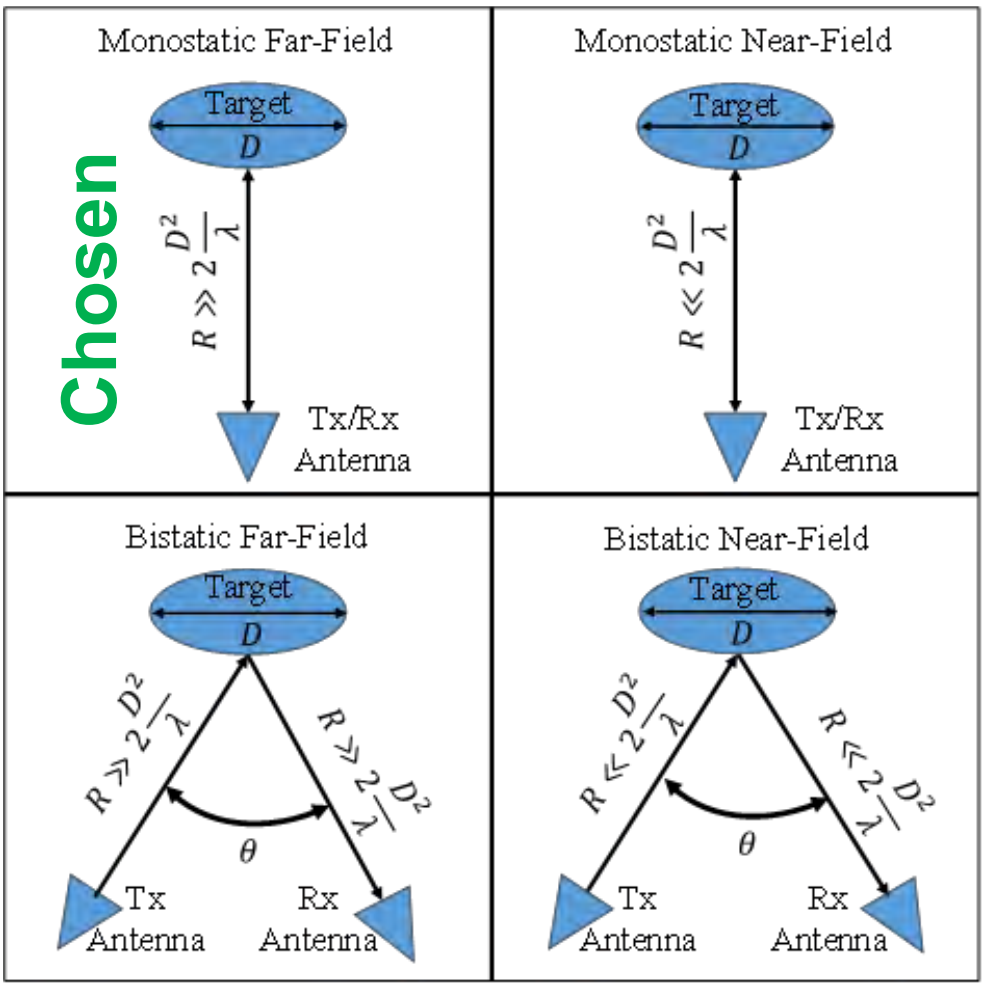

Figure 3. Available target illumination choices. Monostatic far-field illumination (top left), monostatic near-field illumination (top right), bistatic far-field illumination (bottom left), and bistatic near-field illumination (bottom right).

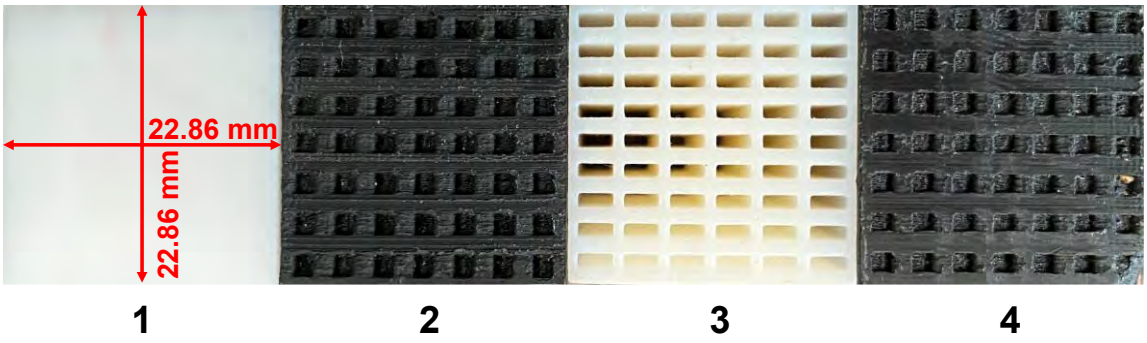

Figure 4. Dielectric cubes used in research, each having a side 22.86 mm: (1) Teflon/Solid: Isotropic – no contrast, (2) Nylon/Low Loss Occlusions: Uniaxial - Low Contrast, (3) Nylon/Air Occlusions: Biaxial – Low Contrast, and (4) Nylon/ESD-PETG Occlusions: Uniaxial - High Contrast.

1.3 Limitations and Challenges

Prior RCS measurement experience suggests that target-mount interactions will be a driving source of error, negatively impacting permittivity estimates. Creating a mounting structure that accurately and repeatably supports the cubes under test while minimizing target-mount interactions will be a challenge. Additionally, loss tangent is known to be more error prone than the dielectric constant in free-space methods. Seeking a best practice that encourages accurate estimates of loss tangent will also be a challenge.

1.4 Resource Requirements

Applied Research Associates in Dayton, Ohio has graciously offered the use of their state-of-the-art RCS measurement facilities, their expansive library of computational electromagnetics software, including FEKO, SENTRi, CST Microwave Studio®, and the Periodic Moment Method. These are in addition to their contingent of machine shop tools and workshop. In addition, the Air Force Institute of Technology (AFIT) has supplied the 3D printed anisotropic Knisely Cubes whose permittivity was characterized in prior efforts and will provide traceability as a means of method validation.

1.5 Organization

This research utilizes measured monostatic RCS data to estimate complex biaxial permittivity. Chapter 2 discusses existing efforts to use RCS measurements as a means of estimating isotropic permittivity and the motivation for extending that work toward anisotropic permittivity. Chapter 3 discusses the methodology for the use of RCS measurements to estimate isotropic, uniaxial, and biaxial permittivity. This discussion includes the role of dielectric spheres in identifying common errors in RCS measurements and their impact on permittivity estimation, as well as the methodology in estimating the permittivity of uniaxial and biaxial cubes. Chapter 4 examines the validity of the method by comparing the estimated permittivity with legacy data for the isotropic, uniaxial, and biaxial dielectric cubes. A discussion of uncertainty evaluates the validity of the method by analyzing the presence of non-overlapping uncertainties and other factors impacting accurate biaxial estimates. Finally, Chapter 5 provides commentary on the efficacy of the method and its limitations and recommendations for further work.

II. Background and Motivation

Methods of characterizing simple materials (i.e., linear, homogeneous, and isotropic) are ubiquitous among material measurement practitioners. Surveys of these methods and their respective applications have been widely reported [6, 7, 11-15]. These methods offer two distinct advantages over finite samples interrogated in free space by a planewave. First, since the incident field is concentrated in the sample, the signal-to-noise ratio is substantial, which limits uncertainty and enhances available receiver dynamic range for characterizing reflective or lossy materials. Second, the currents generated in materials are constrained to the direction of their incident field components as if the sample was infinite in extent[2]. This makes the use of straightforward inversion schemes such as Nicolson-Ross-Weir (NRW) possible [16, 17].

The principle disadvantage of traditional techniques, especially in anisotropic applications, is that the tensor axes must be aligned with the incident field components, making alignment of the material difficult without intentionally machining the sample or the sample holder. This assumes that the orientation of the material tensor axes is known, which for some materials may not be true. Additionally, some anisotropic materials cannot be machined without altering their permittivity in one or more of the tensor axes. A far-field illumination provides incident angle and polarization diversity to accommodate the orientation of the tensor axes, making it an attractive method of sample interrogation. However, this flexibility comes at the cost of measurement errors induced by mutual

[2] This holds true for a biaxial material. If a gyrotropic material, whose off-axis tensor elements are non-zero, is placed in a rectangular waveguide, the fields inside the material will have components orthogonal to the incident field polarization. While those same field components will be evanescent and decay, the original infinite field distribution assumptions are no longer valid.

coupling between the material sample and the mounting structure; alignment errors between the sample geometry and the incident field; reduced signal-to-noise ratio; and perturbations in the incident field caused by the illuminating antenna itself or bistatic scattering from structures in the measurement environment.

The next two sections describe existing work in estimating isotropic and anisotropic material permittivity using RCS measurements. The chapter concludes with a rationale for pursuing a biaxial RCS measurement approach to permittivity estimation considering prior efforts.

2.1 Isotropic Permittivity Estimation using RCS Measurements

In 1963, interest in the RCS measurements of dielectric coated spheres and cylinders was first reported by Swarner and Peters [18, 19]. Soon after, Abbato reported the use of monostatic RCS measurements as a means of estimating the permittivity of isotropic homogeneous spheres [20]. Spheres are attractive scattering models as they are not subject to physical alignment errors, their contact area with mounting structures is minimal, and their far-field scattering is easily computed by use of the Mie Series [21]. Abbato applied his approach to spheres whose radius lies in the range $3.6 < ka < 5.2$, where k is the wavenumber $(2\pi/\lambda)$ and a is the sphere radius. He utilized a graphical look-up table to compare pre-computed sphere RCS magnitude to measured RCS magnitude using a least squares approach. Abbato's use of resonant-sized spheres and least squares inversion approach are directly applicable to the current effort. The sphere is not a suitable target for biaxial applications since most anisotropic geometries are inherently rectangular which is not useful in spherical coordinate applications. Following Abbato, in 1967 and 1970

respectively, Young [22] and Yu [23] presented bistatic RCS measurement techniques that estimated permittivity and permeability by exploiting approximations of the Mie series for small spheres of radius $ka < 0.2$. While both efforts successfully estimated permittivity and permeability using bistatic RCS measurements, the use of electrically small spheres is not helpful to anisotropic modeling.

A significant pause in the literature occurred after Yu until 2009 when Ishikawa [24] proposed an RCS measurement technique to estimate the permittivity of electrically large cubes from bulk material. He isolated the front-face reflection of the total scattered field using time domain gating [25], making use of the plane wave Fresnel coefficient which, in the case of Ishikawa, relates sample permittivity, angle of incidence, and reflection coefficient at normal incidence for an infinite planar interface,

$$\epsilon_r = \left(\frac{1-\Gamma}{1+\Gamma}\right)^2, \tag{2.1}$$

where ϵ_r is the complex relative permittivity and Γ is the reflection coefficient at the interface between free space and the material under test. Ishikawa relates Γ to the measured RCS of an electrically large homogeneous plate using physical optics. This method may be extended to in-plane uniaxial permittivity as shown in Figure 5, in which Knisely's cube orientations O-1 and O-5 present a homogeneous sample in the direction of propagation. Thus, extracting the front face reflection of the cube in either of these two orientations would be the same, as slices of the cube are taken at any point along the direction of propagation. This, of course, would restrict the method to sufficiently thick samples (electrically speaking) to separate the front and rear surface scattering as a function of time. However, in the other four orientations the sample appears as a volumetric effective media

[26] and would present a different front face reflection at every slice along the direction of propagation, thus eliminating the technique for consideration of biaxial materials. A full free space RCS measurement approach illuminates the whole cube at any angle of incidence, viewing the array of occlusions as an effective anisotropic media (assuming spatial requirements were satisfied [27]).

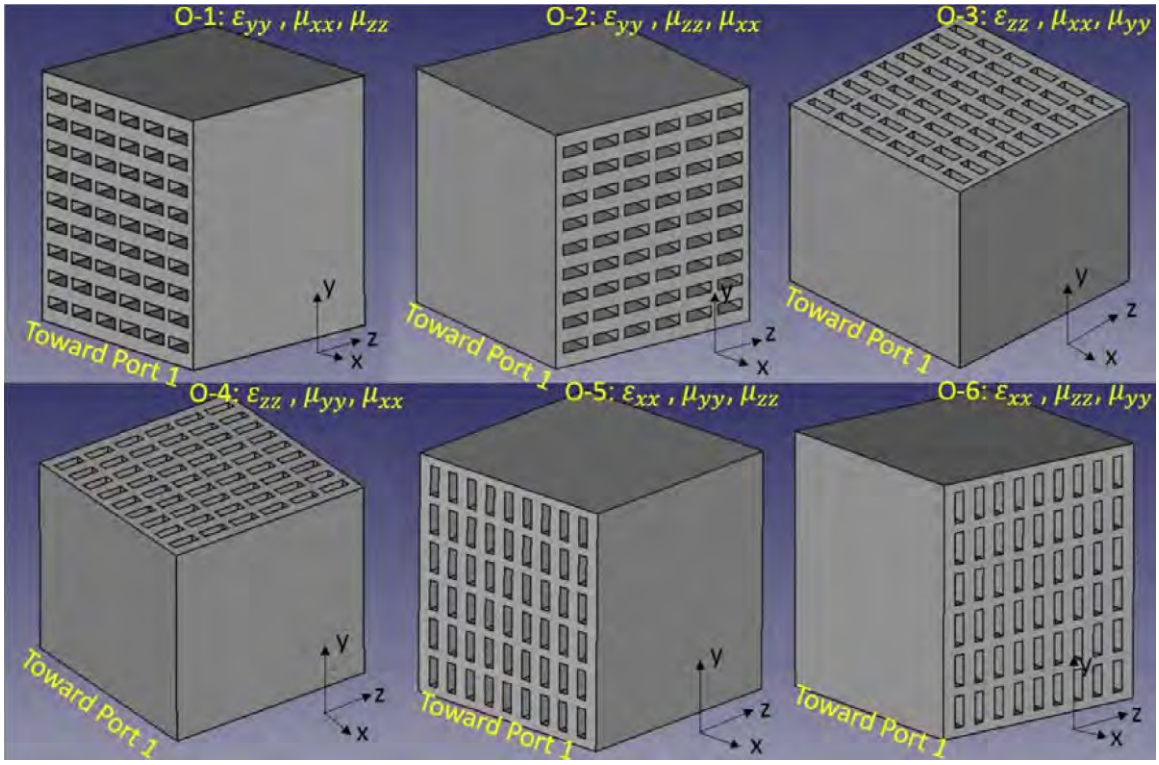

Figure 5. Biaxial Knisely Cube unit cell orientations with respect to incident field. For all orientations shown, the incident field originates from Port 1 (Knisely, 40).

Eyraud [28] followed Ishikawa in 2015 with a bistatic RCS method of sphere permittivity estimation which utilized Bayesian estimation to incorporate measurement error directly into the inversion process. This is in contrast with the more typical application of uncertainty after the inversion process. A free space measurement of spheres is the least complicated target to measure as it affords the opportunity to optimize the measurement process and identify ways to increase inversion accuracy and efficiency. In 2016, Perret

[29] demonstrated a unique quasi-monostatic[3] configuration to characterize low loss bulk dielectric materials with RCS measurements. His process was based on RFID technology which has a resonator in the presence of a dielectric whose resonant frequencies are known a priori. Perret related the change in resonance-Q of the measured backscatter signal to the permittivity of the resonator backing material. This method is not amenable to anisotropic characterization as the scattered fields will not align with the tensor axes in the presence of the resonant structure.

Lastly, in 2021 Saleh [30] made a contribution by utilizing bistatic RCS measurements to characterize the permittivity of 3D printed spheres. The unique contribution from this work was the identification of the density of 3D printed elements required to produce various permittivities in anisotropic samples. The spheres themselves are modeled as though they are homogeneous and isotropic, whereas the dielectric cylinder comprising the spheres may be used in the construction of anisotropic arrays at the proper scale suggested by Kong and Collin [26, 27, 31]. Selah's 3D printed spheres are comprised of a triangular mesh of cylinders just as one would create when using a full-wave solver. A sample of Sale's dielectric spheres is shown in Figure 6. This work especially applies to the development of low contrast anisotropic bodies such as that used by Knisely [3].

[3] Quasi-monostatic refers to the antenna arrangement whereby the transmit and receive antennas are physically close to each such that the bistatic angle between them and the target is negligible. The purpose for such an arrangement is to mitigate the strong impedance mismatch between the transmit antenna and free space which may consume much of the available receiver dynamic range. In larger RCS measurement facilities, this errant return and that from reflectors, walls, floor, ceiling, etc., is mitigated by the application of high-speed RF switching which turns the receiver on only when the target return is anticipated.

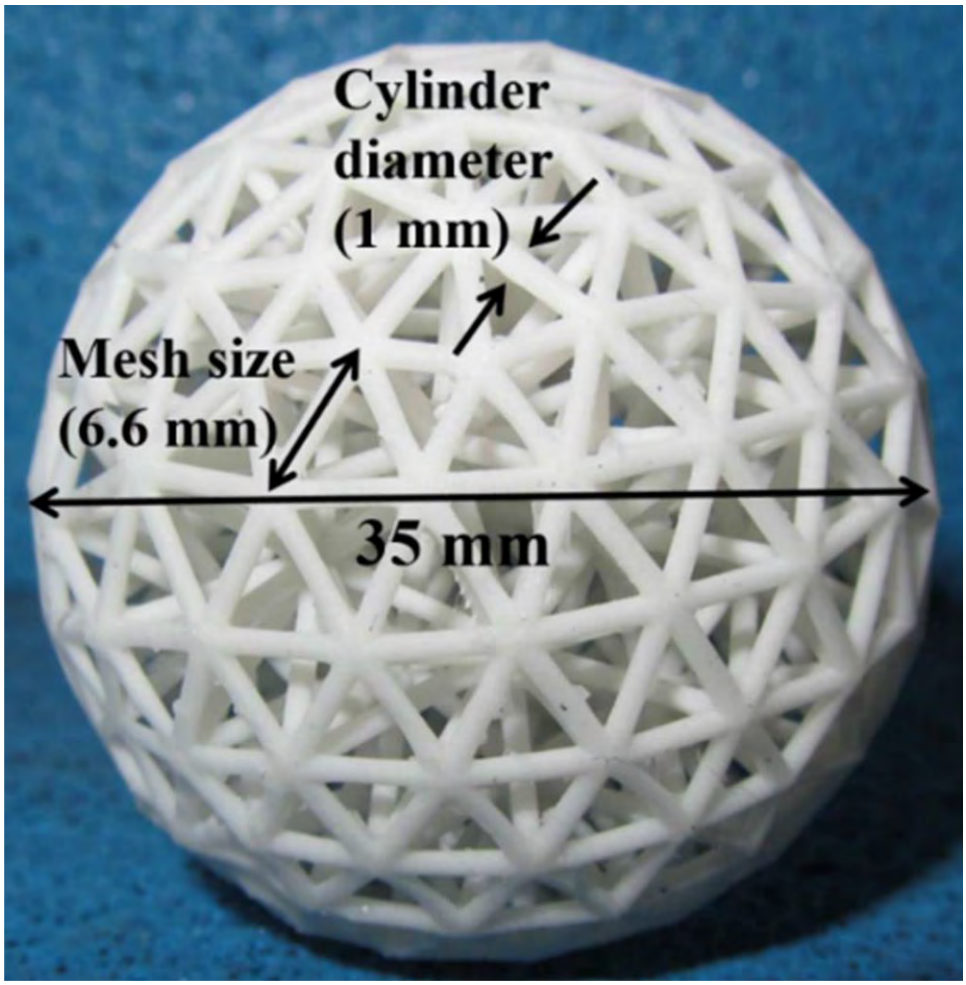

Figure 6. 3D printed homogeneous isotropic sphere comprised of dielectric cylinders in a triangular patch format (Saleh [30])

From Abbato to Saleh, RCS measurements have been used to characterize isotropic spheres and cubes of varying electrical size using both monostatic and bistatic illumination. These efforts demonstrate the efficacy of RCS measurements as a tool for inverting constitutive parameters, but none of them attempt to estimate anisotropic permittivity in a far-field context or define their associated uncertainties as in the case of the current research.

2.2 Anisotropic Permittivity Estimation using RCS Measurements

To date, efforts to estimate anisotropic permittivity using RCS measurements have not been reported. However, in 2012, Hollander [32] reported on a method for extracting single- and double-negative metamaterial properties using an in-line transmit-receive antenna configuration with shaping lenses to limit the incident field from illuminating the sample edges. This approach is akin to the focused-beam system (FBS) methods developed by Schultz [33]. Also, in 2020, Gorman [34] demonstrated biaxial inversions of low and high contrast biaxial planar samples, again using a FBS. Gorman's work, for his biaxial estimation, is directly applicable to this research but is limited to thin planar samples since the focused beam incident field does not offer a plane wave of extent. As such, a volumetric effective media model would exceed the plane wave capability of the FBS and suffer from magnitude and phase illumination errors [35, 36]. The current research provides true planewave illumination over the full extent of the anisotropic model. While finite model illumination creates added complexity due to full-body scattering, it not only dramatically increases the experimental trade-space for diverse shapes and non-cooperative tensor alignment, but also provides a measurement context to analyze new effective media designs.

2.3 Motivation

As indicated by the literature, success has been widely reported in isotropic inversions using monostatic and bistatic RCS measurements. However, no work has been reported that utilizes far-zone scattered fields to estimate biaxial permittivity. As such, the call for

additional techniques to evaluate anisotropic materials without the need to accommodate specific sample holder geometries and their respective field configurations remains.

The first step in this research is to demonstrate isotropic inversion capabilities for a wide range of dielectric spheres in the same context as Abbato [20]. The purpose of this task is to develop the requisite target illumination and mounting configurations, demonstrate the presence of practical signal-to-noise levels, and examine the physics associated with dielectric body scattering.

Once competence has been demonstrated with isotropic spheres, the ability to estimate the permittivity of an isotropic cube will be shown. This exercise will inform the process as to mounting structure implications, forward solver requirements, measurement sampling issues, and inversion algorithm options. This will be followed by the estimating the permittivity of a anisotropic media consisting of low contrast and high contrast uniaxial cubes and a low contrast biaxial cube. Moving from isotropic to anisotropic media has anticipated challenges that include increased forward solver computation time, inversion scheme complexity, isolation of individual tensor parameters due to finite full-body scattering, and potentially overlapping uncertainty metrics due to measurements errors.

An uncertainty model which incorporates all relevant error sources will be applied to permittivity estimates in Chapter 4. This will be followed in Chapter 5 by conclusions along with recommendations for future work.

III. Methodology

In Chapter 2, prior efforts were identified from the literature that used RCS measurements of spheres to estimate isotropic permittivity. Spheres provide an entryway into the more complex measurements of anisotropic arbitrary-shaped materials by establishing an incident field, target support, sampling requirements, antenna and network analyzer configuration, calibration approach, and signal processing needs. This chapter opens with a permittivity estimate of five dielectric spheres of diverse permittivity. The premise is that if adequate isotropic permittivity estimation using RCS measurements is intractable, then pursuing a biaxial estimate is inappropriate. Following a successful demonstration using isotropic spheres, attention will turn toward the use of an isotropic cube, providing an incremental step toward the use of anisotropic cubes.

3.1 Free Space Permittivity Estimation using Spheres

A brief overview of scattering from dielectric spheres will be presented followed by a description of the measurement configuration, process, calibration, and inversion algorithm. Finally, uncertainty bounds in estimated permittivity based on errors in measured RCS magnitude, scattered field phase, and sphere radius will be provided. Five isotropic spheres were selected for analysis whose name, radius, and published permittivity are shown in Table 1. The criteria for sphere selection was permittivity diversity, availability, homogeneity, and sphericity. The range of dielectric constant selected is about $1 < \epsilon_r' < 10$ with a loss tangent range about $0.0001 < tan\delta < 0.5$ based on published estimates. For the sake of this research, it is assumed that these materials are non-dispersive within the primary frequency region of 8.2-12.4 GHz.

Table 1. Dielectric spheres selected for analysis.

Sphere Material	Radius (mm)	Published Permittivity			
		ϵ_r	$tan\delta$	$f(GHz)$	Ref
Teflon	25.4	2.055	2.1e-4	9.816	[37]
Polystyrene 2#	124.65	1.037	1.0e-4	3.25	[38, 39]
Alumina 99.5%	12.7	9.8	1.0e-4	1.0	[40]
Neoprene	25.4	2.84	4.8e-2	3.0	[41]
Shungite*	18.56	x	x	x	x

*Sold as such x=Not available

Sphere Scattering Review

From (1.2), RCS, σ, is restated here as

$$\sigma = \lim_{r\to\infty}\left[4\pi r^2 \frac{|E^s|^2}{|E^i|^2}\right], \tag{3.1}$$

where r is the distance from emitter to target and E^s and E^i represent the scattered and incident fields respectively. In a monostatic far-field context, E^s and E^i are both identically located at position r. Balanis [21] represents the far-zone backscattered field of a dielectric sphere of radius, a, as

$$E^s = jE_0 \frac{e^{-j\beta r}}{\beta r}\sum_{n=1}^{\infty} j^n(-1)^n \frac{n(n+1)}{2}[b_n - c_n], \tag{3.2}$$

where E_0 is the magnitude of the incident field, β_0 and β_d are the free space and dielectric wavenumbers respectively. The parameters b_n and c_n are described by

$$b_n = \frac{-\sqrt{\epsilon_r}\hat{J}_n'(\beta_0 a)\hat{J}_n(\beta_d a) + \sqrt{\mu_r}\hat{J}_n(\beta_0 a)\hat{J}_n'(\beta_d a)}{\sqrt{\epsilon_r}\hat{H}_n^{2\prime}(\beta_0 a)\hat{J}_n(\beta_d a) - \sqrt{\mu_r}\hat{H}_n^{(2)}(\beta_0 a)\hat{J}_n'(\beta_d a)} a_n \tag{3.3}$$

$$c_n = \frac{-\sqrt{\epsilon_r}\hat{J}_n(\beta_0 a)\hat{J}_n'(\beta_d a) + \sqrt{\mu_r}\hat{J}_n'(\beta_0 a)\hat{J}_n(\beta_d a)}{\sqrt{\epsilon_r}H_n^{(2)}(\beta_0 a)\hat{J}_n(\beta_d a) - \sqrt{\mu_r}H_n^{2\prime}(\beta_0 a)\hat{J}_n'(\beta_d a)} a_n, \tag{3.4}$$

where $a_n = j^{-n}\frac{(2n+1)}{n(n+1)}$, $\hat{J}_n$ and $H_n^{(2)}$ indicate spherical Bessel and Hankel functions of the second kind respectively. The superscript, $(')$, indicates a first derivative with respect to βa. Inserting b_n and c_n into (3.2) in the context of (3.1) yields the intermediate solution

$$\sigma_c = \frac{\lambda}{2\sqrt{\pi}}\sum_{n=1}^{\infty}(-1)^n(2n+1)[b_n - c_n], \tag{3.5}$$

whose sum, σ_c, yields the complex far-zone scattered field. Taking $|\sigma_c|^2$ we obtain the RCS formally defined in (3.1) as

$$\sigma = \frac{\lambda^2}{4\pi}\left|\sum_{n=1}^{\infty}(-1)^n(2n+1)[b_n - c_n]\right|^2 \tag{3.6}$$

and whose phase is computed as

$$\Phi = tan^{-1}\left[\frac{Im(\sigma_c)}{Re(\sigma_c)}\right]. \tag{3.7}$$

The monostatic scattering mechanisms for a perfectly conducting sphere are limited to a specular term from the first-incident point followed in time by a creeping wave term at $\tau = (a/c)(2+\pi)$ [42]. In contrast, the combined monostatic scattered field from a homogeneous dielectric sphere is the superposition of numerous responses. These include the specular response, internal reflections, and resonances depending on electrical size of the sphere [43-45]. The computed normalized RCS of a perfect electrical conductor (PEC) sphere versus that of a Teflon sphere are shown as a function of free space $\beta_0 a$ in Figure 7

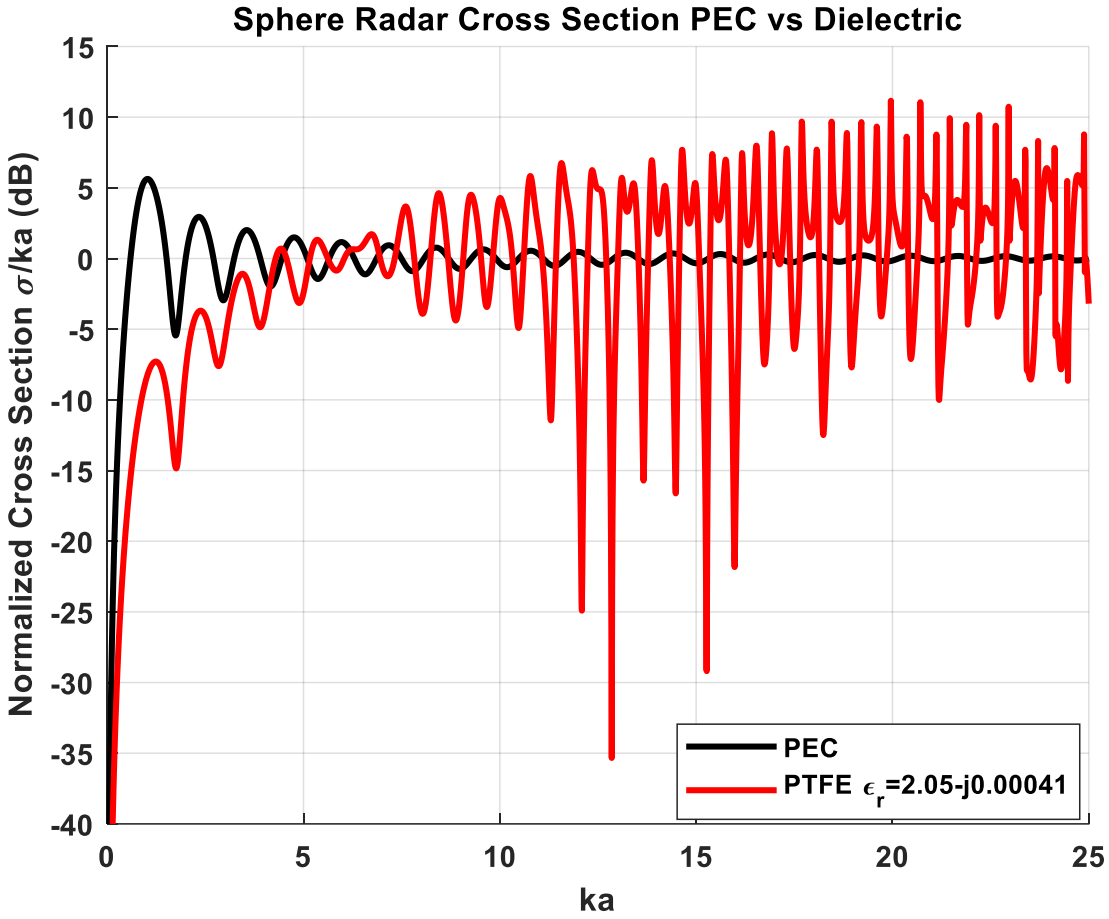

Figure 7. Normalized RCS ($\sigma/\beta_0 a$) comparison between PEC sphere and Teflon sphere as a function of free space $\beta_0 a$.

Measurement Configuration and Calibration

The measurement configuration consisted of an Agilent E8364B Network Analyzer, Flam and Russel 6414 Diagonal Horn Antenna, and low-density foam mount. A photo of the measurement configuration with a 50.8 mm diameter Teflon sphere mounted on the low-density mount is shown in Figure 8.

Figure 8. Teflon sphere mounted on low density foam structure (foreground) with broadband feed antenna (background). Mylar tape used for stability to prevent background movement upon sphere removal.

Low density polystyrene foam (one- or two-pound density) is a staple for mounting targets in RCS measurement systems with an open cell configuration that provides exceptional support strength while its permittivity of $\epsilon_r' = 1.038 - j10^{-5}$ delivers low monostatic RCS returns. The irregular addition of an inverted coffee cup is used to elevate the target (in this case a dielectric sphere) above the larger flat surface of the support

column below. The addition of mylar tape is used to secure the mounting structure such that insertion and removal of the target under test does not move the support structure from its original position. Such movement would negate the effectiveness of any post-measurement processing schemes to mitigate unwanted clutter sources.

The frequency of interest is from 8.2-12.4 GHz to validate results from biaxial assessments made by Knisely [3]. However, additional bandwidth from 6-13 GHz is utilized to ensure that later application of Fourier processing to mitigate extraneous scattering sources does not impinge on data within the desired 8.2-12.4 GHz region. Due to hardware limitations, measurements were limited to vertical polarization with respect to the horizon. The distance between the antenna and spheres was 3.8 m with a maximum target extent defined by the far field criteria (1.2) as

$$D_{max} \ll \sqrt{\frac{\lambda_{min} R}{2}} \sim 214\ mm. \tag{3.8}$$

This maximum target extent of 214 mm is more than all the spheres selected for this research (including the calibration cylinder (190.5 mm x 88.9 mm) except the Polystyrene 2# sphere (249.3 mm). As the RCS profile of this sphere as a function of frequency will show in Chapter IV the very low dielectric constant of ~1.04 causes negligible refraction of the incident planewave into the sphere, which in turn causes the front and rear specular points to be the dominant features. Thus, slightly under-illuminating this sphere does not degrade its RCS profile.

The RCS measurement scenario shown here can be viewed from the perspective of Linear Systems Theory. Whether an instrumentation radar, network analyzer, or Linear FM system is used to interrogate the target of interest, that signal at the receiver input is the

target's complex[4] measured scattered field, E_m^T, resulting from the target's actual (uncorrupted) scattered field, $E_a^T(f,p,\theta)$, corrupted by a band-limited complex linear system response $H(f,p,\theta)$ [46] which may be expressed as

$$E_m^T(f,p,\theta) = H(f,p,L)E_a^T(f,p,\theta), \tag{3.9}$$

where f is the operating frequency, p is the transmit and receive polarization vector direction[5], θ represents the generalized angle of incidence upon the target, and L is loss in the system (RF cables, free space spreading loss, the frequency response of the illuminating antenna, duty cycle, and internal receiver losses)[6]. This system response, H, does not incorporate error associated with the incident field or any interactions between the target and its environment. At this point, the actual (uncorrupted) scattered field of the target and the system response are unknown. Repeating (3.9) for a reference of known scattered field, E_a^R, may be expressed as

$$E_m^R(f,p,\theta) = H(f,p,L)E_a^R(f,p,\theta), \tag{3.10}$$

where $E_a^R(f,p,\theta)$ and $E_m^R(f,p,\theta)$ are the actual (uncorrupted) and measured complex scattered fields of the reference. The linear system relationship of (3.9) and (3.10) may be viewed graphically in Figure 9.

[4] Complex scattered field having both magnitude and phase.
[5] Polarization can take on multiple states, including linear, circular, and cross polarization. For the purposes of this research, all polarization is assumed to be linear, either vertical or horizontal with respect to gravity.
[6] Despite the use of a Linear Systems model to represent the RCS measurements system, not all signals comprising the system response are linear. For example, the antenna response as a function of frequency is usually quite non-linear. The reason a Linear Systems model is effective in the presence of non-linear features, is due to the linearization of those responses via the calibration process where the linear *and* non-linear features of the system are canceled when the target response is divided by the reference response. The same system response is contained in both, nullifying the impact of non-linear system responses. Both linear and non-linear features of the target of interest are retained as they are not within the system response.

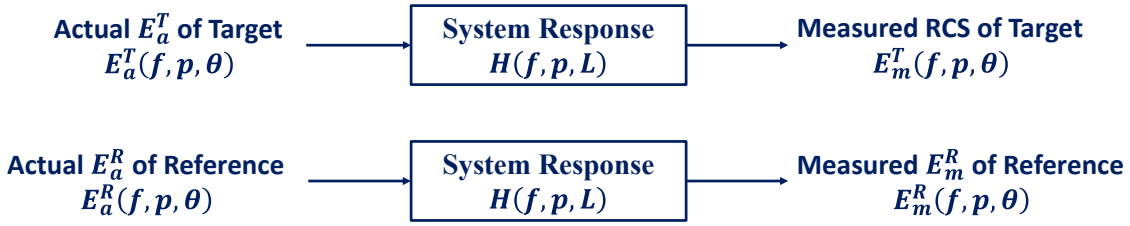

Figure 9. Linear Systems representation of an RCS measurement system. The top diagram represents the corruption of the uncorrupted target scattered field caused by the system response resulting in the measured target scattered field. The bottom diagram represents the corruption of the uncorrupted reference scattered field caused by the same system response resulting in the measured reference scattered field.

With the measurement of a known reference, the system response is now determined by

$$H(f,p,\ L) = \frac{E_m^R(f,p,\theta)}{E_a^R(f,p,\theta)}. \tag{3.11}$$

Inserting (3.11) into (3.9) yields the uncorrupted "calibrated" target scattered field as

$$E_a^T(f,p,\theta) = \frac{E_m^T(f,p,\theta)}{E_m^R(f,p,\theta)} E_a^R(f,p,\theta). \tag{3.12}$$

The calibrated phase of the complex scattered field E_a^T in (3.12) is retained and of interest for later use in potential inversions from measured scattered fields to permittivity. The magnitude, however, is in units of Volts/meter and this research seeks RCS, a scalar quantity in units of square meters. Inserting E_a^T into (3.1) with $\left|E^i\right| = 1\ (V/m)$ and multiplying by the scalar 4π in the far field limit results in RCS (m^2) [47] as described in (3.6), with the phase of E_a^T described by (3.7) . The reference used for the five dielectric sphere measurements was a right circular cylinder, commonly referred to as a "Squat

Cylinder,"[7] whose dimensions are 190.5 mm x 88.9 mm. The predicted RCS of the cylinder and its scattered field phase are shown in Figure 10. Cylinders are favored as calibration targets in RCS measurements due to their:

1. Well-behaved broadband frequency response (beyond the resonance region).
2. Ease of manufacturing and validation of as-built dimensions.
3. Ease of computation using standard full-wave solvers.
4. Ease of mounting on low density foam supports.
5. Low interaction with foam support structures.

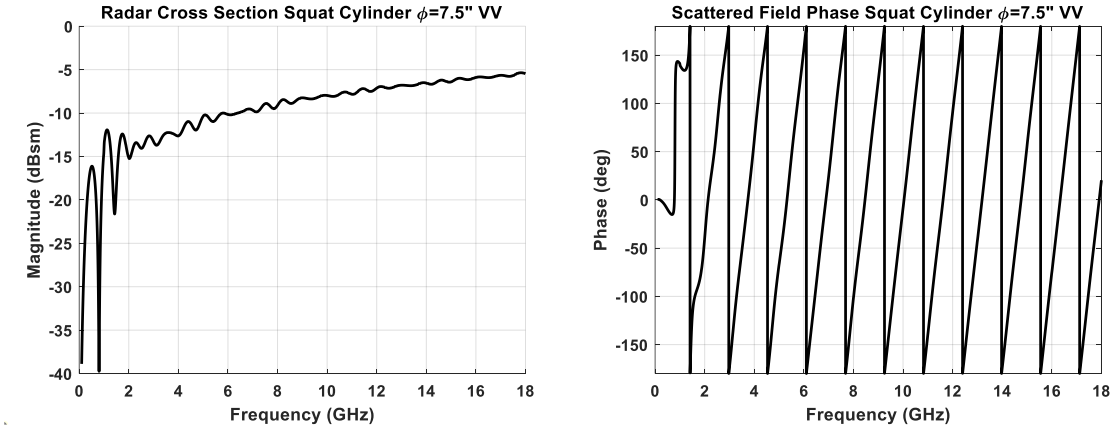

Figure 10. Computed RCS (left) and far-zone scattered field phase (right) for a 190.5 mm diameter calibration squat cylinder.

The inherent assumption of (3.12) is that there are no extraneous contributions to the measured fields E_m^T and E_m^R other than the target and reference respectively. In practice, both quantities are perturbed by a variety of error sources, including noise, which must be

[7] The term squat cylinder refers to the ratio of the cylinder diameter to the height which is close to a factor of two. This ratio has been useful in providing a broadband flat frequency response while driving the first null of the resonance region lower in frequency. As the ratio of diameter to height increases, additional nulls appear in the spectrum and the cylinder loses its value as a reference target since its scattered field magnitude lies in the denominator of (3.12), resulting in near divide-by-zero scenarios.

mitigated if the desired E_a^T is to have the least uncertainty. In the measured sphere configuration, the direct coupling between the network analyzer transmit and receive ports and the impedance discontinuity between the antenna and free space are the largest error sources, followed by internal reflections from the Agilent Network Analyzer, and assorted errors from RF connectors and the target mounting structure. A diagram of the measurement configuration and how these potential errors are manifested is shown in Figure 11, where blue represents range hardware or structures, green represents the sphere scattered field, and red represents undesired signals such as transmit-receive coupling through a broadband circulator, antenna mismatch at the feed point, antenna mismatch at the antenna-free space interface, sphere-foam mount scattered field, and side and back wall absorber scattered fields.

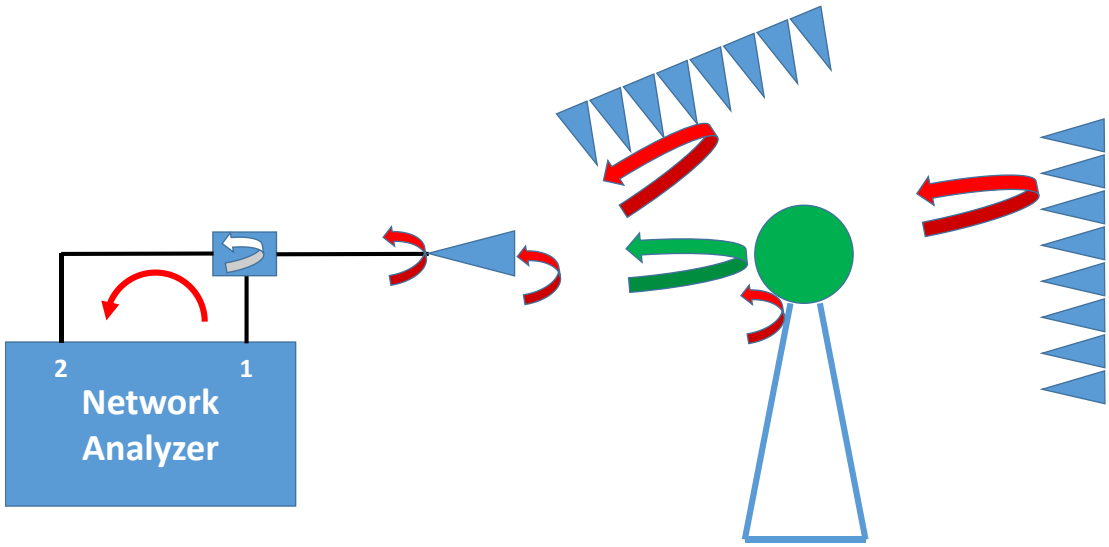

Figure 11. Sphere RCS measurement configuration and error source identification. Blue represents range hardware or structure. Green represents sphere and desired scattered field. Red represents undesired signals: transmit-receive coupling through broadband circulator, antenna mismatch at feed point, antenna mismatch at antenna – free space interface, sphere-foam mount scattered field, and side and back wall absorber scattered field.

Many RCS measurement systems are equipped with high speed pin-diode switches which turn the receiver on only when the desired target return is expected.[8] One example of such a switch is shown in Figure 12. While these switches are very effective in mitigating the contributions from a variety of extraneous signals, they are also costly to implement and, in some circumstances, difficult to use for untrained operators. In those cases, alternative methods must be employed to mitigate the contributions from unwanted signals that corrupt the measured scattered field E_m^T.

Figure 12. Sample high-speed RF pin diode switch. Image and component courtesy of Fairview Microwave (www.fairview.com).

There are two principal methods of mitigating extraneous signal contributions in addition[9] to the use of pin switches: vector background subtraction[10] and software gating [48]. As a linear system, the total scattered field is the superposition of all the available

[8] This is often referred to as a receiver hardware gate.
[9] Pin switches do not preclude the use of vector background subtraction and additional software gating. Most often, the direct scattering from the target or reference mounting structure falls withing the pulse width of the pin switch, thus requiring additional techniques to mitigate its contribution to the total scattered field.
[10] Also commonly referred to as coherent background subtraction.

scattered fields that enter the receiver in addition to the target of interest.[11] For example, assume that the scattered field is measured from a Teflon sphere mounted on a foam support column. The total complex signal at the receiver, E_m^T, is the measured scattered field from the sphere, E_m^S, in addition to the scattered field from: the foam column, E_m^C; the back wall, E_m^W; interactions between the sphere and the column, E_m^I; the impedance mismatch between the antenna and free space, E_m^{AF}; the impedance mismatch between the coax and the antenna, E_m^V; the coupling between the transmit and receive channels, E_m^{TR}; mismatches within the receiver itself, E_m^{Rx}; and receiver noise, N. This total received signal may be expressed as

$$E_m^T = E_m^S + E_m^C + E_m^W + E_m^I + E_m^{AF} + E_m^V + E_m^{TR} + E_m^{Rx} + N_T. \tag{3.13}$$

The same measurement is now considered without the sphere present expressed as the sphere background, E_m^B, according to

$$E_m^B = 0 + E_m^C + E_m^W + 0 + E_m^{AF} + E_m^V + E_m^{TR} + E_m^{Rx} + N_B. \tag{3.14}$$

Note that in the background measurement all scattered field components remain except the target itself and any interactions between the target and the measurement environment. Subtracting (3.14) from (3.13) yields

$$E_m^D = E_m^s + E_m^I + N_T - N_B, \tag{3.15}$$

where E_m^D is the complex difference between (3.14) and (3.13), and N_T and N_B are additive noise for the target and background measurements respectively, each is a circularly

[11] There are conditions under which superposition fails. For example, when a conductive target is placed on a conductive support structure, the incident field may induce shared currents on both the target and support when the frequency is sufficiently low. When this occurs, the scattering from the target and its support may be indistinguishable from the other. A similar problem occurs when a dielectric target is placed in contact with a dielectric support which directly impacts measurement uncertainty.

complex Gaussian independent random variable with zero mean and identical variance $\langle|N|^2\rangle$ since the receive channel is the same for the target and background measurements [46][12]. Subtracting the background from the target is the same as multiplying the background by the phasor term $e^{j\pi}$. Since N is circularly Gaussian, this complex multiply has no effect on the distribution of N [49]. It can also be shown that the difference between the target and background noise has zero mean and variance $2\langle|N|^2\rangle$ and standard deviation $\sqrt{2\langle|N|^2\rangle} = \sqrt{2}\sqrt{\langle|N|^2\rangle}$. This is an important result in that the noise standard deviation increases by a factor of two during the subtraction process illustrated in Figure 13. While this increase is not usually the driver in measurement uncertainty, it can be a factor for measurements of low-level scattered fields whose magnitude is close to the noise magnitude in the receiver. This condition is usually referred to as low signal-to-noise-ratio or abbreviated as low SNR. From a measurement practitioner standpoint, the doubling of the noise standard deviation results in a loss of sensitivity of $20\log_{10}\left[\sqrt{2}\sqrt{\langle|N|^2\rangle}\right] = 20\log_{10}\sqrt{\langle|N|^2\rangle} + 3\ dB$, or a 3dB increase in the minimum detectable signal [50].

[12] Despite the target and background measurements traveling through the same channel architecture, the real and imaginary components of the noise may have different variances due to what is referred to as an imbalance in I/Q Circularity. While this is possible in radar receivers and network analyzers, most contemporary versions of these instruments do not have this problem. In those that do, this imbalance may be incorporated into an uncertainty model.

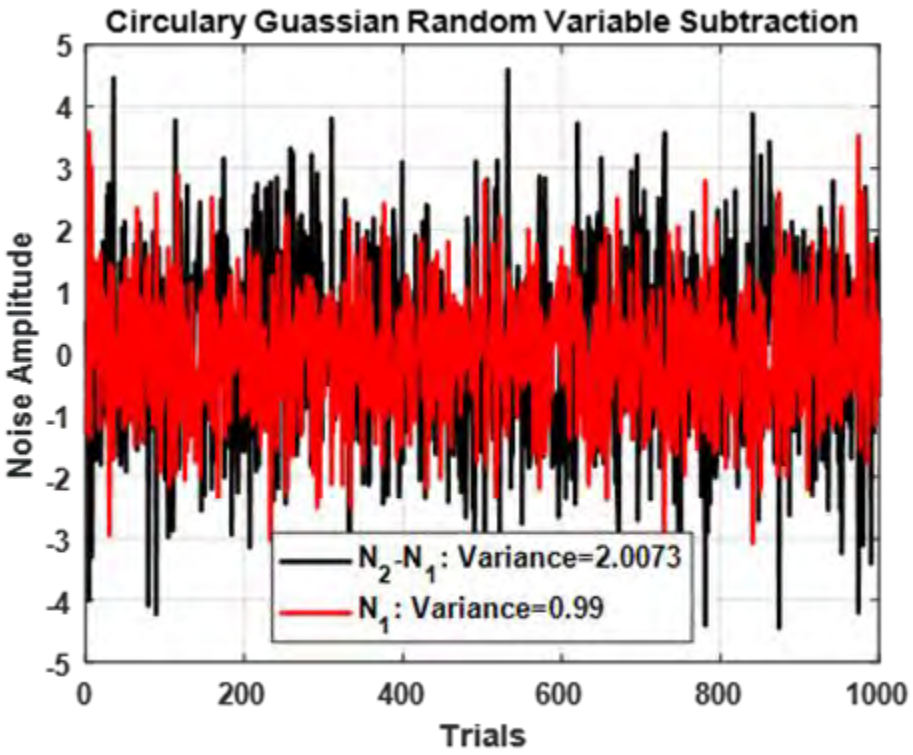

Figure 13. Demonstration of subtraction between two independent circularly Gaussian random variables N_1 and N_2, generated with 1000 samples from the MATLAB Gaussian random number generator. As expected, the variance of the subtracted random variables (N_2-N_1) is twice that of only one random variable (N_1).

The calibration function of (3.12) may now incorporate vector background subtraction and be restated as

$$E_a^T(f,p,\theta) = \frac{E_m^T(f,p,\theta) - E_m^{T_b}(f,p,\theta)}{E_m^R(f,p,\theta) - E_m^{R_b}(f,p,\theta)} E_a^R(f,p,\theta), \qquad (3.16)$$

where the new variables $E_m^{T_b}$ and $E_m^{R_b}$ represent the target and reference background scattered fields respectively [13].

[13] Target and reference backgrounds are listed separately to indicate that there may be two completely independent mounting structures for the target and reference shapes, each having a very different scattered field response as a function of frequency, polarization, and incident angle.

As previously stated, there are two principle means of mitigating unwanted sources of error in RCS measurements in addition to hardware gates: vector background subtraction and software gating. Having described vector background subtraction, attention will now be given to software gating which may be applied directly in some commercial network analyzers or in software applications such as MATLAB.

Referring again to a linear systems model of the RCS measurement system, the calibrated measurement of the target under test in (3.16) can be viewed from either the frequency domain or time domain via the Fourier Transform pair

$$E_a^T(f,p,\theta) \Leftrightarrow E_a^T(t,p,\theta). \tag{3.17}$$

The software gate is a time domain function $g(t)$ in the time domain or $G(f)$ in the frequency domain. The role of $g(t)$ is to isolate desired signals from unwanted signals in the time domain by attenuating the contribution of the unwanted signals. This can be performed in the time domain as a Hadamard Product $E_a^T(t,p,\theta) \odot g(t)$ or as a convolution in the frequency domain as $E_a^T(f,p,\theta) * G(f)$. The Fourier Transform pair of a sample software gate is shown in Figure 14.

$$g(t) \Leftrightarrow G(f)$$

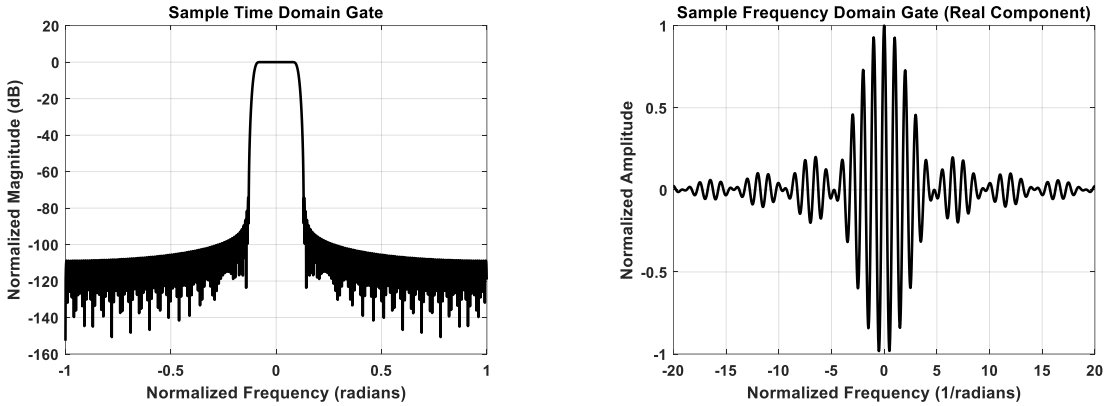

Figure 14. Sample software gate applied in either the time domain as a Hadamard product (left) or in the frequency domain as a convolution (right). The time domain plot (left) is shown in decibel format while the real portion of the frequency domain gate is shown to be consistent with traditional nomenclature for each domain.

In this research, the time domain gate, $g(t)$, was applied using a Finite Impulse Response (FIR) low-pass filter defined by Lathi [51]. Such a design provides a quality flat magnitude response in the passband as well as linear phase, and steep skirts for effective cutoff. Numerous approaches to software gating have been reported, each with their own advantages and disadvantages [52-56].

To illustrate the application of software gating, consider two scattering sources, one of whom is desired at 0 ns while the other is located 2 ns away and is lower in magnitude by 10 dB. This type of separation in time may correspond in practice to the difference in time between the scattering response of a target and that of the mismatch between the antenna and free space. The frequency and time dependent response of the superposition of these two sources are shown in Figure 15.

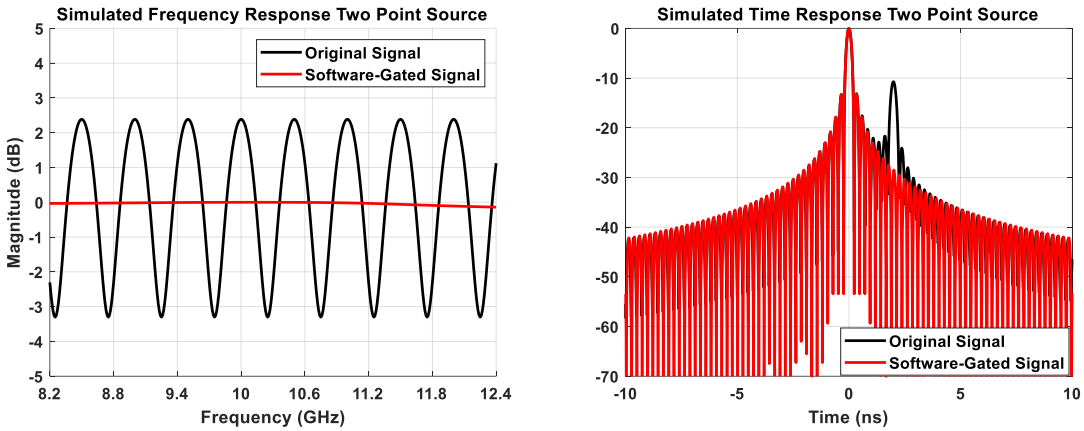

Figure 15. Simulated frequency domain (left) and time domain (right) responses from two scattering sources illuminated from 8.2-12.4 GHz, one located at t=0 ns with a magnitude 0.0 dB and the second source at t=2 ns with a magnitude of -10 dB compared to the first. In both plots, the black curve corresponds to the original signal while the red curve corresponds to the application of a multiplicative Finite Impulse Response (FIR) low pass filter or gate in the time domain. This filter excludes the secondary lower response from the combined signal. Note the slight degradation in the frequency response due to coupling between the two signals in time.

To further illustrate the impact of vector subtraction and time gating on calibration, consider the implementation of (3.12) and (3.16) in the frequency and time domain in Figure 16 and Figure 17, respectively. In both figures, four curves are presented with their calibration function or its Fourier Transform to the right. In both figures, the magenta curve shows the Teflon sphere plus the background without any subtraction or gating applied to (3.12). The black curve shows the Teflon sphere with background subtraction but without any gating applied to (3.16). The red curve shows the Teflon sphere with both vector subtraction and gating applied to (3.16). Finally, the blue curve shows the optimal subtracted background with gating applied to (3.16), inserting $E_{m_2}^{T_b} - E_{m_1}^{T_b}$ into the numerator of (3.16), providing practitioners with the minimum RCS (noise or clutter limit) under the current measurement configuration and the maximum possible separation between the signal of interest and the noise or clutter limit. At the bottom of the time

domain presentation of Figure 17, letters A-E at the bottom of the time domain plot indicate the location of identifiable structures in the chamber with respect to the position of the target: A: Antenna Interface, B: Absorber Wall Near Antenna, C: Teflon Sphere, D: Back Wall Absorber, and E: Transmit/Receive Coupling.

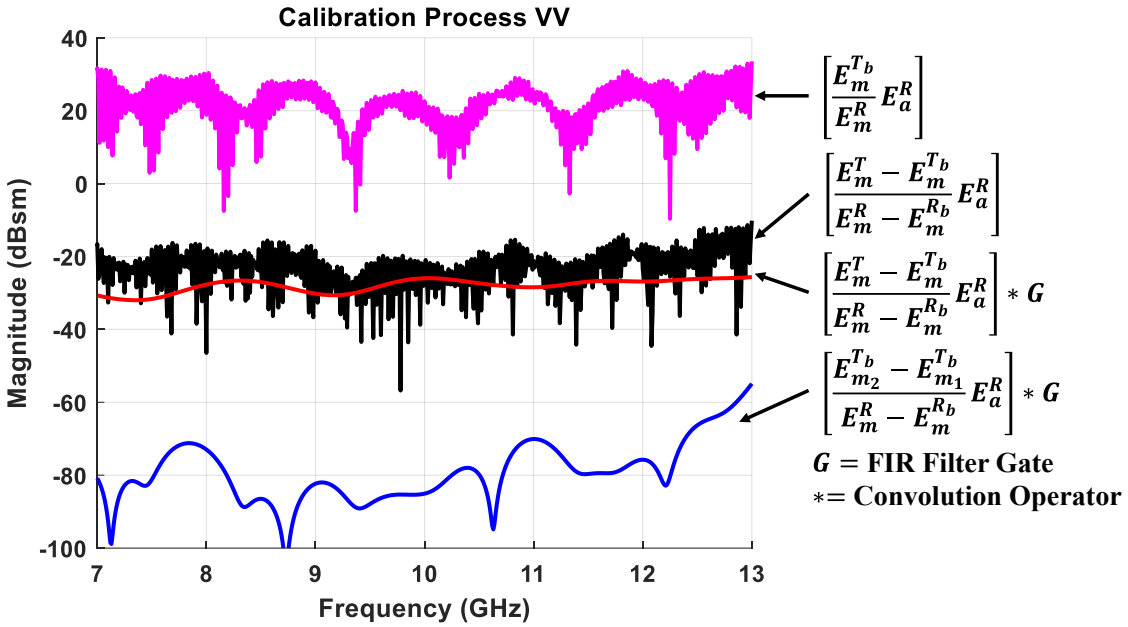

Figure 16. Illustration of the impact of vector subtraction on calibration using (3.12) and (3.16) in the frequency domain. Four curves are presented with their calibration function to the right. The magenta curve shows the Teflon sphere plus the background without any subtraction or gating applied to (3.12). The black curve shows the Teflon sphere with background subtraction but without any gating applied to (3.16). The red curve shows the Teflon sphere with both vector subtraction and gating applied to (3.16). The blue curve shows the optimal subtracted background with gating applied to (3.16), providing practitioners with the minimum RCS (noise or clutter limit) under the current measurement configuration and the maximum possible separation between the signal of interest and the noise or clutter limit.

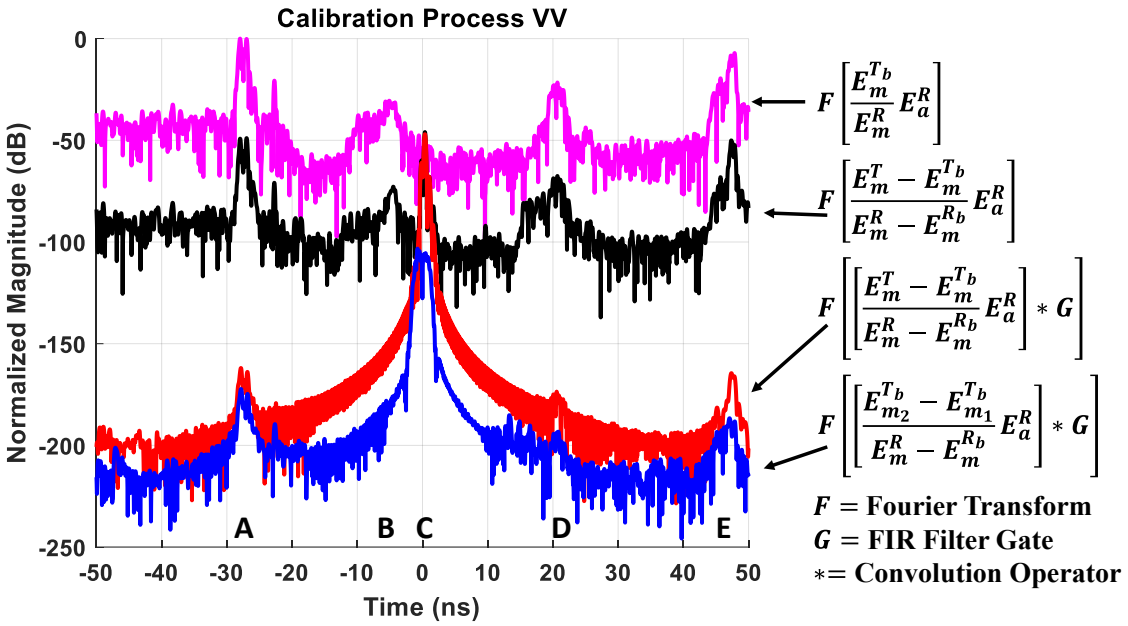

Figure 17. Illustration of the impact of vector subtraction on calibration using (3.12) and (3.16) in the time domain. Four curves are presented with the Fourier Transform of their calibration function to the right. The magenta curve shows the Teflon sphere plus the background without any subtraction or gating applied to (3.12). The black curve shows the Teflon sphere with background subtraction but without any gating applied to (3.16). The red curve shows the Teflon sphere with both vector subtraction and gating applied to (3.16). The blue curve shows the optimal subtracted background with gating applied to (3.16), providing practitioners with the minimum RCS (noise or clutter limit) under the current measurement configuration and the maximum possible separation between the signal of interest and the noise or clutter limit. Letters at the bottom of the time domain plot indicate the location of identifiable structures in chamber with respect to the position of the target: A: Antenna Interface, B: Absorber Wall Near Antenna, C: Teflon Sphere, D: Back Wall Absorber, and E: Transmit/Receive Coupling.

The frequency and time domain presentations shown in Figure 16 and Figure 17 reveal that both vector background subtraction and time domain gating are essential tools in recovering the measured scattered field of interest. To determine the efficacy of the calibration and signal recovery process, the RCS and time domain responses of the Teflon sphere are compared with the same presentations created from the Mie Series shown in Figure 18. The time presentation clearly reveals that the scattered field profile as a function

of time is well represented. However, there is an equally clear error manifesting as a bias in the frequency domain. This error cannot be related to errors in sphere diameter or the Mie series dielectric constant as minor errors in either would result in a shift of the frequency response to the left or right. In addition, the error cannot be associated with illumination irregularities since the sphere was physically placed at the mid-height of the calibration cylinder, thus receiving the same incident field distribution. Rather, the bias is directly associated with an additional loss component corrupting the inherent loss term of the sphere permittivity. In other words, the Teflon sphere is no longer Teflon when in the presence of the dielectric support structure. Rather, the calibrated-subtracted response is now the Teflon sphere in the presence of the dielectric support. This is an important conclusion potentially limiting the efficacy of this method – specifically at perpendicular polarization with respect to the target support normal and in the context of a low loss tangent target. Also, while traditional low-density Polystyrene foam is the support structure-of-choice by RCS measurement practitioners, those supports are most commonly open-cell configurations, causing their effective permittivity to be close to air. Whereas, the inverted Polystyrene coffee cup support is a closed-cell structure and may have perturbed the Teflon sphere in ways that an open-cell foam would not.

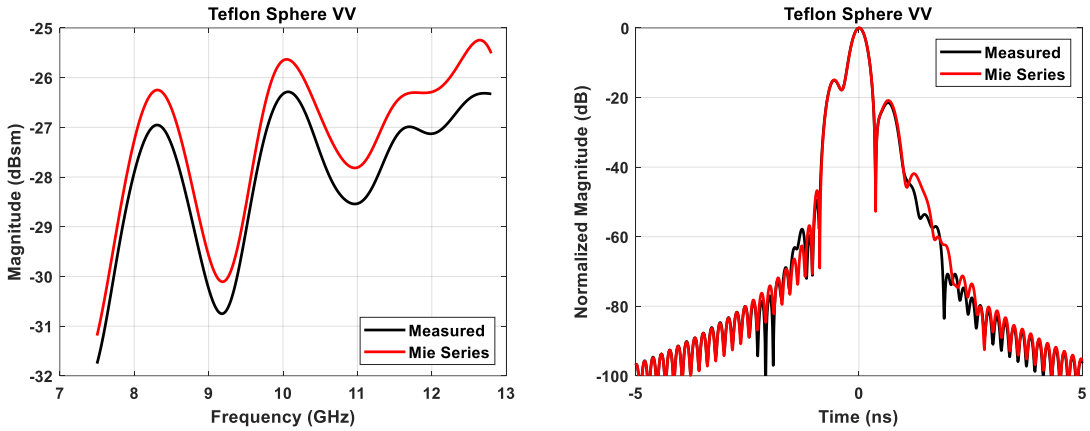

Figure 18. Measured RCS of 50.8 mm Teflon sphere using vector background subtraction and time domain gating in the frequency domain (left-black) and time domain (right-black). The Mie series for the Teflon sphere in the frequency and time domain is shown by the red curve. The visible bias error in the frequency domain is caused by imposed loss due to the presence of the foam support.

To establish a first-order estimate of the impact of the coffee cup support (Polystyrene $\epsilon_r' = 2.5 - j0.00041$) in contact[14] with the sphere (Teflon/PTFE $\epsilon_r' = 2.5 - j0.00041$), a full-wave solution of the sphere over the coffee cup bottom disk was computed from 8-12 GHz with results shown in Figure 19. The presence of the Polystyrene support accounted for the measured loss of magnitude across the spectrum. The central issue related to the presence of the Polystyrene disk is that it denies any opportunity to achieve a quality loss tangent estimate of the Teflon as shown in Figure 20. Here, the effective Teflon sphere permittivity was computed with the Mie Series using a complex permittivity of $\epsilon_r' = 2.05 - j0.0123$ resulting in very good agreement with the measured RCS. While the dielectric constant remains unchanged, the presence of the Polystyrene structure is a limiting factor in quality inversions despite the use of measurement best practices. This error will inevitably impact the scattered fields and subsequent inversions for the other

[14] Due to mesh restrictions in FEKO, the Teflon sphere was placed 0.508 mm (0.02 inches) above the Polystyrene disk.

spheres and the four dielectric cubes yet to be presented. An additional way to understand the impact of the presence of the Polystyrene support, the RCS of the disk itself, is examined in Figure 21. The RCS of the Polystyrene disk by itself compared to the RCS of the Teflon sphere while on the mount is negligible. This underscores the impact of mutual coupling between the sphere and the disk as a primary source of measured scattered field error and not the direct scattering from the mount itself.

Thus far, the impact of the disk as an error source has been limited to vertical polarization. Due to hardware limitations at the time of sphere testing, the antenna was limited to vertical polarization. However, both polarizations were utilized at the time of cube testing in a modified measurement configuration that will be described in Section 3.2.

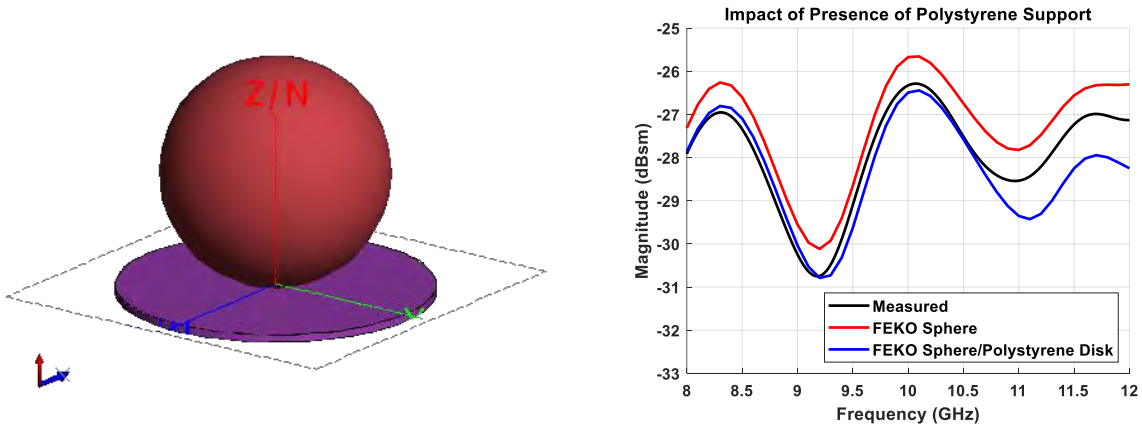

Figure 19. FEKO representation of a Teflon sphere (ε_r=2.05-j0.00041) 0.508 mm above a Polystyrene disk (ε_r=2. 5-j0.00041) with thickness of 1.651 mm and a diameter of 69.85 mm (left) and RCS vs Frequency (right) of the measured sphere (black), FEKO prediction of the sphere alone (red), and FEKO prediction of the sphere on top of the Polystyrene (blue).

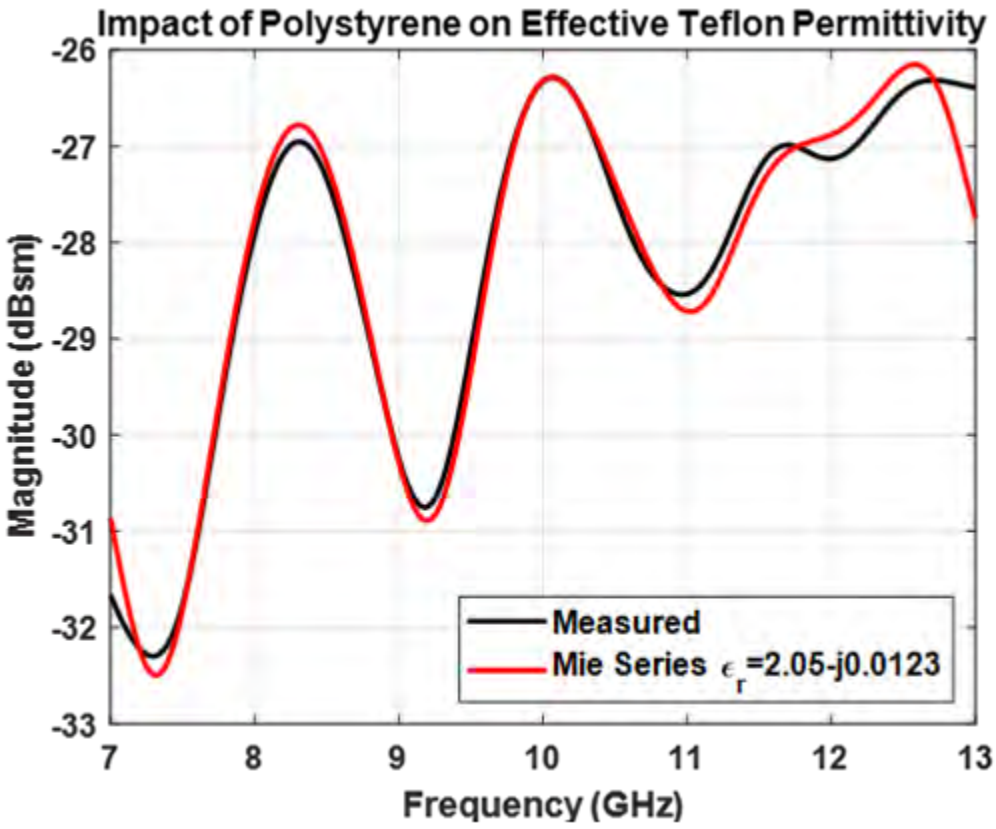

Figure 20. Measured RCS of Teflon sphere (εr=2.05-j0.00041) mounted on Polystyrene disk (εr=2. 5-j0.00041) (black) with an estimated effective permittivity of the same sphere using the Mie series (εr=2.05-j0.0123) (red).

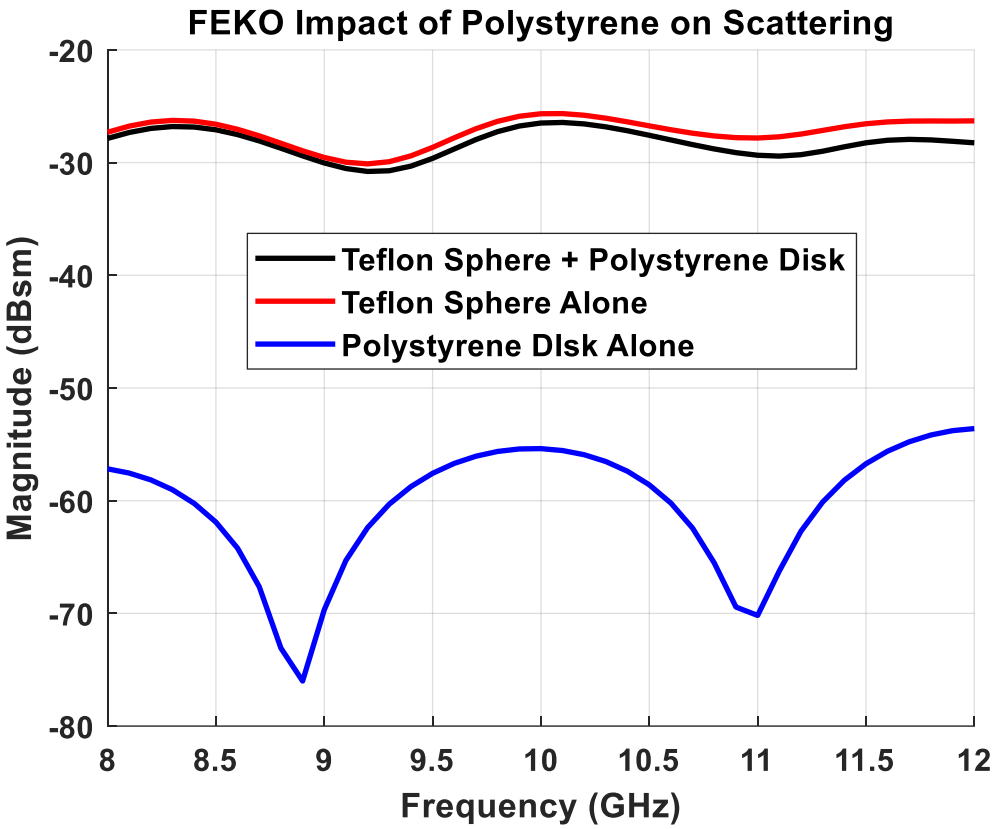

Figure 21. FEKO RCS of Teflon sphere mounted on Polystyrene disk (black), FEKO RCS of Teflon sphere alone (red), and FEKO RCS of Polystyrene disk alone (blue).

Having established a foundation for dielectric sphere scattering, a configuration to measure it, and mutual coupling as the most significant error impacting a quality inversion, the following order of measurements is used for each of the five dielectric spheres under consideration and forms the baseline procedure to be used for measuring the RCS of the four dielectric cubes:

1. Target Background: Measure the frequency response of the sphere mounting structure without the sphere present.

2. Target Sphere: Measure the frequency response of the sphere mounting structure with the sphere present.

3. Reference Background: Measure the frequency response of the reference mounting structure without the reference present.

4. Reference Cylinder: Measure the frequency response of the reference mounting structure with the reference present.
5. Apply (3.16) with time domain gating.
6. Estimate the sphere permittivity.

Sphere Permittivity Estimation.

Permittivity inversion for the spheres is achieved through a non-linear optimizer which minimizes the least squares difference between the measured and estimated broadband RCS magnitude and scattered field phase. This broadband approach exploits variations in the frequency response assuming the sphere permittivity is constant over the band of interest. This approach limits the efficacy of the method to non-dispersive materials or dispersive materials over a narrow bandwidth. The optimizer minimizes the objective function, f_{obj}, according to

$$f_{obj} = min \sum_{k=1}^{N} \left[|\bar{\sigma}_m - \bar{\sigma}_e(\epsilon_r)|_k + \left|\bar{\phi}_m - \bar{\phi}_e(\epsilon_r)\right|_k \right] \tag{3.18}$$

where $\bar{\sigma}_m$ and $\bar{\sigma}_e$ are the measured and estimated mean-subtracted $20log(\sigma_c)$ from (3.6) respectively. $\bar{\phi}_m$ and $\bar{\phi}_e$ are the measured and estimated mean-subtracted $tan^{-1}(\sigma_c)$ from (3.7) respectively. N is the number of frequencies used in the minimization and k is the frequency index selected from the available measured bandwidth. The range of k is selected based on artifacts imposed by the FIR filter at the band edges. Inclusion of band edge artifacts imposes artificial errors in permittivity estimation. Subtraction of the mean minimizes magnitude and phase bias from calibration errors and mutual coupling between the sphere and its mount as described earlier.

Explanation of Sphere Results.

The inversion process (3.18) was applied to the calibrated scattered field measurements of the five dielectric spheres described in Table 1 with the estimated permittivity for each, including differences as compared to published data (Table 1) and Von Hippel [39] shown in Table 2. Teflon, Acrylic and Alumina Oxide dielectric constants were within 0.1-0.49% of published values respectively. However, there was variance between their estimated and published loss tangents ranging from 1348-206% which is consistent with the mutual coupling between the spheres and the mounting disk. The Neoprene and Shungite dielectric variances are driven by unavailability of published permittivity data at X-band.

Table 2. Estimated permittivity of five dielectric spheres from inversion process with percent difference from various published sources and compared with Von Hippel.

Sphere Material	Estimated Permittivity		Difference % Published		Von Hippel		
	ϵ_r	$tan\,\delta$	ϵ_r	$tan\,\delta$	ϵ_r	$tan\,\delta$	f (GHz)
Teflon	2.053	3.04e-3	0.10	1348	2.08	3.7e-3	10
Polystyrene 2#	1.041	1.77e-3	0.36	1670	1.03	1.0e-4	3
Alumina 99.5%	9.848	3.06e-4	0.49	206	8.80	3.0e-4	1
Neoprene	3.726	1.78e-2	6.85	48	2.84	4.8e-2	3
Shungite	2.085	5.14e-1	x	x	x	x	x

To better visualize the convergence of the inversion algorithm as a function of permittivity, consider the mapping of the inverse of the objective function, $\frac{1}{f_{obj}}$, (3.18) at 10 GHz shown in Figure 22. In the case of Teflon (Figure 22 – left), there is great

responsiveness to the dielectric constant but no definable minimum with respect to the imaginary term. As loss increases as in the case of the Shungite sample, a well-defined minimum develops as shown in Figure 22 (right).

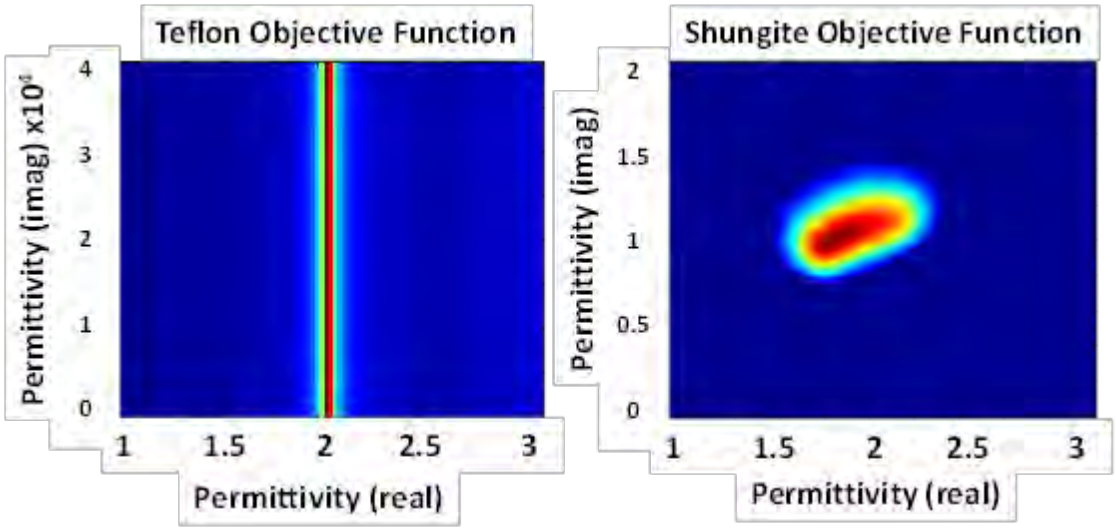

Figure 22. Inverse objective function mapping of low loss Teflon (left) and high loss Shungite (right). Mappings reveal the presence or absence of a global minimum along the real and imaginary axes.

A sensitivity analysis of RCS (3.6) as a function of real and imaginary components of permittivity is shown in Figure 23. Variations in real permittivity result in shifting magnitude and frequency response whereas variations in imaginary permittivity results primarily in a magnitude shift as a bias for two orders of magnitude from the near-lossless case. From these observations, it is important to note the following:

- A minimal change in RCS occurs as dielectric loss changes by an order of magnitude.
- An RCS measurement error of even 0.5 dB can result in an imaginary permittivity error of two orders of magnitude from the near-lossless condition.

These observations are consistent with the objective function for Teflon shown in Figure 22 (left). The response of RCS magnitude to variations in permittivity (real and imaginary) is an important result and will help determine initial guesses for estimation of anisotropic permittivity.

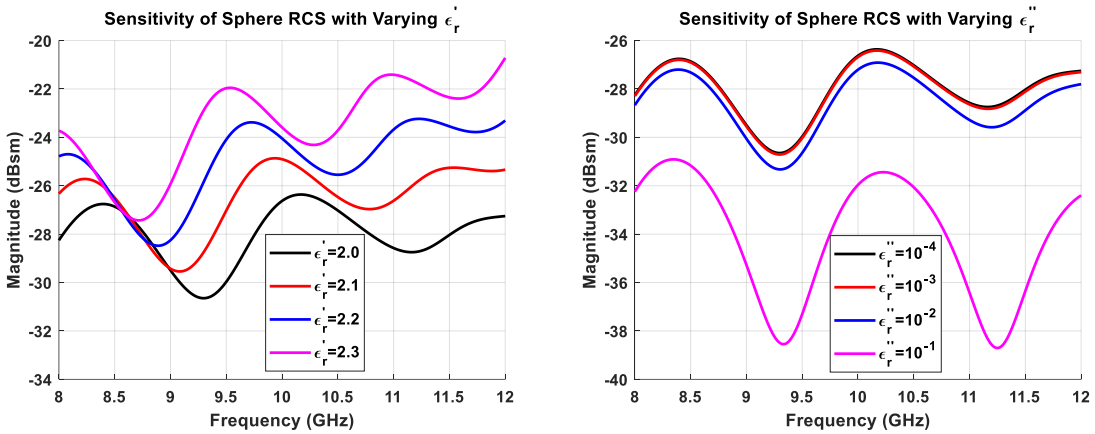

Figure 23. Sensitivity of RCS magnitude for dielectric sphere ε_r=2.0-j10^{-4} versus $\Delta\varepsilon'_r$ (left) and $\Delta\varepsilon''_r$ (right).

The results of the permittivity estimate for each sphere is shown as a comparison between the measured and inverted RCS and scattered field phase in Figure 24 through Figure 28. Each reconstruction shows excellent agreement with the measured data. While this agreement reflects a quality representation of the dielectric constant, it is not a quality representation of the loss tangent. Even in the case of a perfect measurement (e.g., no errors in calibration, incident field, diameter, etc.), the measured sphere scattered field will be corrupted by coupling between the sphere and the dielectric mounting surface.

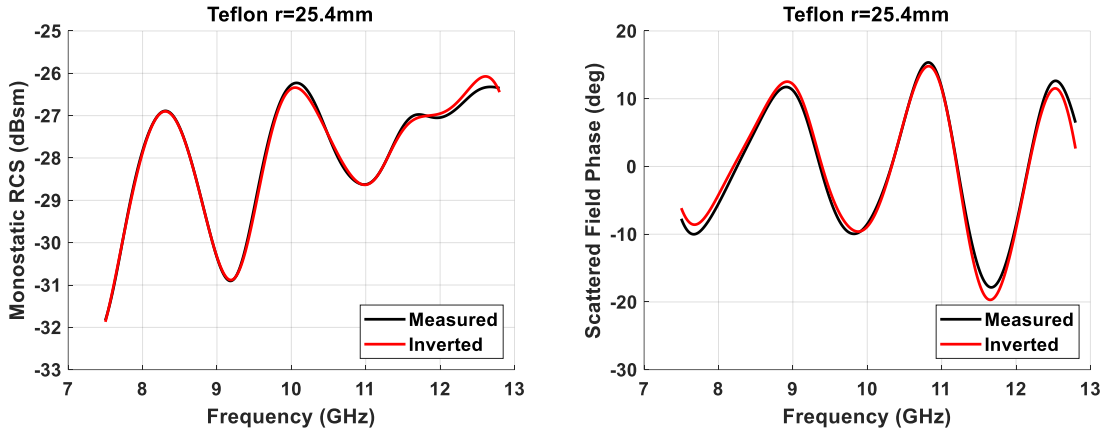

Figure 24. Comparison between measured and inverted RCS (left) and far-zone scattered field phase (right) for a Teflon sphere a=25.4 mm.

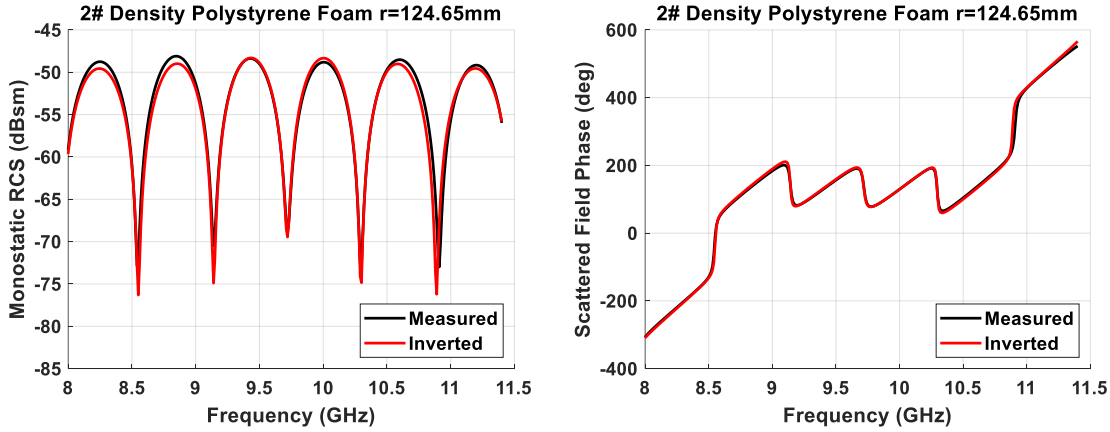

Figure 25. Comparison between measured and inverted RCS (left) and far-zone scattered field phase (right) for a Polystyrene Foam 2# sphere a=124.65 mm

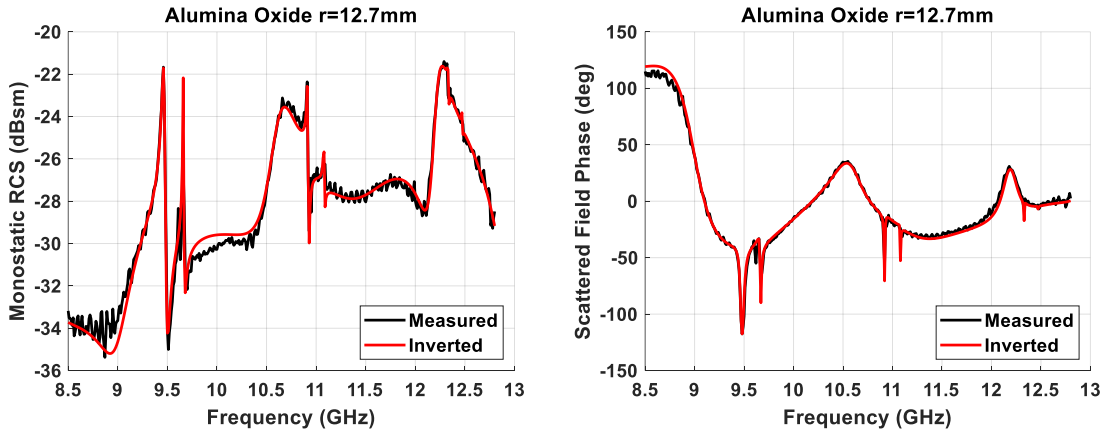

Figure 26. Comparison between measured and inverted RCS (left) and far-zone scattered field phase (right) for an Alumina Oxide (99.5%) sphere a=12.7 mm.

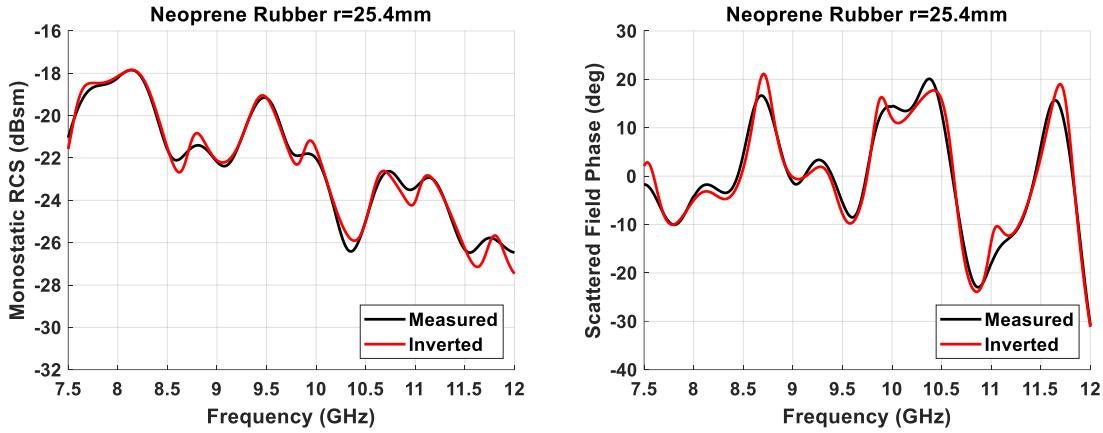

Figure 27. Comparison between measured and inverted RCS (left) and far-zone scattered field phase (right) for a Neoprene Rubber sphere a=25.4 mm.

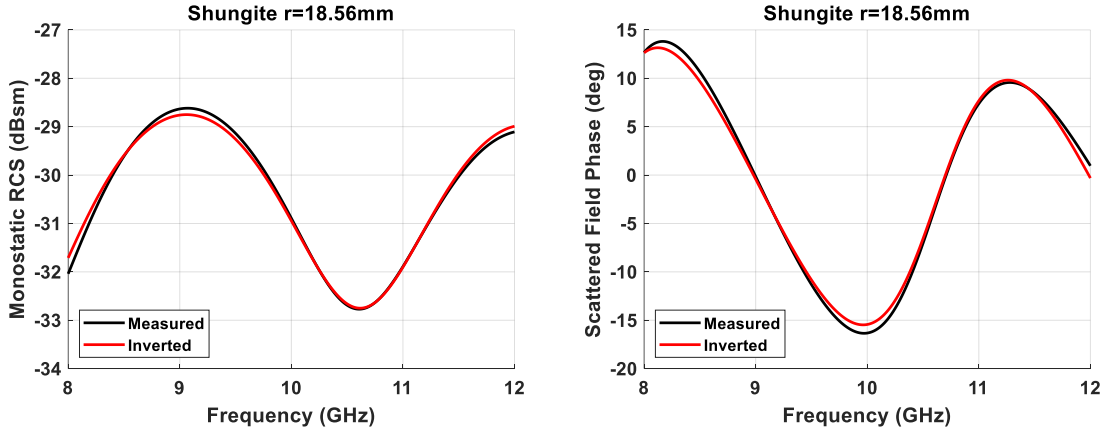

Figure 28. Comparison between measured and inverted RCS (left) and far-zone scattered field phase (right) for a Shungite sphere a=18.56 mm.

Uncertainty Considerations for Spheres.

To quantify uncertainty for each sphere measurement, a 1000-trial Monte Carlo approach was applied with uniformly distributed variables, $|\bar{\sigma}_m|$, $\bar{\phi}_m$, and sphere diameter, d. The limits of the Monte Carlo input distributions, based on far-field measurement requirements and physical diameter limitations are [-0.5, 0.5] dB, [-10, 10] degrees and [-.05, .05] mm respectively. The Monte Carlo process is shown graphically in Figure 29. The Monte Carlo results versus published values are shown in Table 3. It's important

to note that the Monte Carlo simulation does not include uncertainty contributions due to coupling between the target and support as this requires a priori knowledge of the material parameters.

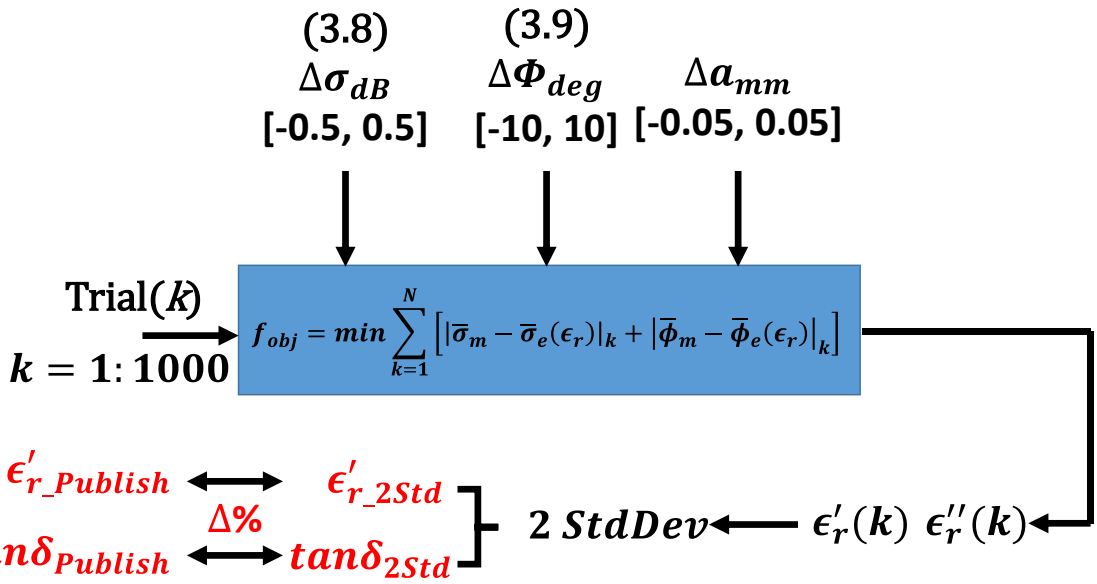

Figure 29. Monte Carlo 1000 trial uncertainty flow diagram reflecting percent difference between 2 Std Dev dielectric constant and loss tangent with same published values for the material shown in red.

Table 3. Monte Carlo uncertainty of measured dielectric constant and loss tangent of six dielectric spheres expressed as a percentage from the inverted complex permittivity.

Sphere Material	Measured Permittivity Uncertainty (±%)	Measured Loss Tangent Uncertainty (±%)
Teflon	0.58	68
Polystyrene	0.04	26
Alumina	0.24	278
Neoprene	0.16	10
Shungite	2.53	6

Sphere Permittivity Summary

A monostatic scattered field measurement system is presented as a tool for estimating the permittivity of isotropic spheres. The spheres are used as a first step in identifying critical measurement issues prior to estimating anisotropic permittivity using other shapes such as cuboids. A linear systems model is applied to the measurement system to mitigate system response and assorted measurement errors via vector background subtraction and time domain gating. Mutual coupling between the spheres and their dielectric support were shown to increase uncertainty in loss tangent estimates by approximately two orders of magnitude. A non-linear least squares optimization minimized the difference between measured complex scattered fields and the predicted fields from the Mie Series. The measured scattered fields from five dielectric spheres were inverted to estimate their respective complex permittivity and corresponding reconstructed complex scattered fields. A 1000-trial Monte Carlo uncertainty analysis was performed for the spheres revealing their two standard deviation difference with the same dielectric published permittivity.

The next section will address estimation of permittivity using isotropic and anisotropic cubes with a desire to match results from prior efforts by Knisely [3, 8]. Design parameters for effective media will be discussed along with FEKO as a forward solver choice. The section will close with a discussion on measurement methodology for the isotropic and isotropic cubes.

3.2 Estimation of Permittivity using Dielectric Cubes

The prior section showed success in estimating the dielectric constant of spheres at X-band, but significant error was seen in loss tangent estimation due to mutual coupling with the

dielectric target support. In this section we examine the use of dielectric cubes as a means of estimating anisotropic permittivity as described by (1.1). Represented in a rectangular coordinate system, dielectric cubes offer the potential of exciting one tensor axis at a time based on the polarization vector of the incident field. Unlike the sphere which is aspect invariant, the cube scattered field has three degrees of freedom with respect to the incident field vector: azimuth, elevation, and roll as shown in Figure 30. This measurement diversity provides independent scattered field information to aid in estimating permittivity but also increases uncertainty due to positioning errors in each of the three directions. Illumination in azimuth, elevation and roll is achieved by 90-degree rotation of the cube and then rotation is performed along the azimuth axis.

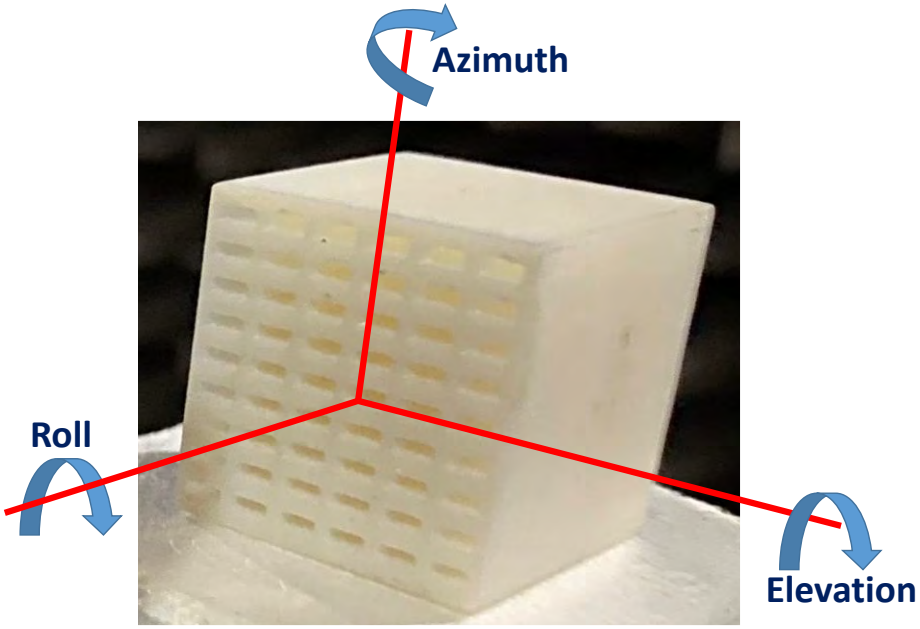

Figure 30. Biaxial cube showing three degrees of freedom.

The measured RCS from this three-dimensional data space can be viewed as a function of frequency, azimuth, and polarization at a time as shown in Figure 31. Here, the plot x-axis corresponds to incidence angle (degrees) with respect to the normal of the openings to

the air-filled occlusions (Figure 30) and the plot y-axis corresponds to the illumination frequency (GHz). The RCS magnitude (dBsm) is displayed as color whose corresponding RCS values are displayed at the color bar to the right of the plot. Above and below the plot are renderings of the biaxial cube in their respective orientations with respect to the incident field. While the primary frequency of interest is 8-12 GHz for validation purposes, the band of frequencies tested may be significantly wider as shown in the plot (4-20 GHz) to identify trends in scattering that may not be apparent in a narrower band. The interference patterns along the azimuth and frequency axes may offer insight as to incident angles or frequencies of interest to be used in the inversion process. For example, at approximately 8 GHz and 12 GHz respectively, there is a strong interference pattern which may indicate useful fixed frequency opportunities to estimate permittivity. However, 6 GHz, 10 GHz, and 14 GHz, RCS reside in a null and would not be a reliable data source due to the increased presence of noise resulting in increased uncertainty. The response below 6 GHz is outside the operational specifications of the radiating antenna and is thus dominated by error and not useful for inversion purposes. The global RCS representation for all four cubes is shown in Figure 32. Fixed frequency “slices” of Figure 31 along the azimuth direction show a one-dimensional extraction from the global presentation as shown in Figure 33.

One-dimensional slices from the global presentation provide detailed insight into the scattering as a function of azimuth and frequency. The slices can also be produced at fixed azimuth angles with frequency dependent responses as shown in Figure 34. In both fixed frequency and fixed azimuth representations of RCS, permittivity contrast between tensor parameters can be gleaned by changes in magnitude and frequency response for each polarization. For example, consider the RCS of the high contrast biaxial Knisely Cube

compared to RCS of a Teflon cube of the same size at 8 GHz as a function of azimuth and the same RCS as a function of frequency at a fixed azimuth of zero degrees shown in Figure 35. Scattering from the cube forces the periodicity of the fixed frequency representation to be 90 degrees. However, the differences and similarities at the principle azimuth angles of $n\pi/2$ reveal how close or dissimilar the dielectric constant is for each at that angle and polarization. In the case of the frequency dependent representation, an increase of dielectric constant causes a contraction within the frequency response and a magnitude shift. Both cause-and-effect observations are essential to initial estimates in the inversion process. Beginning with a reference material whose permittivity is well known, one can make educated guess regarding initial tensor axis permittivity. Achieving a close approximation to the actual permittivity can be performed manually which then affords a minimum amount of automated optimization by the full wave forward solver. Without this initial estimate concept, the optimizer will inevitably spend valuable time seeking a better estimate.

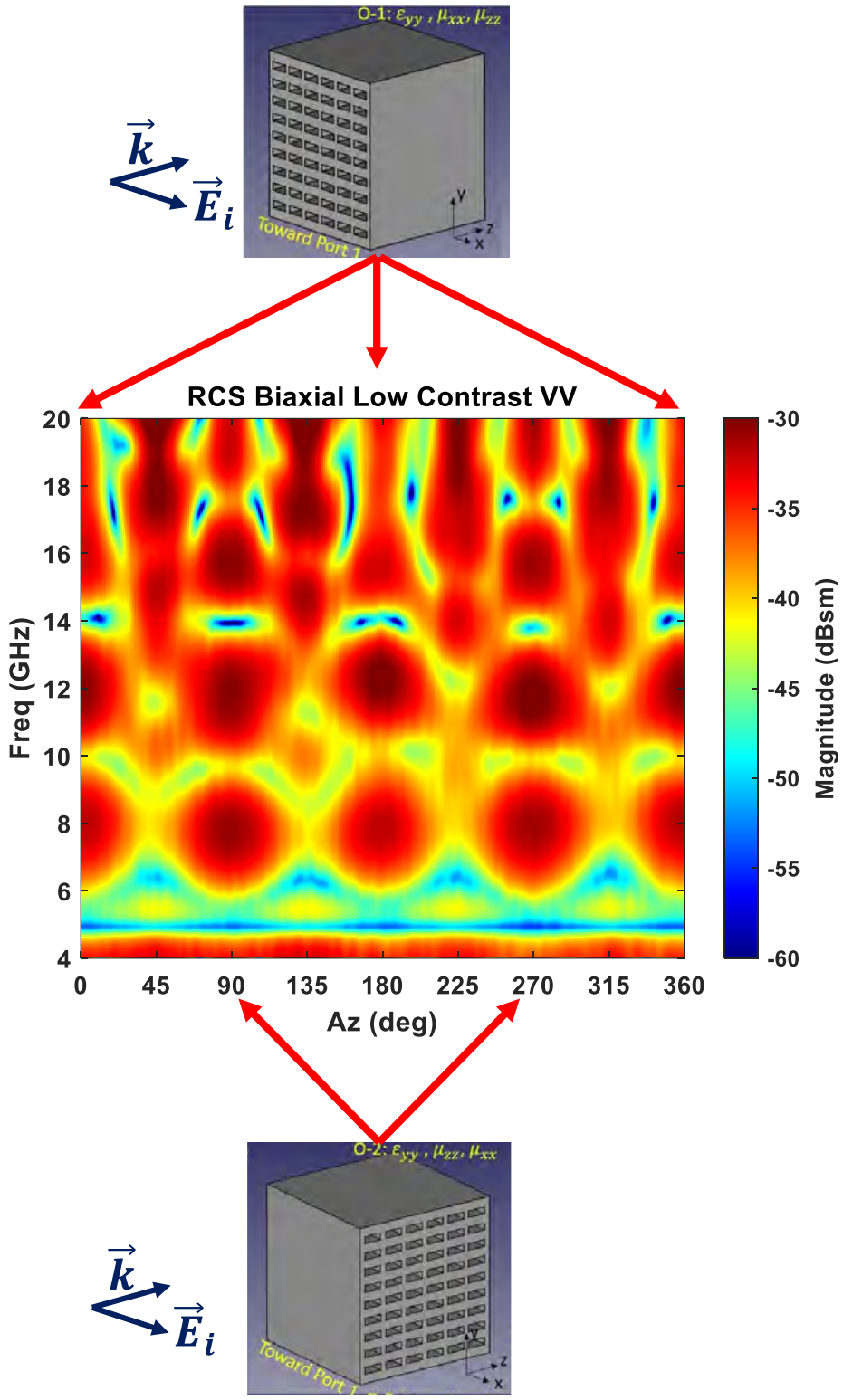

Figure 31. Global presentation of measured RCS of Knisely low contrast biaxial cube as a function of frequency and azimuth. Above and below the global plot are the orientations of the cube with respect to the incident field.

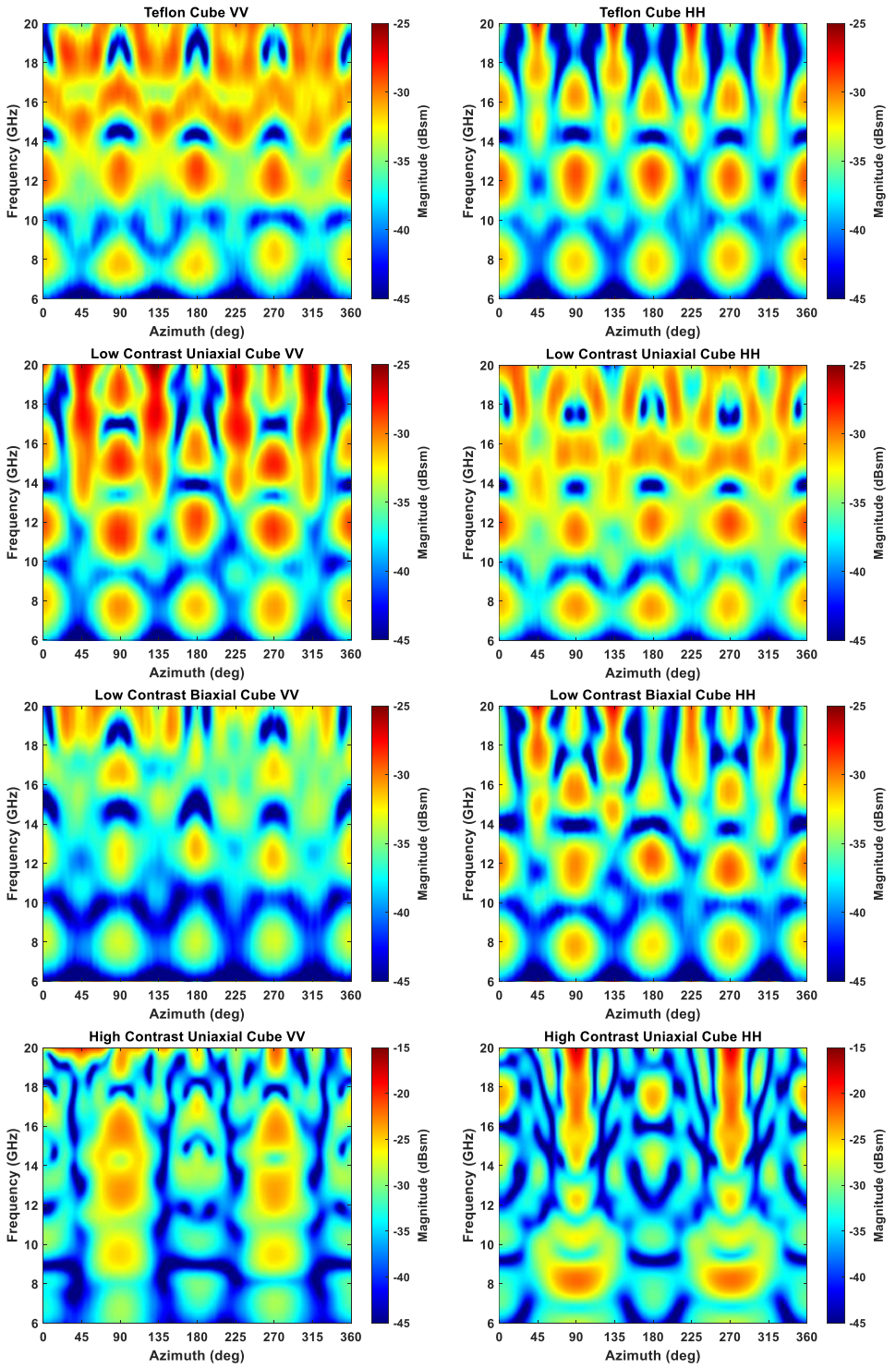

Figure 32. Measured global RCS presentations VV (left) and HH (right) from top to bottom: Teflon, low contrast uniaxial, low contrast biaxial, and high contrast uniaxial. Color axis the same for all except high contrast uniaxial for presentation purposes.

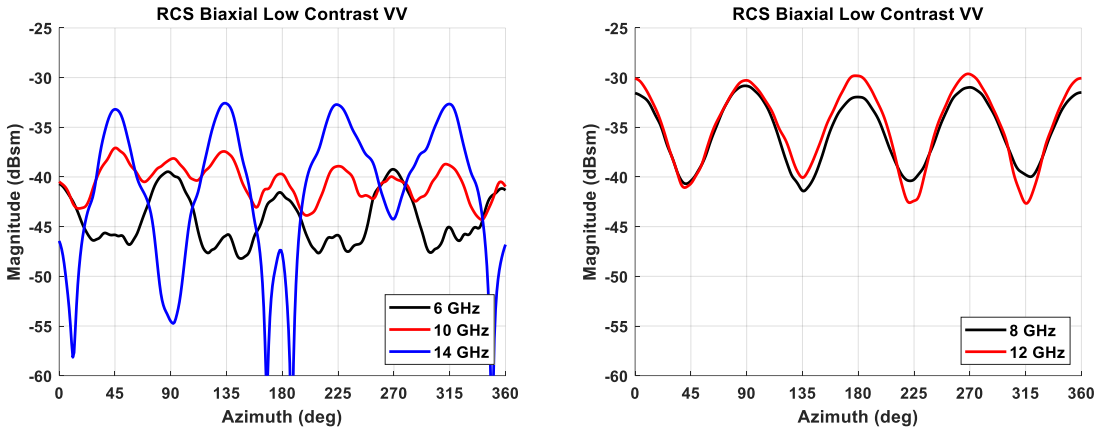

Figure 33. Fixed frequency azimuth-dependent slices from global measured RCS presentation of Knisely biaxial low contrast cube. 6, 10 and 14 GHz (left) and 8 and 12 GHz (right).

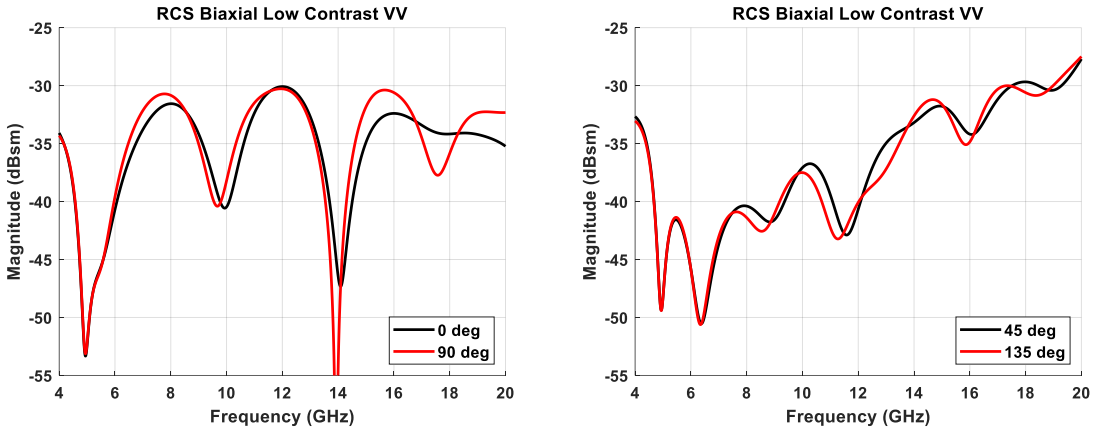

Figure 34. Fixed azimuth frequency-dependent slices from global measured RCS presentation of Knisely biaxial low contrast cube. 0 and 90 degrees (left) and 45 and 135 degrees (right).

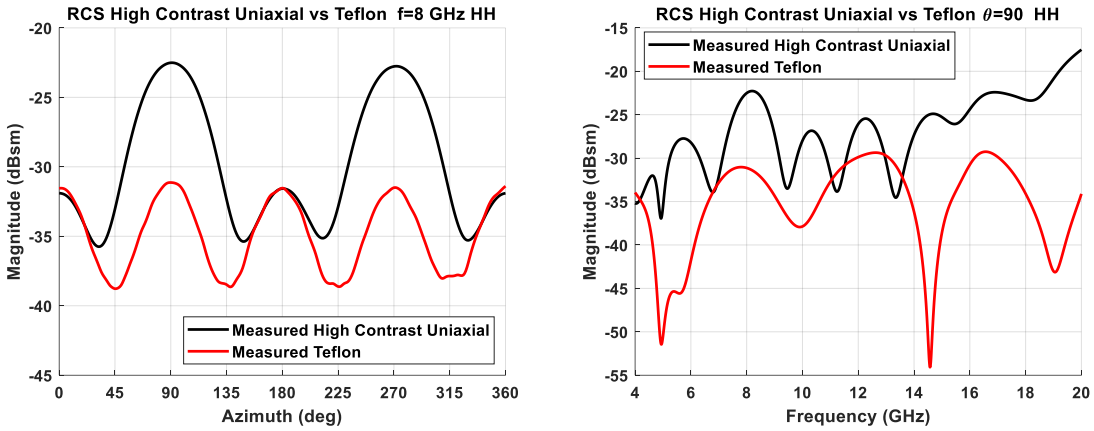

Figure 35. Measured RCS of high contrast uniaxial cube vs isotropic Teflon cube of same dimensions. Fixed frequency azimuth-dependent slice at 8 GHz (left) and fixed azimuth frequency-dependent slice at 90 degrees. Magnitude differences and similarities at specific angles (left) reflect excitation of primary tensor parameters for each material. Magnitude differences and frequency response contraction at 90 degrees azimuth (right) reflect excitation of primary tensor parameters for each material.

Legacy and Traceability with Prior Work.

The work of Knisely was selected as a launching point for this research for the following reasons:

- Existing 3D printed uniaxial and biaxial cubes designed for the TE_{10} mode dimension of the X-band waveguide (22.86 mm on a side) were readily available and their orthogonal three-axis geometry is well-suitable for biaxial estimation.
- The existing cubes are available in low contrast and high contrast geometries which is helpful for challenging inversion schemes.
- Quality waveguide measurements for the all chosen cubes provide legacy data and a means of validation for current results.

- Comparisons between waveguide samples (infinite in extent) and free space illumination (finite) provides opportunity for understanding limits of artificial dielectric designs.

Use of FEKO as a Forward Solver.

The Mie Series provided an efficient modal solution as a scattered field forward solver in the case of spheres. The illumination of cubes beyond the Rayleigh region but electrically small for physical optics requires the use of a full-wave solver. There are several government and commercial codes available to predict the scattered fields of dielectric targets. At the inception of this research, comparisons were made between CST Microwave Studio, SENTRi, (DoD-owned) and FEKO for use as a forward solver. While each one has advantages and limitations such as types of problems solved, memory usage, cost, availability, ease-of-use, etc., FEKO has the most intuitive operational design and the opportunity to examine differences between the use of surface equivalent currents (SEP) and volumetric currents (VEP) in solving for the scattered fields. For isotropic cubes, FEKO was directed to use an SEP approach which is far more efficient than VEP based on the number of mesh elements. In the case of anisotropy, FEKO does not support SEP and utilizes the finite element method (FEM). FEKO is also equipped with internal optimization capabilities, making external interfaces to codes such as MATLAB unnecessary.

Range Configuration and Calibration

Facility and equipment availability prevented the use of the same measurement configuration presented in Section 3.1 to be used for cube scattered field measurements.

Recognizing the polarization limitation of the previous configuration, a MVG QH2000 dual-polarized feed antenna was used to illuminate the cubes from 91.44 cm away. Using (1.2), the target maximum extent D_{max} is expressed as

$$D_{max} \ll \sqrt{\frac{\lambda_{min} R}{2}} \sim 214\ mm. \tag{3.19}$$

Using the maximum frequency of 12.4 GHz for Knisely validation at 91.44 cm provides a maximum target extent of $D_{max} \ll 105.1\ mm$. Since the maximum extent of the cubes of interest are 32.3 mm (22.86 mm cube at 45 degrees), a margin of 3.25x satisfies the far field criteria.

In the previous section on measured sphere scattering, a squat cylinder whose diameter was 190.5 mm was used as a calibration device to mitigate unwanted system response from perturbing the incident field. That same cylinder is too large for the new measurement configuration and was replaced by three canonical PEC shapes:

- Squat cylinder: Diameter = 22.1996 mm Height = 11.0744 mm.
- Cube at broadside: Side length = 22.86 mm.
- Sphere: Diameter = 15.875 mm.

As a means of demonstrating adequate illumination using the new feed antenna, shorter distance to target, and new calibration cylinder, the RCS of the cylinder (calibration reference = cube), cube (calibration reference = cylinder), and sphere (calibration reference = cube) are shown in Figure 36. Excellent agreement is shown between the calibrated measurements and the FEKO predicted responses for the cylinder and cube, especially within the X-band region. The sphere response has been perturbed by the presence of the

support structure, primarily at VV polarization, which is expected in view of the prior discussion on mutual coupling.

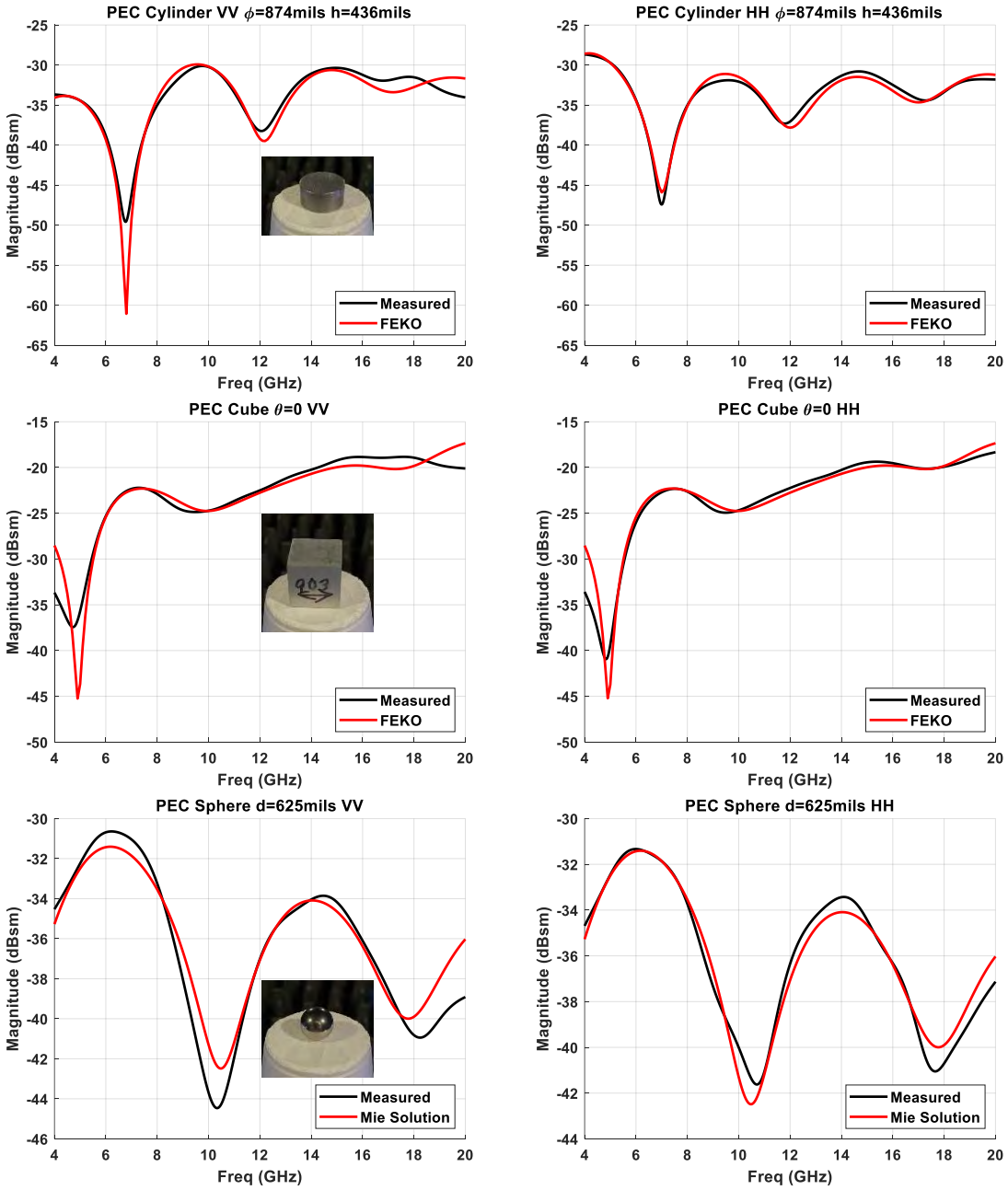

Figure 36. Comparison of measured RCS of canonical PEC targets to predicted RCS using FEKO: squat cylinder VV (upper left) and HH (upper right), squat cylinder VV (middle left) and HH (middle right), sphere VV (lower left) and HH (lower right).

Measurement and Inversion Methodology

The cubes will be measured and inverted in the following order of increasing complexity:

1. Teflon: Isotropic
2. Nylon with low loss filled occlusions: Uniaxial/Low contrast
3. Nylon with ESD-PETG filled occlusions: Uniaxial/High contrast
4. Nylon with air occlusion: Biaxial/Low Contrast

Prior to cube measurements, the scattered field from the cube and cylinder were each measured over the 4-20 GHz band along with background fields at both VV and HH (TE and TM) polarizations. All cubes were illuminated from 4-20 GHz with VV and HH (TE and TM) polarizations for each cube orientation. All cubes were rotated through a 360-degree aperture with a frequency sweep occurring every degree.

Since Teflon is isotropic, the cube was measured in one orientation with zero azimuth marked by the normal to one cube face parallel to the incident field direction of propagation. Each frequency sweep was calibrated according to (3.16) with FIR gating applied. The uniaxial and biaxial cubes were measured in three orthogonal orientations defined by Knisely as O-1, O-5, and O-4. Measurement and calibration were the same as for Teflon.

Inverting the cube measurements into permittivity will follow an iterative man-in-the-loop (IMIL) approach, combining known frequency and azimuth dependent behavior with the Nelder-Mead non-linear least squares optimization by which the measured and estimated RCS is compared and minimized in a least squares sense. To aid in determining initial permittivity estimates, known changes in frequency shift and magnitude bias for

perturbations in real and imaginary permittivity are computed and shown in Figure 37. Here the shift in global minimum in frequency and magnitude tracks for changes in complex permittivity. Given initial assumptions of real and imaginary tensor parameters combined with estimated changes in global minimum frequency and magnitude (Figure 37), a user may converge on a solution. Then, a narrowly scoped iterative search along the real and imaginary tensor axes for a least-squares minimum provides the optimal estimate for permittivity. The minimal least squares difference between the calibrated complex scattered field and the estimated complex scattered field is stated as

$$f_{obj} = min \sum_{k=1}^{N} |E_a^T - E_e^T(\epsilon_r)|_k \tag{3.20}$$

where E_a^T is the calibrated complex scattered field, $E_e^T(\epsilon_r)$ is the estimated complex scattered field from the trial permittivity, and k is the index corresponding to the frequency or azimuth angle of interest. In general, f_{obj} is not limited to frequency or azimuth dependence, but can be a mixture of estimates from frequency, azimuth, and polarization simultaneously.

Permittivity Estimation Summary

A method for estimating the permittivity of isotropic, uniaxial, and biaxial cubes has been presented. A rationale for anisotropic cube selection as a means of traceability with prior efforts along with the use of FEKO as a forward solver was provided. Distinctions between sphere and cube measurement configurations were detailed including selection of calibration reference shapes. Finally, measurement and inversion procedures were outlined for all four dielectric cubes being analyzed. The next chapter reveals the scattered field

measurements associated with each cube and the results of their respective inversion processes. Finally, a discussion of estimation uncertainty will be provided.

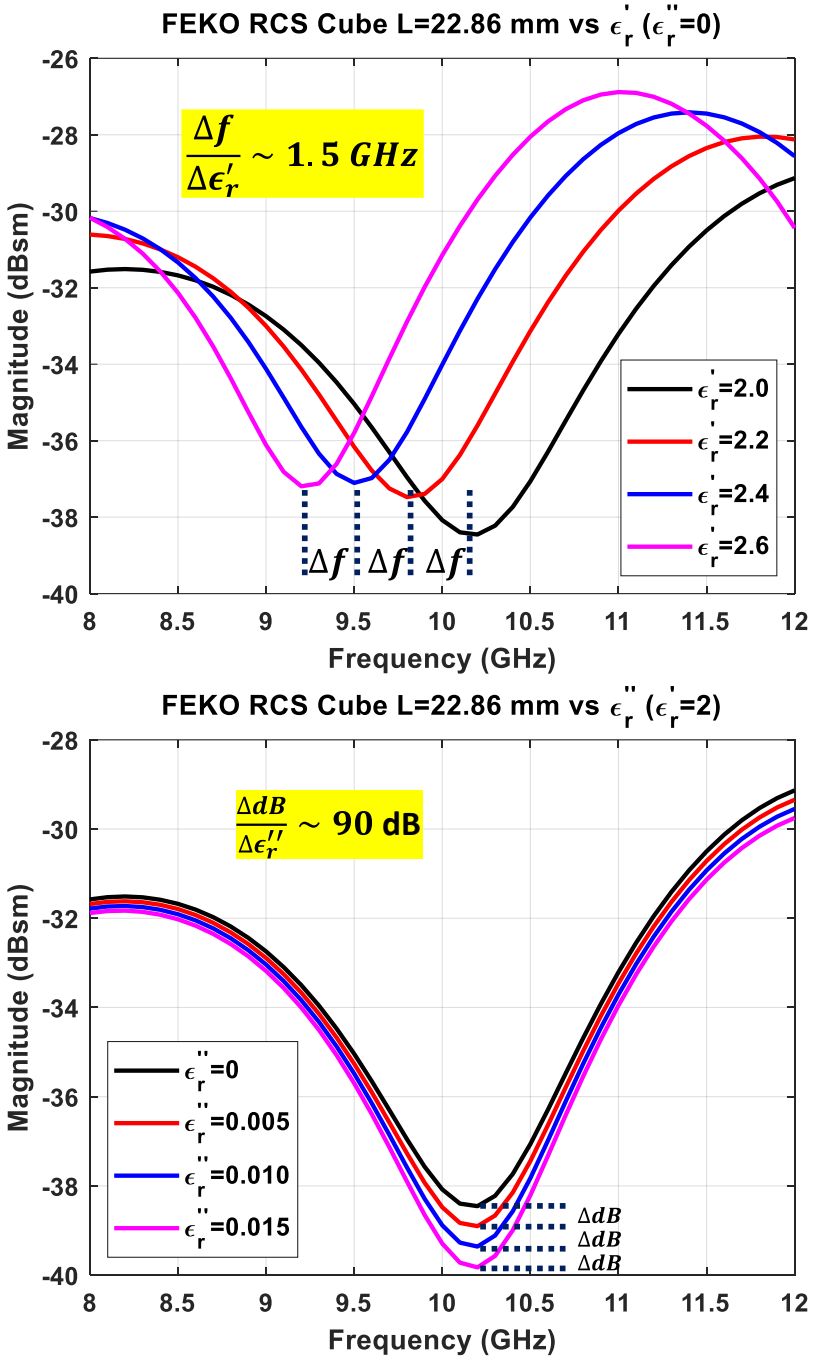

Figure 37. FEKO RCS of arbitrary dielectric cube (L=22.86 mm) demonstrating shifts in global minimum in frequency and magnitude for variances in real and imaginary permittivity.

IV. Results and Analysis

4.1 Measured Scattered Field Comparisons

Before presenting estimated permittivity results for each cube, a comparison is made between the cubes for frequency- and azimuth-dependent scattered fields. Consider the comparison between the measured Teflon, low contrast uniaxial, and low contrast biaxial scattered fields from 8-12 GHz for the in-plane (O-1 and O-5) and out-of-plane (O-4) axes shown in Figure 38.[15] The value of this presentation lies in the comparison of the null frequency and level with respect to the Teflon null whose isotropic permittivity is $\epsilon_r = 2.05 - j0.00041$. A similar comparison between the measured Teflon cube and high contrast uniaxial cube is shown in Figure 39. A qualitative analysis of the estimated permittivity of each tensor axis, in-plane (O-1 and O-5) and out-of-plane (O-4), is shown in Table 4 where the unknown permittivity is compared to Teflon (T) based on null frequency and null level. Such analyses inform initial estimates for permittivity inversion whose convergence history for each of the four measured cubes is shown in the Appendix.

[15] The in-plane orientation is defined as those tensor axes (occlusion axes) that are transverse to the direction of propagation, whereas the out-of-plane orientation is defined as the single tensor axis (occlusion axis) that is in the direction of propagation.

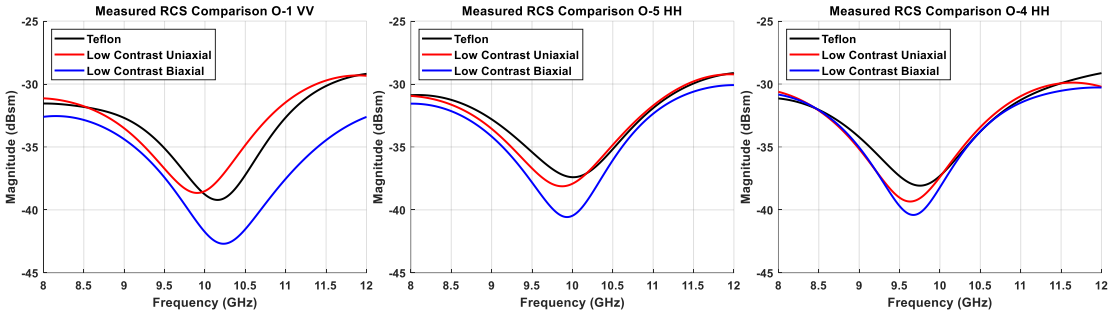

Figure 38. Measured frequency-dependent RCS comparison between Teflon, low contrast uniaxial, and low contrast biaxial cubes. The in-plane tensor axes O-1 and O-5 are shown left and middle respectively with out-of-plane axis O-4 shown right.

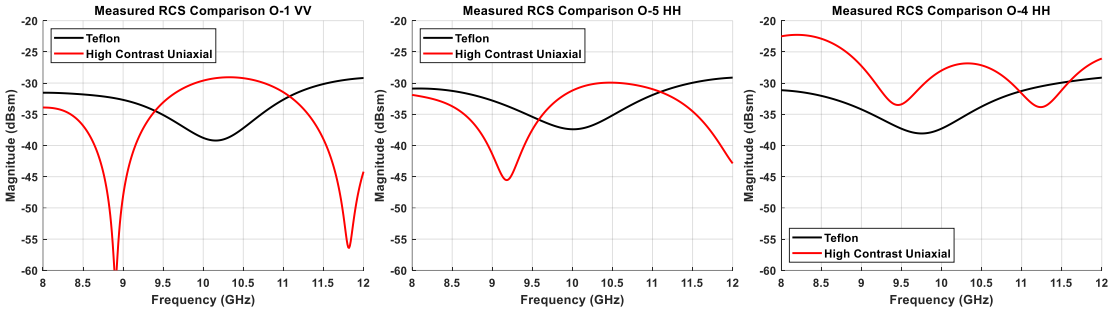

Figure 39. Measured frequency-dependent RCS comparison between Teflon and high contrast uniaxial cubes. The in-plane tensor axes O-1 and O-5 are shown left and middle respectively with out-of-plane axis O-4 shown right.

Table 4. Qualitative analysis of estimated permittivity for each tensor axis, in-plane (O-1 and O-5) and out-of-plane (O-4). Unknown permittivity is compared to Teflon (T) based on null frequency and null level.

	In-Plane O-1 (VV)		In-Plane O-5 (HH)		Out-of-Plane O-4 (HH)	
Cube Name	Null Freq	Null Level	Null Freq	Null Level	Null Freq	Null Level
Low Contrast Uniaxial	$\epsilon_r' > T$	$\epsilon_r'' \sim T$*	$\epsilon_r' > T$	$\epsilon_r'' > T$	$\epsilon_r' > T$	$\epsilon_r'' > T$
Low Contrast Biaxial	$\epsilon_r' < T$	$\epsilon_r'' \gg T$*	$\epsilon_r' > T$	$\epsilon_r'' \gg T$	$\epsilon_r' > T$	$\epsilon_r'' \gg T$
High Contrast Uniaxial	$\epsilon_r' > T$	$\epsilon_r'' \gg T$	$\epsilon_r' > T$	$\epsilon_r'' \gg T$	$\epsilon_r' \gg T$	$\epsilon_r'' \gg T$

* Teflon null level is excessively low compared to the other in-plane (O-5) and out-of-plane (O-4) axes. This may be due to mutual coupling with support structure.

The scattered field from each cube is measured as a function of frequency and azimuth. Having made frequency dependent comparisons of the scattered fields with respect to Teflon, a comparison is now made between the same scattered fields as a function of azimuth to identify potential ways to exploit such information for inversion purposes. A principal distinction between the frequency and azimuth-dependent measurements is the fixed cube orientation (O-1, O-5, and O-4) for frequency-dependence and variable orientation for the azimuth dependent measurements. Under the later, an HH-polarized incident field at zero azimuth begins with O-5 and transitions to O-4 at 90-degrees azimuth. A depiction of this orientation transition is shown in the first comparison where a 360-degree plot of RCS at 8 GHz for all cubes using both VV and HH polarizations is shown in Figure 40. Here there are noticeable differences between the RCS of the different cubes, but the same sinusoidal response due to the same shape and size of each cube. Under ideal conditions, an azimuth-dependent measurement of a cube may be limited to 90 degrees of illumination as it repeats every 90 degrees. However, a combination of cube manufacturing irregularities combined with target mounting and rotational errors make a full rotation an asset for quality checks. To examine the potential for azimuth dependent exploitation, the same arbitrary cube shown in Figure 37 is examined for known changes in RCS magnitude and scattered field phase bias resulting from perturbations in the real and imaginary permittivity as shown in Figure 41. Here, measurable shifts in magnitude and phase behavior are the result of changes in real and imaginary permittivity. As in the frequency-dependent case, such analyses inform initial estimates for permittivity inversion.

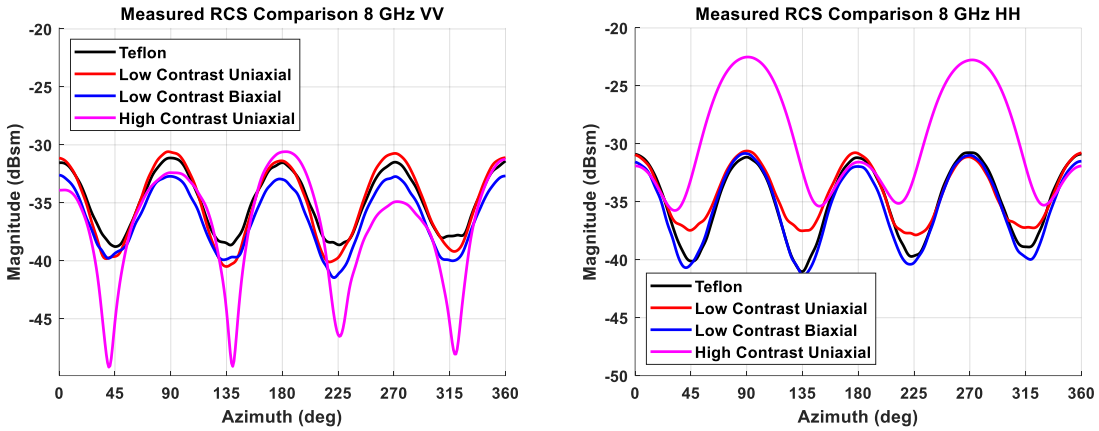

Figure 40. Measured azimuth dependent RCS comparison at 8 GHz using VV (left) and HH (right) polarization for Teflon, low contrast uniaxial, low contrast biaxial, and high contrast uniaxial cubes.

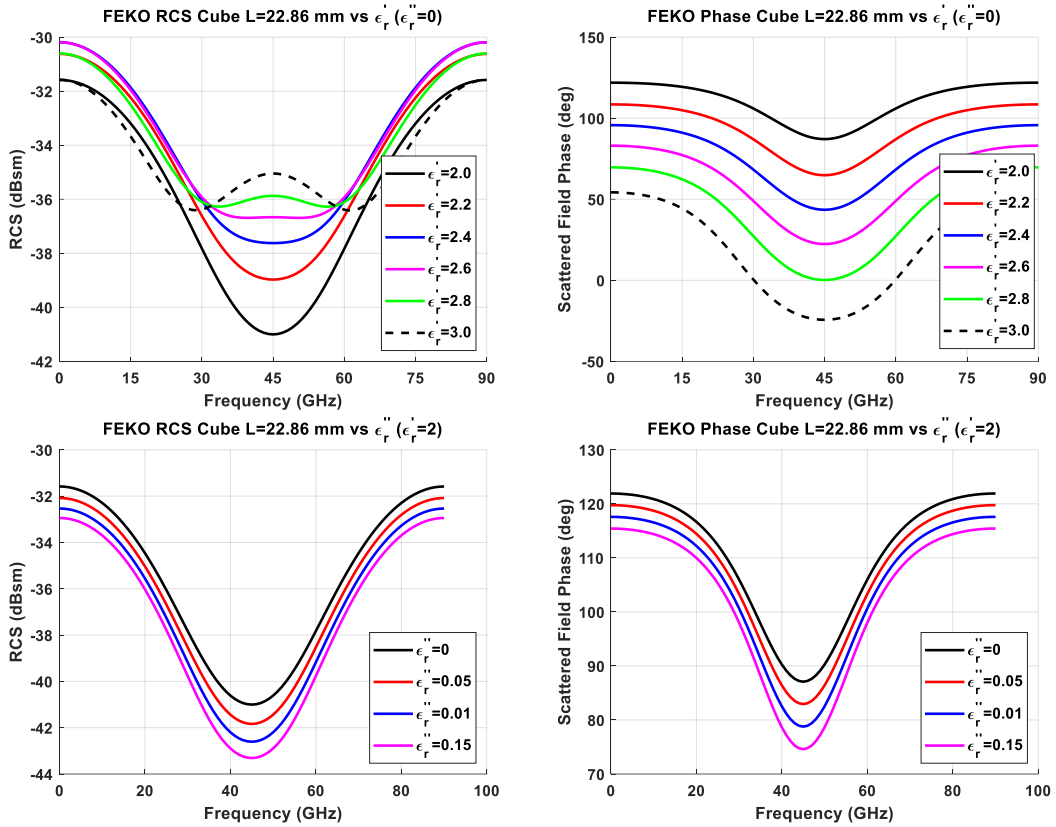

Figure 41. FEKO RCS and scattered field phase of arbitrary dielectric cube (L=22.86 mm) demonstrating shifts in global minimum magnitude and phase for variances in real and imaginary permittivity. RCS shifts (top left) and scattered field phase (top right) versus real permittivity and RCS shifts (bottom left) and scattered field phase (bottom right) versus imaginary permittivity

The Use of Measured Phase in Inversions

Complex measured scattered fields provide independent information to the inversion algorithm expressed in (3.18) in addition to magnitude-only data (RCS). An inversion was performed on the Teflon cube using measured RCS-only at 8 GHz across the full 360-degree rotation aperture. The inverted permittivity for VV polarization was $\epsilon_r = 1.955 - j0.00226$ and for HH polarization was $\epsilon_r = 2.036 - j0.00105$. Inverted RCS as a function of azimuth was reconstructed using the inverted permittivity for each polarization and is shown in Figure 43.

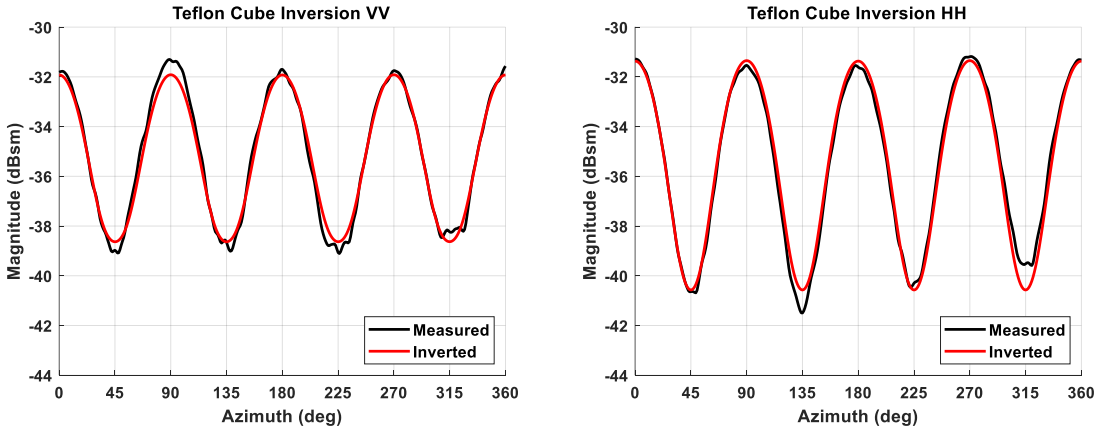

Figure 42. RCS of Teflon cube measured versus inverted at 8 GHz VV (left) and HH (right). Inversion used RCS only without phase.

Inverted phase as a function of azimuth was reconstructed using the inverted permittivity for each polarization and is shown in Figure 43.

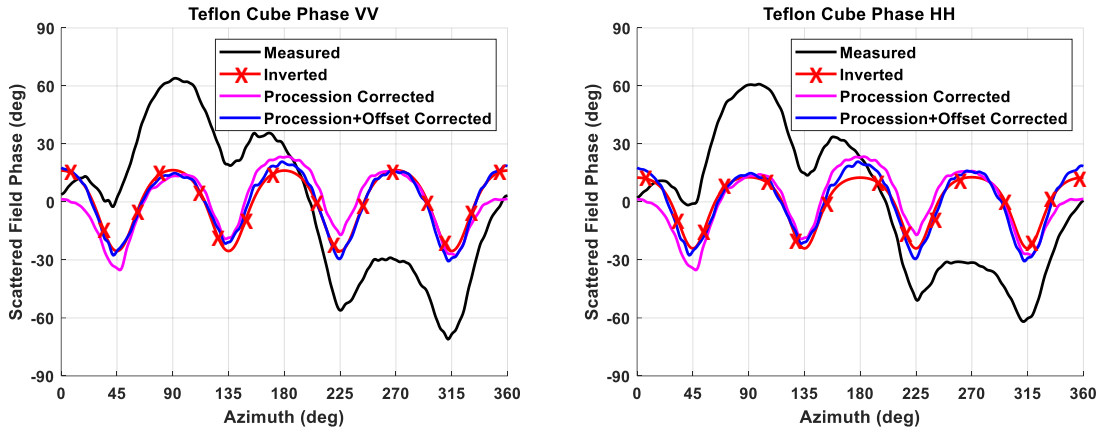

Figure 43. Measured scattered field phase compared to FEKO inverted phase for Teflon at 8 GHz using VV polarization (left) and HH polarization (right). Comparison reveals rotational procession and offset in the Styrofoam support superimposed on azimuth rotation. A two-step phase correction scheme mitigates most rotational errors.

The calibrated phase shown in the black curves has significant error as compared to the inverted azimuth-dependent RCS phase (red) and not valued added data for inversion. The difference between the measured and predicted phase is due to two errors: a procession in the Styrofoam support column as the rotator moves in azimuth and a lateral offset in the target, either directly from the target itself or the foam column not centered on the azimuth rotator. The procession is due to a column tilt caused by a variance in thickness created by a chemical reaction as the glue between the column and wooden base was cured. To estimate the full procession offset, consider the maximum phase error in Figure 43 from the measured phase to the inverted phase which is 47.28 degrees. At 8 GHz, this is equivalent to a maximum procession displacement of the target, P_{max},

$$P_{max} = \frac{47.28_{deg}}{360_{deg/\lambda}} \frac{299.7925_{mm/ns}}{8_{GHz}} \sim 4.922\, mm\,. \tag{4.1}$$

The phase of the measured scattered field, Φ, (3.7) is now corrected by

$$\Phi_P' = \Phi_P e^{j\beta_0 P_{max} sin\theta}, \tag{4.2}$$

where Φ_P' is the procession corrected phase and θ is the azimuth angle of incidence. A second correction remains due to an offset from the center of rotation. The remaining phase error due to this displacement, D_{max}, is

$$D_{max} = \frac{23.06\ _{deg}}{360_{deg/\lambda}} \frac{299.7925_{mm/ns}}{8_{GHz}} \sim 2.400\ mm. \tag{4.3}$$

The displacement corrected phase of the measured scattered field, Φ_P'', (4.2) is now corrected by

$$\Phi_P'' = \Phi_P' e^{j\beta_0 D_{max} sin(\theta/2)}, \tag{4.4}$$

where Φ_P' is the procession corrected phase and θ is the azimuth angle of incidence. The final corrected phase is shown in the blue curves of Figure 43. While the procession error is the same for all cubes, the displacement error is local to each cube based on the accuracy of placement on the support. Now that a phase corrected scheme has been shown, the inverted permittivity of the Teflon based on the full complex scattered field is shown in Figure 44. The inverted RCS based on the addition of phase information into the inversion process made no distinguishable difference in the quality of the inversion as seen in Figure 44. A summary of the differences in the inversions with and without the use of phase is shown in Table 5.

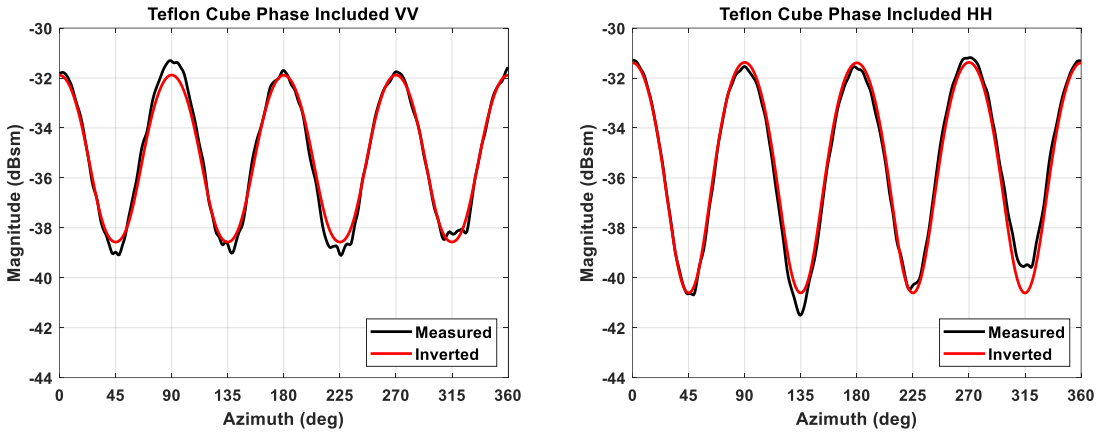

Figure 44. RCS of Teflon cube measured versus inverted at 8 GHz VV (left) and HH (right). Inversion used RCS and phase data.

Table 5. Comparison of inverted Teflon permittivity at 8 GHz using RCS alone versus the addition of phase information at both VV and HH polarizations.

Inversion Basis	Permittivity (real)		Permittivity (imaginary)	
	VV	HH	VV	HH
RCS Only	1.955	2.036	0.00442	0.00214
RCS with Phase	1.957	2.038	0.00440	0.00278
NIST Permittivity	2.05	2.05	0.00041	0.00041

Isotropic Teflon Permittivity Estimate

The Teflon cube is isotropic and non-dispersive such that both azimuth-dependent and frequency-dependent inversions are possible. An inversion of the Teflon cube measured azimuth-dependent RCS was performed at 8, 9, 10, 11, and 12 GHz for VV and HH polarizations, the results of which are shown in Figure 45. The permittivity estimates in the plot (shown by "x") are superimposed with the value published by NIST (blue-dash curve). The real values show close agreement with NIST while the imaginary values diverge form

NIST by an order of magnitude. This substantial error in imaginary inversion is consistent with the results of the sphere inversions shown in Chapter 3 for low loss dielectric spheres.

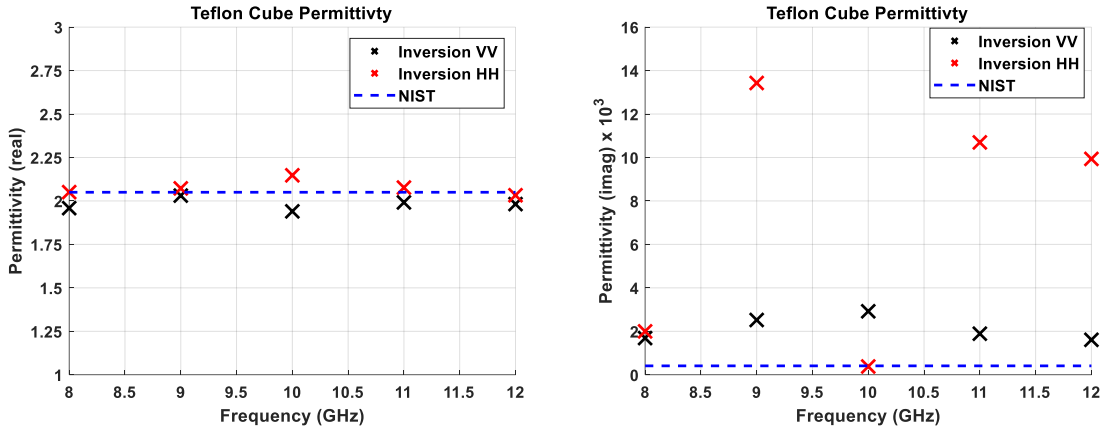

Figure 45. Estimated Teflon permittivity real (left) and imaginary (right) for VV and HH polarizations using azimuth-dependent measured RCS.

Uniaxial Low Contrast Permittivity Estimate.

The stated goal of this research was to compare the inversions from the current research with those of Knisely measured in waveguide. Three anisotropic cubes available for study in this regard are a low contrast uniaxial, high contrast uniaxial, and low contrast biaxial cube. Direct comparisons are available for the high contrast uniaxial and low contrast biaxial cubes. The low contrast comparison is a qualitative comparison as the Knisely Cube occlusions are air-filled while the filler for the current research was a Nylon-based material.

The uniaxial low contrast cube is comprised of an array of 49 (7x7) occlusions measuring 1.5875 mm x 1.5875 mm x 22.86 mm as shown by Knisely in Figure 46. Each occlusion is filled with a Nylon-based material. As an artificial dielectric, the three anisotropic cubes used in this research (uniaxial and biaxial) can be described by two permittivity tensors as shown in Figure 47. This presents a problem in that there is no common third axis, thus requiring a rotation of the cube orientation 90 degrees in elevation

to appropriately excite the three axes in one tensor. However, to demonstrate the technique of anisotropic inversion and minimize measurement error induced by physically repositioning the cubes, orientations O-1, O-5, and O-4 will be estimated according to the nomenclature of Knisely (Figure 5). While this minimizes error, it also assumes that the permittivity of interest is constant over the measured band. In the work of Knisely, the permittivity of each cube was nearly constant across X-band and thus provides a validation metric for this research. The azimuth-dependent inversion used for Teflon was applicable because an isotropic homogenous material can be thought of as a three-dimensional array of spatially distributed scatterers (e.g. spheres) on a single rectangular coordinate system. This is not the case for the extruded occlusions of the current cubes. The use of a dual-polarized feed antenna permits the collection of VV and HH polarizations by a 90-degree azimuth rotation. This movement has significantly less error than repositioning the cube on the support structure. Thus, the order of measurement each of the three anisotropic cubes is O-1 (VV) and O-5 (HH) at zero degrees azimuth, and at 90 degrees azimuth (HH) to excite the third tensor axis using orientation O-4.

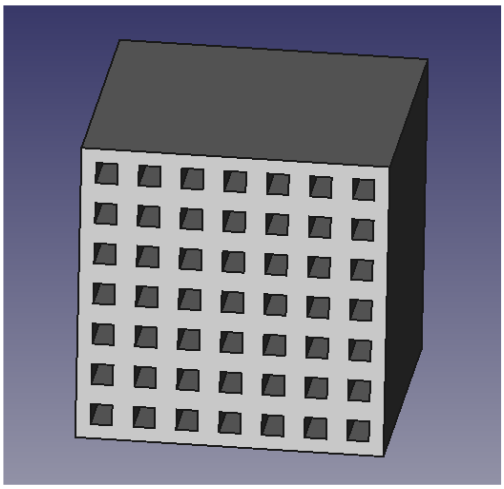

Figure 46. Configuration of uniaxial occlusions [8].

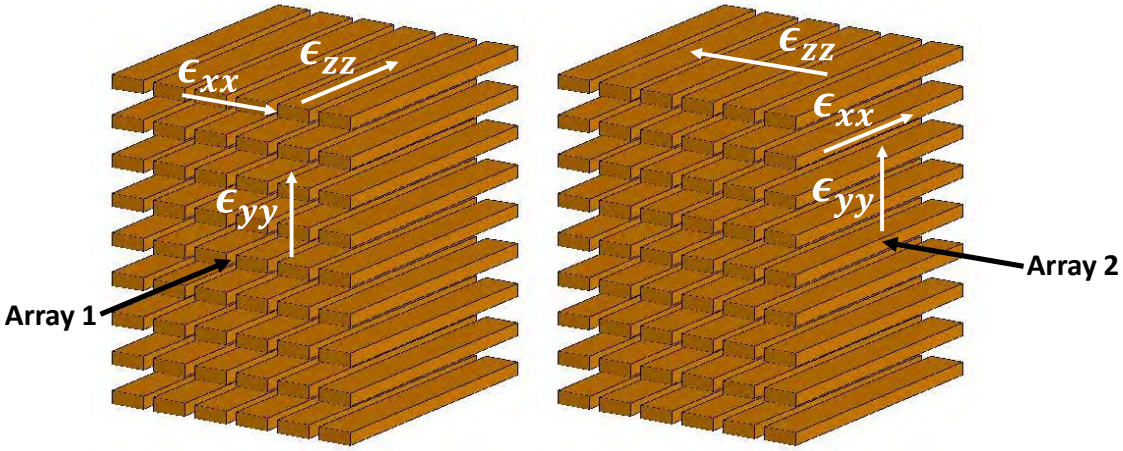

Figure 47. Diagram of permittivity tensors for each anisotropic cube. Knisely orientations O-1, O-3, and O-5 (left) and O-2, O-4, and O-6 (right). The base molecule shown is an extruded rectangle representing a biaxial configuration whereas the uniaxial molecule is an extruded square.

The RCS of the low contrast uniaxial cube was measured at the requisite zero- and 90-degree incident angles. Three frequencies and their corresponding RCS levels were selected as input to the least squares optimization for each measurement to estimate permittivity. The inverted RCS is overlaid with the measured RCS for comparisons as shown in Figure 48. The inverted RCS values are within 1 dB for all cases.

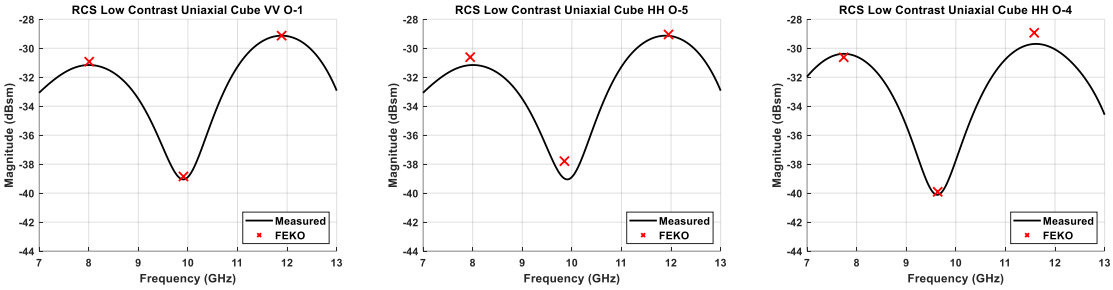

Figure 48. Comparison between measured and inverted RCS of low contrast uniaxial cube: O-1 (left), O-5 (middle), and O-4 (right).

The inverted permittivity (real) is plotted over the original Knisely data for this same cube in Figure 49. This figure, extracted from [8] and courtesy of Alexander Knisely, shows the original dielectric constant for each tensor axis compared to the current research. The Knisely cube in this instance was air-filled which would naturally result in a lower permittivity than the current Nylon-filled cube which is reflected in the data of Figure 49. A frequency of 10 GHz was selected as a representative frequency over which the permittivity was estimated.

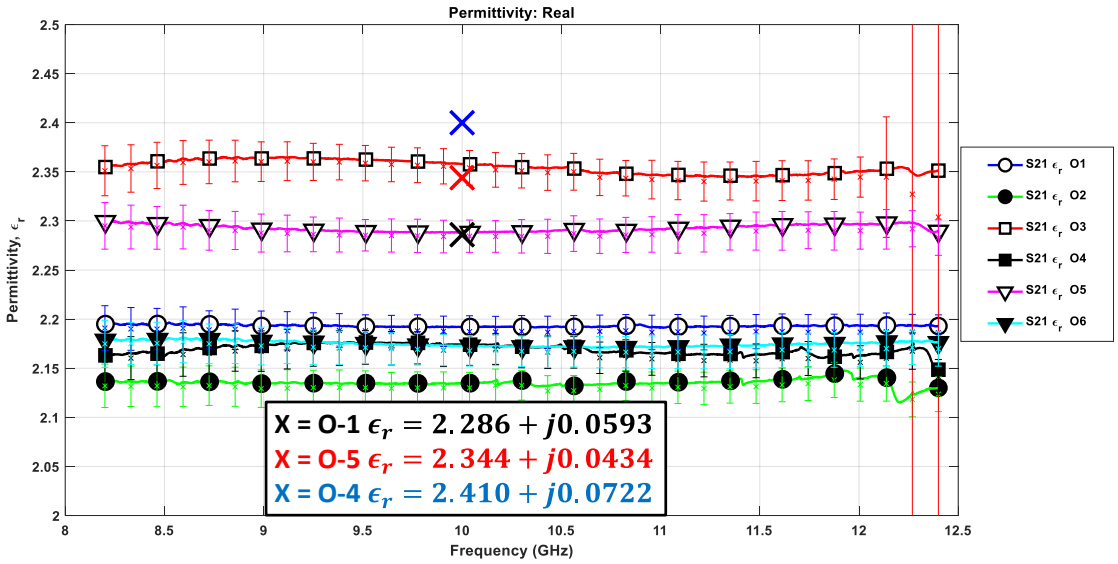

Figure 49. Low contrast uniaxial (occlusion-filled) inverted permittivity (real) overlaid with Knisely (occlusion air-filled) square waveguide results [8]. A frequency of 10 GHz was selected as a representative frequency over which the permittivity was estimated. Original plot courtesy of Alexander Knisely. Y-axis has been expanded for presentation purposes.

Uniaxial High Contrast Permittivity Estimate.

The uniaxial high contrast cube has the same construction as the uniaxial low contrast cube (Nylon), except that the occlusions are filled with ESD-PETG material. The RCS of the high contrast biaxial cube was measured at the requisite zero- and ninety-degree incident angles. Three frequencies and their corresponding RCS values were selected as input to the least squares optimization for each measurement to estimate permittivity. The inverted RCS is overlaid with the measured RCS for comparison in Figure 50. The inverted RCS values demonstrate the efficacy of the method providing quality RCS reconstructions for all but two points: a deep null in the O-1 orientation which may be due to the influence of the dielectric support at that frequency since the RCS level is exceeding low; and the second is a ~2 dB error in the O-4 high contrast orientation of the third point. This may be

due to coupling between the high permittivity axis and the other two axes. The inverted permittivity (real) is plotted over the original Knisely data for this same cube in Figure 51. This figure, extracted from [8] and courtesy of Alexander Knisely, shows the original dielectric constant for each tensor axis compared to the current research. The current inversion shows a higher out-of-plane permittivity as Knisely and a lower than expected in-plane permittivity.

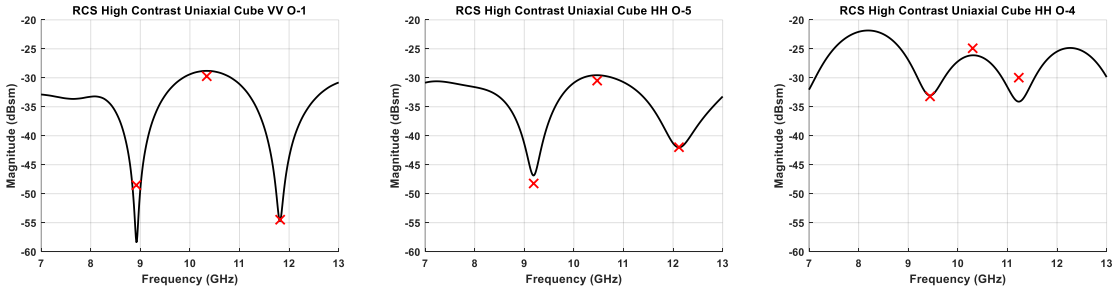

Figure 50. Comparison between measured and inverted RCS of high contrast uniaxial cube: O-1 (left), O-5 (middle), and O-4 (right).

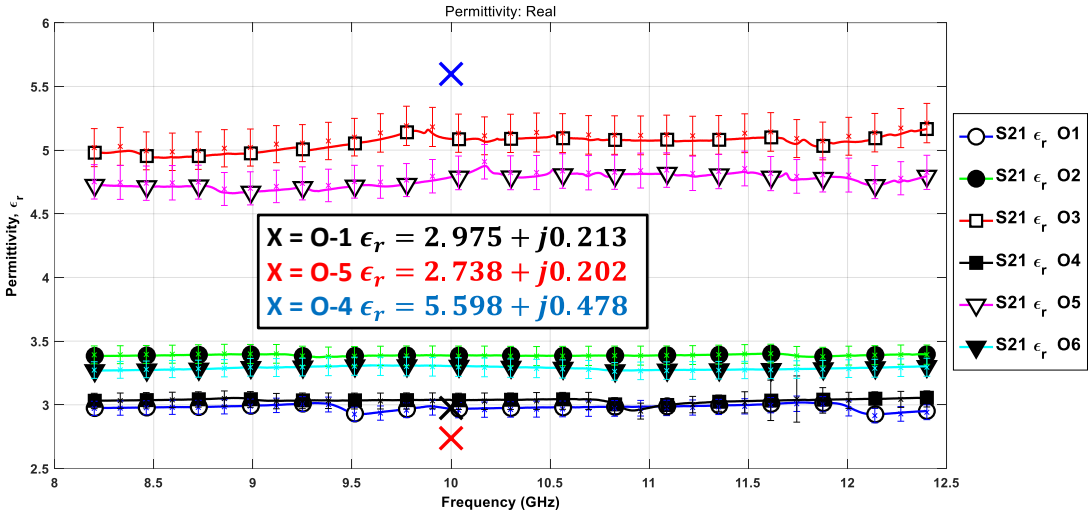

Figure 51. High contrast uniaxial inverted permittivity (real) overlaid with Knisely square waveguide results [8]. A frequency of 10 GHz was selected as a representative frequency over which the permittivity was estimated. Original plot courtesy of Alexander Knisely. There is a known discrepancy between the original plot legend (right) and published Knisely orientation definitions.

Biaxial Low Contrast Permittivity Estimate

The biaxial low contrast cube has a 9 x 6 array of air-filled occlusions measuring 1 mm x 2.79 mm x 22.86 mm. The RCS of this cube was predicted in FEKO in the O-1, O5, and O4 orientations and compared to the measured RCS. The three-dimensional FEKO model including air-filled occlusions is shown in Figure 52. The RCS of this cube was measured at the requisite zero- and ninety-degree incident angles. Three frequencies and their corresponding measured RCS values were selected as input to the least squares optimization for each measurement to estimate permittivity. The inverted RCS is overlaid with the measured RCS and predicted FEKO response for comparison in Figure 53. The measured and inverted permittivity at each orientation reveal a variance with the stipulated permittivity (real) used for prediction. In each case, the shift in measured and inverted permittivity (real) with respect to the predicted RCS reveals a smaller effective dielectric constant than what was assumed $\epsilon_r \approx 2.8655 - 0.04j$ [3]. A comparison between Knisely and the current research for inverted real and imaginary permittivity is shown in Table 6.

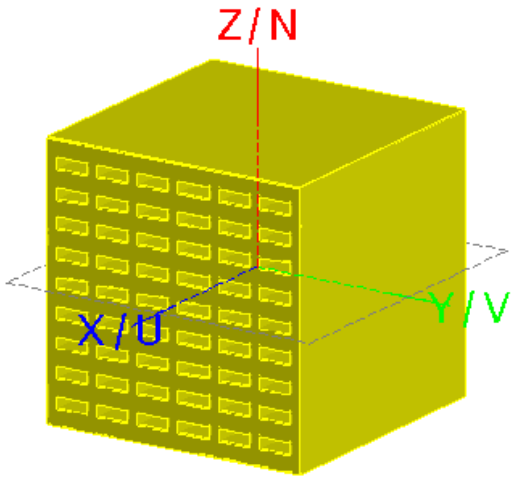

Figure 52. Three-dimensional FEKO model including air-filled occlusions used to compute RCS in the O-1, O-5, and O-4 orientations.

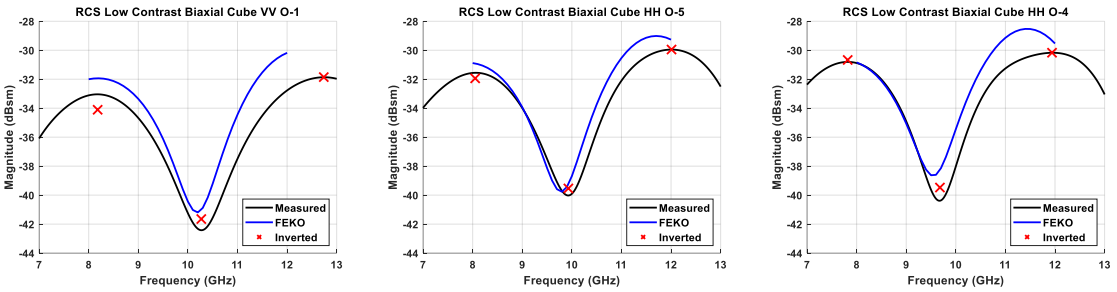

Figure 53. Comparison between measured, predicted, and inverted RCS of low contrast biaxial cube: O-1 (left), O-5 (middle), and O-4 (right).

Table 6. Estimated permittivity comparison between Knisely low contrast biaxial cube and current research inversion for all three measured orientations O-1, O-5, and O-4.

Sample Orientation	Permittivity (real)			Permittivity (imaginary)		
	Current	Knisely	Δ%	Current	Knisely	Δ%
In-Plane (O-1)	1.765	1.989	11.3	0.067	0.037	81.1
In-Plane (O-5)	2.012	2.209	8.9	0.046	0.053	13.2
Out-of-Plane (O-4)	2.435	2.274	7.1	0.079	0.055	43.6

4.2 Summary of Results

The proposed method for estimating permittivity was applied to all four cubes identified in Chapter I and shown in Figure 4. Comparisons were made between the measured and inverted RCS for the in-plane and out-of-plane axes along with differences between the estimated permittivity and that published by Knisely.

In the case of the Teflon cube, the permittivity was estimated from azimuth-dependent RCS data at 9, 10, 11, and 12 GHz. The estimates for the real component varied from the published NIST values by 4.6% and 0.68% respectively for the VV and HH polarizations. The estimated imaginary permittivity varied by an order of magnitude from the published NIST values for both polarizations.

The low contrast uniaxial cube was filled with a Nylon material in contrast with the Knisely cube whose occlusions were air-filled. As such, a direct comparison was not possible. However, a qualitative comparison shows reasonable shifts in the complex permittivity based on the inclusion of the Nylon filler and known shifts as previously defined. The inverted RCS based on the estimated permittivity is within 1 dB for all points chosen. The high contrast uniaxial cube displayed excellent agreement with Knisley for real permittivity with an estimated difference at 10 GHz of 0.1% for in-plane orientation O-1, 10.2% for in-plane orientation O-5, and between 9.8%-16.7% for the out-of-plane orientation.

Finally, the low contrast biaxial cube showed variances from Knisely for real permittivity from 8.9%-11.3% for the in-plane axes and 7.1% for the out-of-plane axis. The imaginary permittivity demonstrated high variances from Knisely showing 13.2%-81.1% for the in-plane axes and 43.6% for the out-of-plane axis. Additionally, the predicted RCS of this cube was made with FEKO and overlaid with the measured RCS and compared with the inverted RCS values. The variances between the predicted and measured RCS for the low contrast biaxial cube consistently showed a shift in frequency content and magnitude consistent with a lower dielectric constant for the measured RCS. This can be associated with a variance between the actual dielectric constant, the permittivity used by FEKO to compute the cube RCS at X-band. The other principal source of error impacting permittivity estimation is the cube of interest in contact with the polystyrene target support previously described. The impact of this error will be described in more depth in the next section along with other uncertainty components.

4.3 Uncertainty Considerations

The free space inversion method presented in this research is subject to a variety of errors that include incident field perturbations, target-mount mutual coupling, dynamic range limitations in subtraction, calibration errors, noise, dimensional errors either in estimation or manufacturing tolerances, alignment of samples with the incident field, and receiver anomalies. These error sources, while certainly numerous, do not have the same impact on scattered field measurements and subsequent inversions. Only target-mount mutual coupling, calibration bias, and sample alignment errors produce enough errors in measurement to be considered for an RMS estimate. The small dimension of the cubes alleviates concerns about incident field perturbations. Dynamic range limits and thermal noise contributions have been mitigated using vector background subtraction and software gating. Dimensional estimation using a micrometer is accurate to fractions of a millimeter and are not relevant. Manufacturing tolerances of the cubes impact assumptions about their scattering behavior and not measurement accuracy. This research utilizes a method that relies on the magnitude of RCS as a function of azimuth and frequency. As such, errors that impact measured RCS will be considered. A Root Mean Square (RMS) uncertainty estimate will combine the impact of calibration magnitude bias, sample alignment in azimuth, elevation, and roll (includes polarization misalignment), and mutual coupling. Calibration phase is not considered in the inversion process and therefore not incorporated into the error estimate. In addition to the RMS error estimate, the Teflon cube will act as a representative in examining target-mount mutual coupling, both as a function of frequency and azimuth.

Target-Mount Coupling Errors

Mutual coupling between spheres and their mounting structure was reported in Chapter III. It was assumed that such coupling errors would also be present when using cubes. A representative view of mutual coupling between Teflon and its Polystyrene mount is shown in Figure 54 - Figure 57 respectively. In Figure 54, the vector subtraction is applied between the complex signature of the Teflon cube mounted on the Polystyrene disk and the disk itself. This subtraction removed any direct scattering from the disk while leaving any mutual coupling behind. Figure 54 reveals approximately 0.8 dB or error due to mutual coupling using HH polarization. In Figure 55, the same operations were performed using VV polarization and there is negligible coupling remaining. These two representative examples of mutual coupling are based on frequency-dependent scattering data. The same subtraction operation was applied to the cube-on-foam scenario in Figure 56 (HH) and Figure 57 (VV). In Figure 56, a bias of about 0.8-1.0 dB is shown across the entire rotating aperture. However, in Figure 57 there is negligible impact from the presence of the Polystyrene disk.

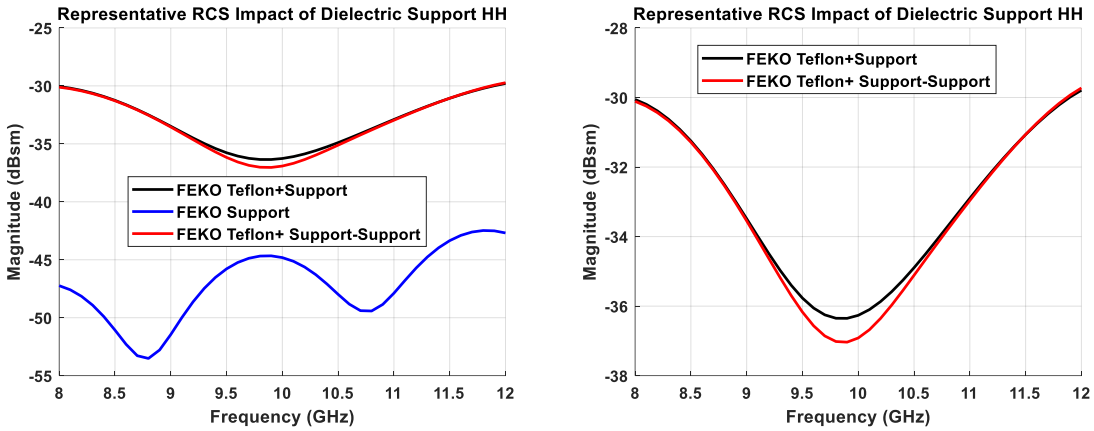

Figure 54. Representative RCS impact of Teflon cube mounted on Polystyrene support disk as a function of frequency using HH polarization. RCS of Teflon cube on disk, disk alone, and complex subtraction (left). Expanded view of teflon cube mounted on cube and subtracted RCS (right).

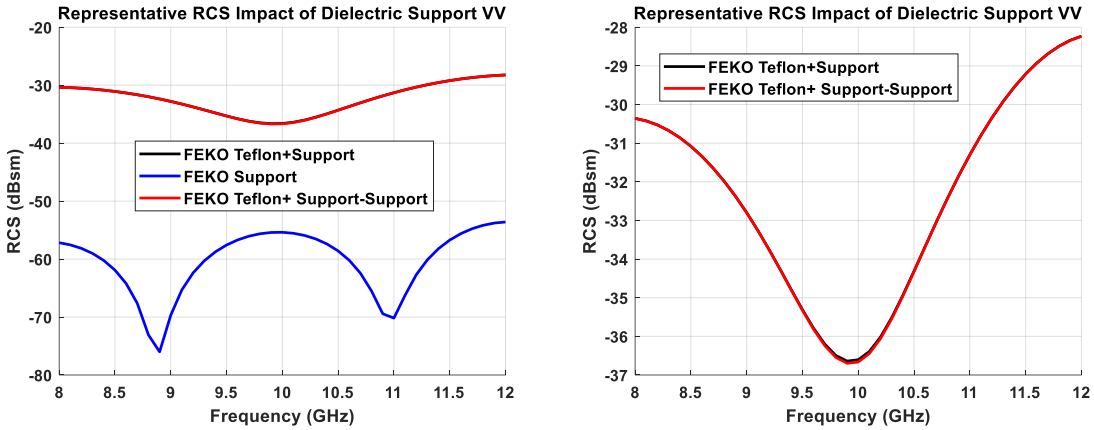

Figure 55. Representative RCS impact of Teflon cube mounted on Polystyrene support disk as a function of frequency using VV polarization. RCS of Teflon cube on disk, disk alone, and complex subtraction (left). Expanded view of teflon cube mounted on cube and subtracted RCS (right).

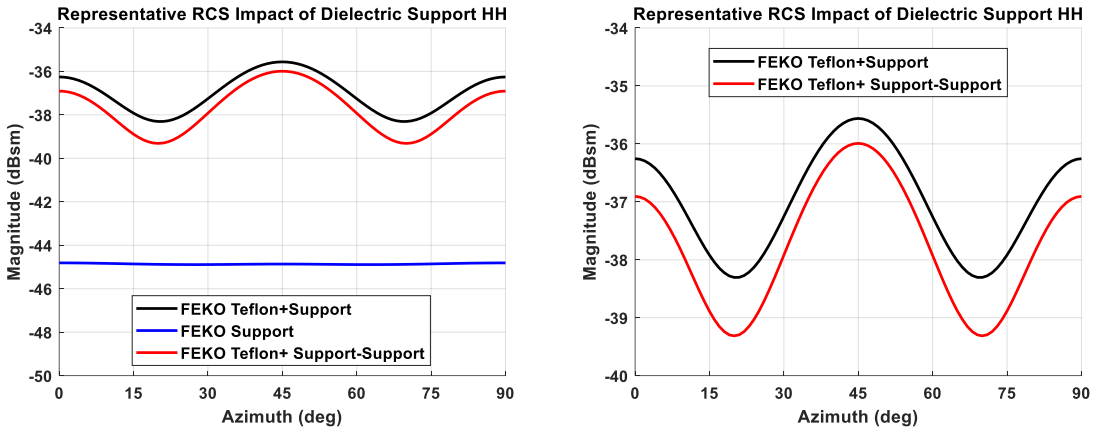

Figure 56. Representative RCS impact of Teflon cube mounted on Polystyrene support disk as a function of azimuth at 10 GHz using HH polarization. RCS of Teflon cube on disk, disk alone, and complex subtraction (left). Expanded view of teflon cube mounted on cube and subtracted RCS (right).

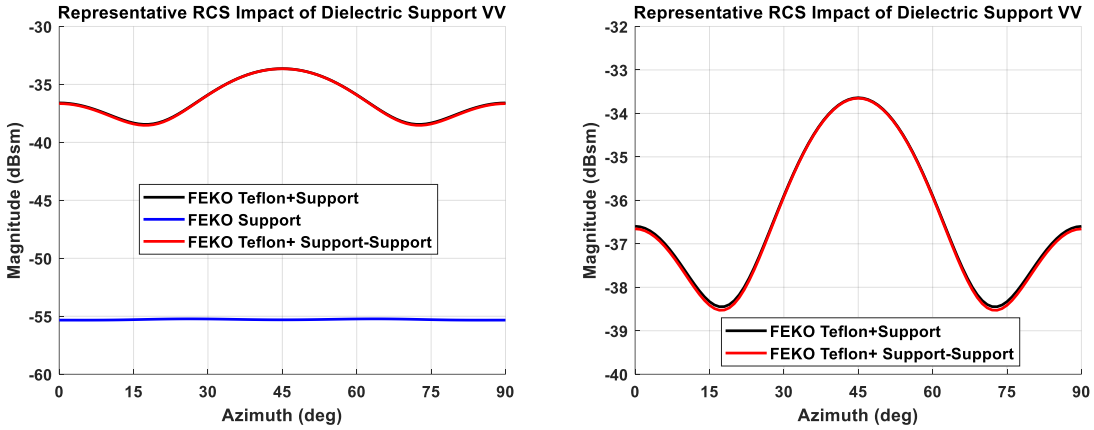

Figure 57. Representative RCS impact of Teflon cube mounted on Polystyrene support disk as a function of azimuth at 10 GHz using VV polarization. RCS of Teflon cube on disk, disk alone, and complex subtraction (left). Expanded view of Teflon cube mounted on cube

Root Mean Square Error Estimate

The largest uncertainty associated with calibration error is the leveling of the reference target and target under test (accounted by roll and elevation error). When the reference target is not level, the scattered field is less than it should be and forces the calibrated RCS to be higher than it should be. In practice, such errors are limited to ± 0.5 dB. In the same

way, when the target suffers alignment errors, the calibrated RCS is pushed lower than it should be. Azimuth, elevation, and roll alignment errors are estimated to be ± 0.2 degrees. The predicted value of the reference target has been mitigated through proper dimension estimation and sufficient computational meshing in FEKO. The RMS estimate in permittivity estimation is stated for real and imaginary components separately as

$$\delta\epsilon_r^{real} = \sqrt{\begin{array}{c}\left(\left|\frac{\partial\epsilon_r^{real}}{\partial|\theta|}\delta|\theta|\right|\right)^2 + \left(\left|\frac{\partial\epsilon_r^{real}}{\partial|\phi|}\delta|\phi|\right|\right)^2 + \left(\left|\frac{\partial\epsilon_r^{real}}{\partial|\alpha|}\delta|\alpha|\right|\right)^2 + \cdots \\ \left(\left|\frac{\partial\epsilon_r^{real}}{\partial|\gamma|}\delta|\gamma|\right|\right)^2 + \left(\left|\frac{\partial\epsilon_r^{real}}{\partial|C|}\delta|C|\right|\right)^2\end{array}} \tag{4.4}$$

and

$$\delta\epsilon_r^{imag} = \sqrt{\begin{array}{c}\left(\left|\frac{\partial\epsilon_r^{imag}}{\partial|\theta|}\delta|\theta|\right|\right)^2 + \left(\left|\frac{\partial\epsilon_r^{imag}}{\partial|\phi|}\delta|\phi|\right|\right)^2 + \left(\left|\frac{\partial\epsilon_r^{imag}}{\partial|\alpha|}\delta|\alpha|\right|\right)^2 + \\ \left(\left|\frac{\partial\epsilon_r^{imag}}{\partial|\gamma|}\delta|\gamma|\right|\right)^2 + \left(\left|\frac{\partial\epsilon_r^{imag}}{\partial|C|}\delta|C|\right|\right)^2\end{array}} \tag{4.5}$$

where $\delta\epsilon_r^{real}$is RMS error estimate for permittivity (real), $\delta\epsilon_r^{imag}$is RMS error estimate for permittivity (imaginary), θ is azimuth error, ϕ is elevation error, α is roll error, γ is calibration magnitude bias, and C is the error due to mutual coupling between the cube and mount. The error in azimuth, elevation, and roll are equally ±0.2 degrees, calibration bias is +0.5 dB, and the coupling error is -1.0 dB.

The Nyquist sampling interval for a 22.86 mm cube at 12 GHz is 28.6 degrees according to

$$\Delta\theta = tan^{-1}\left(\frac{\lambda}{2D}\right), \tag{4.6}$$

where λ is the operating wavelength and D is the maximum dimension of the target under illumination. Since the estimated error in alignment is 0.2 degrees, a small fraction of the Nyquist sampling criteria, any minor alignment error in azimuth, roll and elevation will produce negligible changes in RCS as shown in Figure 58. Here, the Teflon baseline at broadside was compared to the RCS at 8, 10, and 12 GHz.

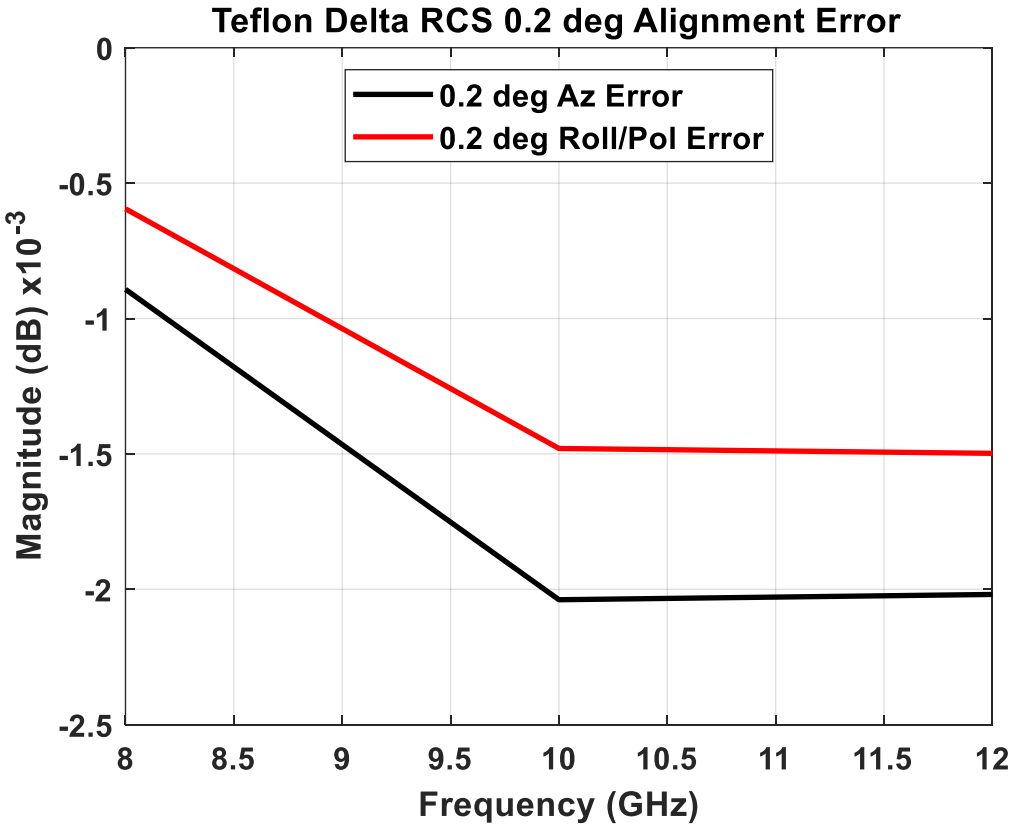

Figure 58. Change in RCS for baseline Teflon RCS versus 0.2-degree alignment error. Note: Y-Axis is in thousandths of one dB.

Such small changes in RCS warrant a modified version of (4.4) and (4.5) as

$$\delta\epsilon_r^{real} = \sqrt{\left(\left|\frac{\partial\epsilon_r^{real}}{\partial|\gamma|}\delta|\gamma|\right|\right)^2 + \left(\left|\frac{\partial\epsilon_r^{real}}{\partial|C|}\delta|C|\right|\right)^2} \tag{4.7}$$

and

$$\delta\epsilon_r^{imag} = \sqrt{\left(\left|\frac{\partial\epsilon_r^{imag}}{\partial|\gamma|}\delta|\gamma|\right|\right)^2 + \left(\left|\frac{\partial\epsilon_r^{imag}}{\partial|C|}\delta|C|\right|\right)^2}\,. \tag{4.8}$$

The RMS error is now driven by the calibration bias and mutual coupling with the target support. The impact of these errors on RMS permittivity uncertainty is summarized in Table 7. The pattern revealed in the earlier presentation of sphere permittivity inversions is that uncertainty is reduced with increasing loss as is shown in the objective function images of Figure 22. The fundamental question is whether uncertainty bounds provide decision making capability to discern anisotropy in measured orthogonal axes. To address this question, the inverted real and imaginary permittivity for each cube is overlaid with their individual axis uncertainty in Figure 59 through Figure 62. In the case of the Teflon cube (Figure 59), the real and imaginary axes have overlapping uncertainty which is to be expected as an isotropic sample. It is clear from the low contrast biaxial cube (Figure 60) and the low contrast uniaxial cube (Figure 61) that their overlapping uncertainties prevent any definitive identification of these two cubes as anisotropic. As in the case of Teflon, the in-plane uncertainty for the two uniaxial cubes is expected as their permittivity is designed to be the same. However, the difference in uncertainty between the low and high contrast cubes can be erroneously associated with their low contrast condition. This conclusion is set aside by the uncertainty of the high contrast uniaxial cube (Figure 62) which clearly

shows non-overlapping uncertainty between the in-plane and out-of-plane axes, not because of differences in permittivity (contrast) but instead is the direct result of a high loss tangent. This result is consistent with the objective function for the sphere inversions shown earlier in Figure 22. The high loss of the high contrast sample greatly reduces uncertainty and provide a clear context where this method may be most useful.

Table 7. RMS Error in real and imaginary permittivity for each cube and their respective in-plane orientations (O-1 and O-5) and out-pf-plane orientation (O-4). LCB=Low Contrast Biaxial. LCU=Low Contrast Uniaxial. HCU=High Contrast Uniaxial.

	Permittivity (real)	**Permittivity (imaginary)**
Teflon VV	1.955 ± 0.547 (28%)	0.00442 ± 0.0027 (61%)
Teflon HH	2.036 ± 0.466 (23%)	0.00214 ± 0.0050 (234%)
LCB O-1	1.765 ± 0.360 (20.4%)	0.067 ± 0.033 (49.3%)
LCB O-5	2.012 ± 0.308 (15.3%)	0.046 ± 0.029 (63.0%)
LCB O-4	2.435 ± 0.357 (14.7%)	0.079 ± 0.046 (58.2%)
LCU O-1	2.286 ± 0.237 (10.4%)	0.059 ± 0.029 (49.2%)
LCU O-5	2.344 ± 0.054 (2.3%)	0.043 ± 0.048 (111%)
LCU O-4	2.410 ± 0.114 (4.7%)	0.072 ± 0.023 (31.9%)
HCU O-1	2.975 ± 0.002 (0.07%)	0.213 ± 0.009 (4.2%)
HCU O-5	2.738 ± 0.009 (0.33%)	0.202 ± 0.013 (6.4%)
HCU O-4	5.598 ± 0.135 (2.4%)	0.478 ± 0.049 (10.3%)

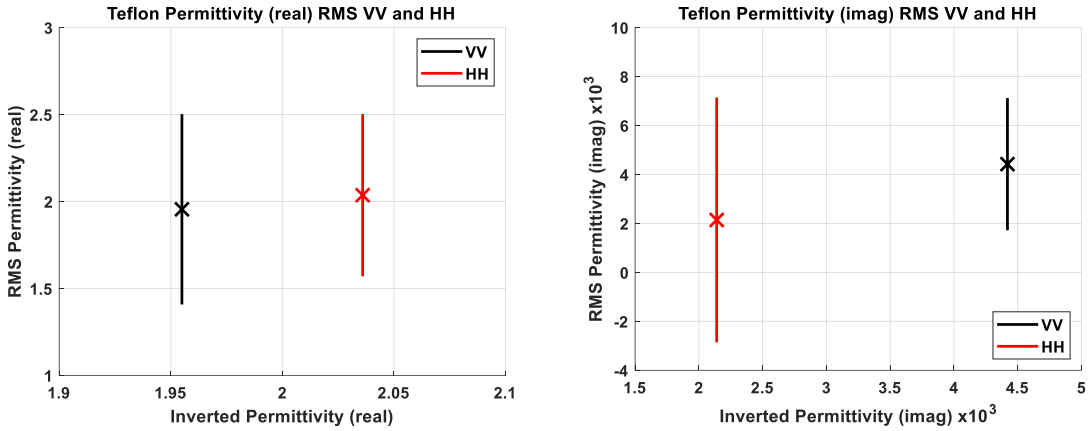

Figure 59. Teflon permittivity uncertainty bounds real (left) and imaginary (right) at 8 GHz for VV and HH polarizations.

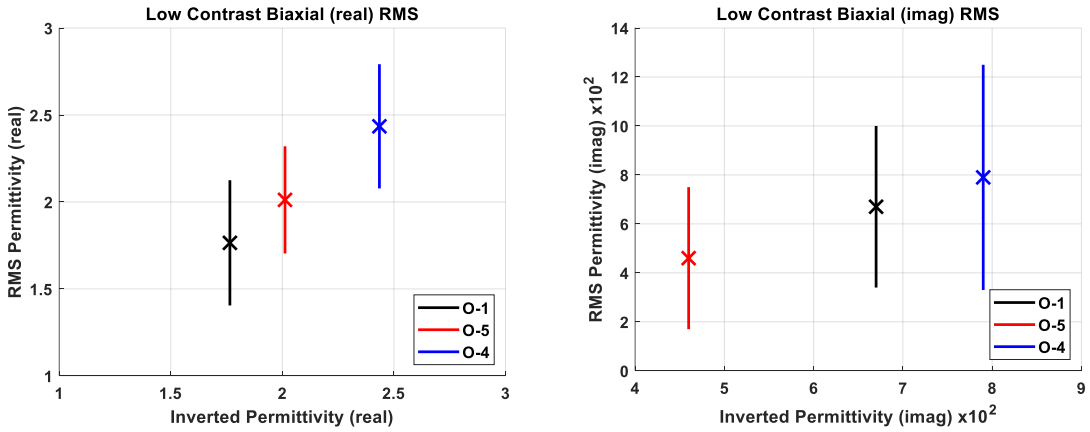

Figure 60. Low contrast biaxial permittivity uncertainty bounds real (left) and imaginary (right) at X-band for O-1, O-5, and O-4 orientations.

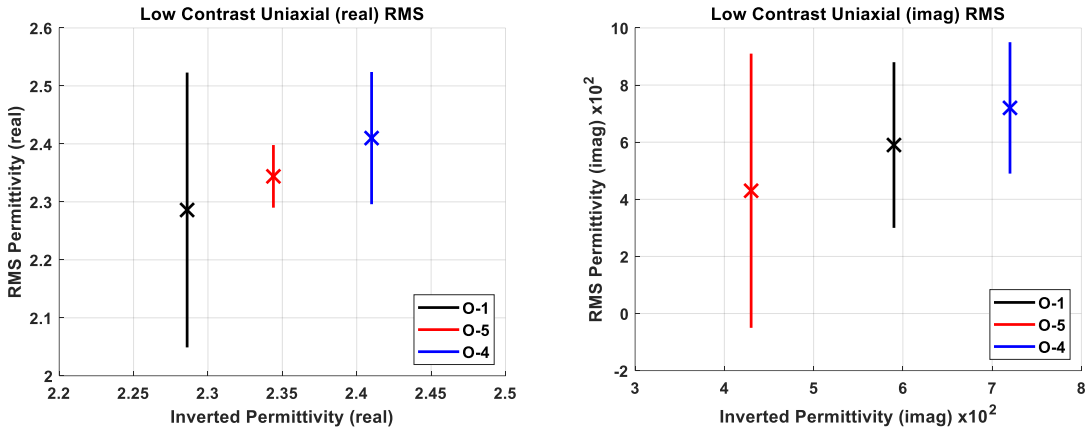

Figure 61. Low contrast uniaxial permittivity uncertainty bounds real (left) and imaginary (right) at X-band for O-1, O-5, and O-4 orientations.

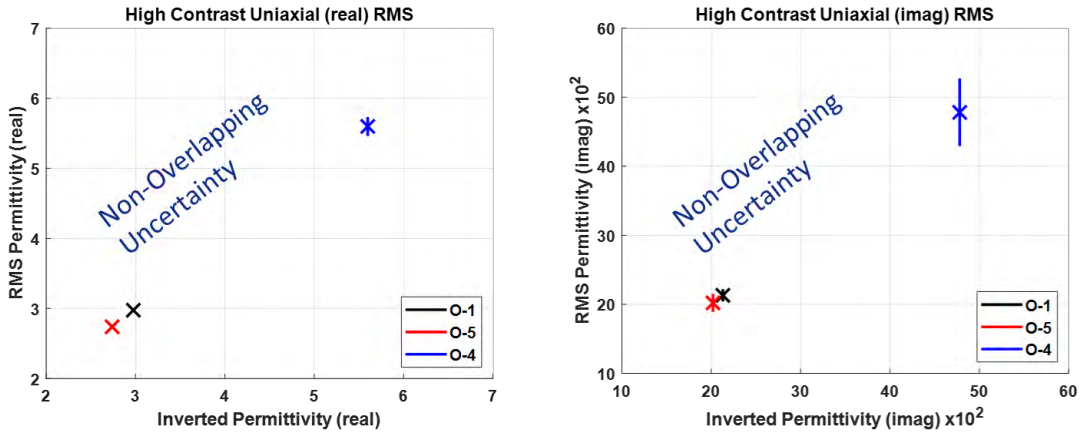

Figure 62. High Contrast uniaxial permittivity uncertainty bounds real (left) and imaginary (right) at X-band for O-1, O-5, and O-4 orientations.

Error Comparison with Focused Beam System

Apart from the current research, two additional free space methods are the focused beam system (FBS) and the absorber-lined transmission tunnel as shown in Figure 63 and Figure 64 respectively.

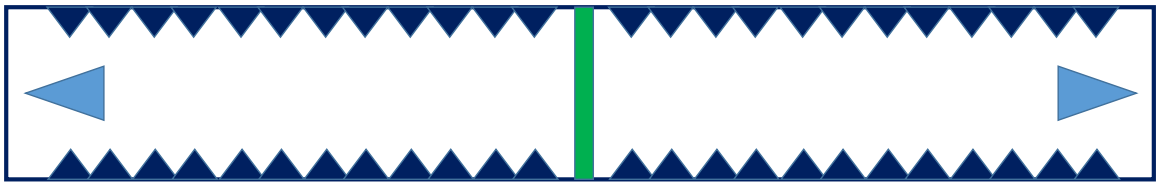

Figure 63. Notional absorber-lined transmission tunnel.

Figure 64. Typical focused beam system (FBS) configuration showing lenses, feed antennas, and sample mounting structure (left). Same system showing material coupon mounted within support frame (right). Used by permission. Photo courtesy of the Compass Technology

While neither of these methods offer full plane wave illumination of a bulk material such as cubes or spheres, they are the closest method available to compare error estimates. The transmission tunnel has no formal definition or design parameters within the material measurement community, and the efficacy of this system is dependent on a number of variables such as antenna beamwidth, cross-sectional area of the tunnel with respect to wavelength, distance to sample, and type and placement of absorber. Due to the lack of uniformity in the use of the transmission tunnel, errors related to the FBS will be considered in comparison to the current research.

The FBS is a two-port S-parameter measurement technique whose structure is comprised of two sets of dielectric lenses, each fed by an independent source antenna [33].

The lenses create a shaped Gaussian beam whose "Gaussian waist" [35] halfway between the lenses provides a non-uniform planewave in that single plane transverse to the direction of propagation. The amplitude distribution of the Gaussian aperture decays to about -20 dB at the sample edges compared to the peak at the center of the Gaussian waist. The FBS is designed to illuminate flat panel sheets whose thickness is less than ½-wavelength in the material. While the current research relies on accurate measurements of RCS, the FBS is dependent on accurate measurements of forward and reverse S-parameter magnitude and phase.

Schultz [33] has provided a RMS error estimate for the FBS based on errors in network analyzer magnitude and phase for forward and reverse S-parameters S_{11} and S_{21} and sample thickness errors. Applying (4.4) and (4.5), Schultz states the FBS RMS error as

$$\delta\epsilon = \sqrt{\begin{array}{c}\left(\left|\frac{\partial\epsilon}{\partial|S_{11}|}\delta|S_{11}|\right|\right)^2 + \left(\left|\frac{\partial\epsilon}{\partial|\Phi_{11}|}\delta|\Phi_{11}|\right|\right)^2 + \left(\left|\frac{\partial\epsilon}{\partial|S_{21}|}\delta|S_{21}|\right|\right)^2 + \cdots \\ \left(\left|\frac{\partial\epsilon}{\partial|\Phi_{21}|}\delta|\Phi_{21}|\right|\right)^2 + \left(\left|\frac{\partial\epsilon}{\partial|t|}\delta|t|\right|\right)^2,\end{array}} \tag{4.7}$$

where $\delta\epsilon$ is the RMS in complex permittivity[16], $|S_{11}|$ is the magnitude of the complex reflection S-parameter S_{11}, Φ_{11} is the phase of the complex reflection S-parameter S_{11}, $|S_{21}|$ is the magnitude of the complex reflection S-parameter S_{21}, Φ_{21} is the phase of the complex reflection S-parameter S_{21}, and t is the material thickness. Assuming a thickness error of ±0.0127 mm, phase error of ±0.2 degrees, and an amplitude error of ±0.5% plus an absolute error of 0.001. Using a representative permittivity $\epsilon_r = 3 - j0.01$,

[16] Separable for individual estimated of ϵ_r' and ϵ_r''.

Schultz estimates an average RMS error for a sample thickness of ¼-wavelength of 0.6% (real) and 100% (imaginary). The errors increase dramatically as the sample thickness approaches ½-wavelength as predicted.

It is clear from the uncertainty analysis for both the FBS and current method, that the FBS has lower uncertainties than the current method, especially for low permittivity and low loss materials. However, the FBS is not suited for thick anisotropic structures, and another method, such as the one presented here, provides full-body plane wave illumination at multiple angles of incidence and polarizations. This cannot be found in any other current method of anisotropic estimation. With increased control over mounting structure coupling and revised calibration schemes that provide a more predictable alignment with the incident field, the method of characterizing anisotropic materials using scattered fields has the capacity to significantly reduce uncertainties and find application in a variety of contexts.

V. Conclusion

5.1 Discussion

A free space method for estimating anisotropic material parameters using scattered field measurements has been presented. The method, an extension of the work of Knisely who measured the anisotropic properties of dielectric cubes in waveguide, utilized monostatic RCS measurements of those same cubes in a free space far-zone context. The method was first applied to a series of dielectric spheres to identify major contributors of error in the far field context and to show that quality inversions of isotropic materials was possible prior to venturing into anisotropic territory. A Monte Carlo uncertainty analysis of the sphere permittivity and loss tangent estimates was performed resulting in errors of 0.04-2.53% for permittivity (real) and from 6-278% for loss tangent estimates. A fundamental conclusion here was that inversion uncertainty was exaggerated for low loss materials but greatly reduced for high loss materials, a conclusion that is relevant for anisotropic cubes as well.

The research made the following contributions to the material measurement community:

- Extension of biaxial estimation to a free-space far-field context.
- Established biaxial estimation uncertainty for real and imaginary components.
- Identified conditions for non-overlapping uncertainty among anisotropic axes.
- Demonstrated isotropic inversion of anisotropic axes.
- Defined use of azimuth- and frequency-dependent scattering information.
- Demonstrated biaxial inversion without complex hardware or costly facilities.

The method successfully estimated the dielectric constant of isotropic, uniaxial, and biaxial cubes at X-band. For isotropic inversion, measured azimuth-dependent RCS data was utilized, while for anisotropic inversion, measured frequency-dependent RCS data was used. In direct comparisons with Knisely biaxial data, the real permittivity varied from 5.9%-9.4% for the in-plane axes and 7% for the out-of-plane axis. The imaginary permittivity demonstrated high variance from Knisely showing 13.2%-81.1% for the in-plane axes and 43.6% for the out-of-plane axis.

An uncertainty RMS estimate identified significant error margins for low loss materials such as Teflon, indicating that this method is not suitable in those cases. However, the same uncertainty analysis revealed that for larger loss materials, error margins were driven down as low as 2.4% in the case of the high contrast uniaxial cube (O-4), making this method a suitable candidate for permittivity estimation in those instances.

The research demonstrated the artificial media measured by Knisely in waveguide proved sufficiently large as an array of occlusions in the finite context. In addition, inversions of the anisotropic axes under isotropic assumptions proved especially helpful for two reason. First, a complex plane optimization for two unknown variables (i.e. permittivity real and imaginary for one axis) is far more efficient than a complete biaxial inversion with six unknown terms. Such an inversion takes multiple days without the guarantee of a unique solution. The second reason is that the apparent lack of mutual coupling between tensor axes has implications for additive manufacturing of anisotropic samples – especially when printing occlusions which may have edges, corners, and points. Such geometric features become costly to print with respect to time and equipment

complexity when the radii of these geometric features are forced to be more restrictive than necessary.

Finally, the method demonstrated that estimates of high loss biaxial permittivity is possible using monostatic RCS measurements without the need for complex hardware or access to costly facilities.

5.2 Future Work

Numerous efforts have been reported on artificial dielectric arrays. These designs would be aided by using a validation test bed for estimating their effective permittivity. The current measurement configuration and inversion scheme is ideal for such a validation test bed.

The use of honeycomb "core" is commonplace in aircraft design. Core is by its very design is an anisotropic structure. Coating all surfaces of these cores with carbon-based materials, commonly referred to as "loaded core," creates entirely new anisotropic absorbing structures. Measuring the RCS of these loaded cores in concert with the permittivity estimation technique presented here would provide a useful tool in optimizing the loading process.

The presence of a target support is a principle source of error in this research. The use of inverted Stewart platforms (string support systems) are used by some RCS test ranges to support targets by means support strings, thus mitigating coupling between the target and support structure. A small version of what is used in the RCS measurement community would provide a means of supporting anisotropic cubes and other shapes without the presence of coupling errors.

This work focused on the use of spheres and cubes because their local coordinate systems lent themselves to inversions that could readily be adapted to their coordinate systems (i.e. Mie series, isolated tensor inversions). In addition, these shapes were the first step in seeking the permittivity of more complex shapes. The use of alternative shapes or unknown tensor axis orientations would require adaptation of the current inversion scheme to accommodate these new coordinate systems and provide a next step toward arbitrary-shaped inversions.

The measurement of sample S-parameters in a waveguide provides an infinite sample context. This context constrains the incident field to the excitation of a single tensor axis at one time. In the free space context, the finite nature of the target imposes currents radiating in all directions, causing coupling between the tensor axes. This is not a result of off-diagonal tensor elements, but the simple realization that corners and edges radiate in all directions, regardless of the direction of the source within the material. A rigorous treatment of this coupling would provide insight into how much variance between measured and predicted results is from axis coupling and other error sources.

The current research focused on the scattered fields from isolated targets. However, by coating a variety of canonical shapes with unknown materials in concert with FEKO or other suitable forward solvers, the complex scattered fields may be used to identify the permittivity, permeability, and other electromagnetic scattering behaviors.

Finally, the current research focused on monostatic RCS measurements as the data engine for inversions, where a future approach may focus on bistatic RCS measurements that may offer additional independent information toward successful inversions.

Appendix: Inversion Convergence History

The inversion convergence history for Teflon, low contrast uniaxial, high contrast uniaxial, and low contrast biaxial cubes and their respective orientations is shown in Figure 65, Figure 66, Figure 67 and Figure 68 respectively.

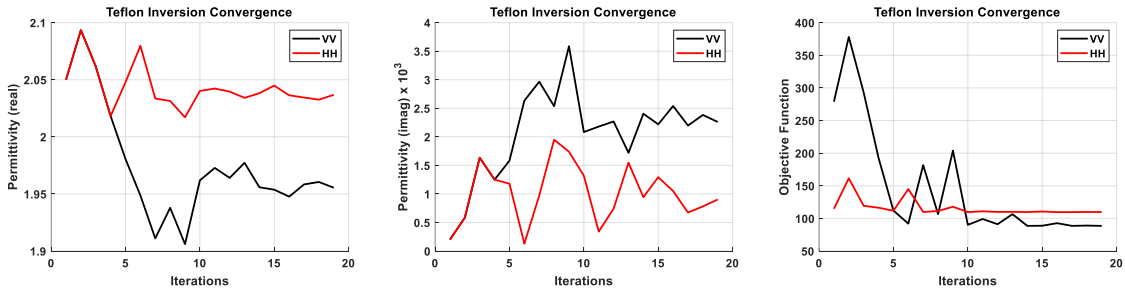

Figure 65. Teflon inversion convergence history under VV and HH polarizations for real permittivity (left), imaginary permittivity (middle), and the inversion objective function (right).

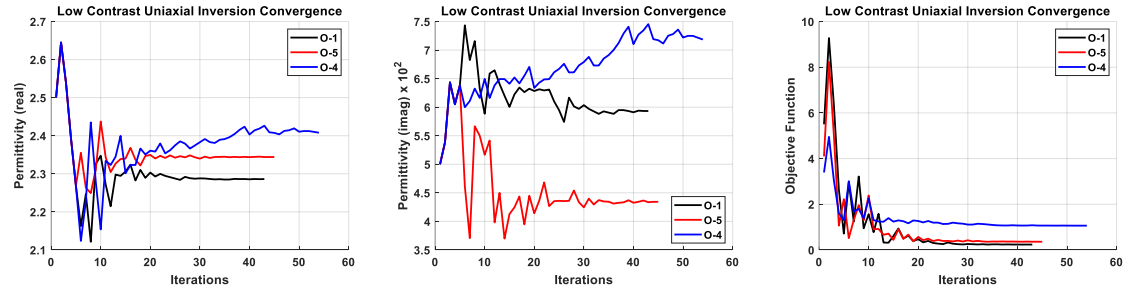

Figure 66. Low contrast uniaxial inversion convergence history for orientations O-1, O-5, and O-4 for real permittivity (left), imaginary permittivity (middle), and the inversion objective function (right).

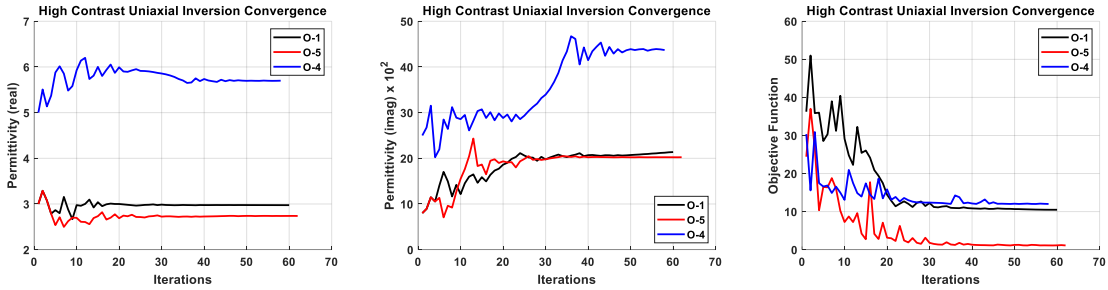

Figure 67. High contrast uniaxial inversion convergence history for orientations O-1, O-5, and O-4 for real permittivity (left), imaginary permittivity (middle), and the inversion objective function (right).

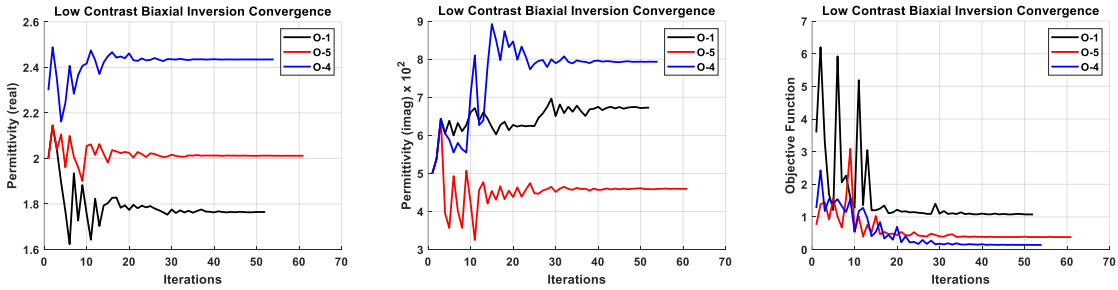

Figure 68. Low contrast biaxial inversion convergence history for orientations O-1, O-5, and O-4 for real permittivity (left), imaginary permittivity (middle), and the inversion objective function (right).

Bibliography

[1] T. Cui, "Microwave metamaterials," *National Science Review,* vol. 5, pp. 134-136, 03/01 2018, doi: 10.1093/nsr/nwx133.

[2] M. J. Havrilla, "The Effect of Symmetry on Material Property Tensors," in *Material Measurement Working Group (MMWG)*, Boulder, CO., 7-8 May 2014 2014, Wright Patterson AFB, OH 45433, 2014.

[3] A. G. Knisely, "Biaxial Anisotropic Material Development and Characterization using Rectangular to Square Waveguide," Master of Science in Electrical Engineering Thesis, Department of Electrical and Computer Engineering, Air Force Institute of Technology, Wright Patterson Air Force Base, AFIT-ENG-MS-15-M-055, 2015. [Online]. Available: https://scholar.afit.edu/etd/40

[4] A. K. Amert and K. W. Whites, "Characterization of small specimens using an integrated computational/measurement technique," in *2013 IEEE Antennas and Propagation Society International Symposium (APSURSI)*, 7-13 July 2013 2013, pp. 706-707, doi: 10.1109/APS.2013.6711013.

[5] M. M. Scott, D. L. Faircloth, J. A. Bean, and S. G. Holliday, "Biaxial Permittivity Determination for Electrically Small Material Specimens of Complex Shape Using Shorted Rectangular Waveguide Measurements," *IEEE Transactions on Instrumentation and Measurement,* vol. 63, no. 4, pp. 896-903, 2014, doi: 10.1109/tim.2013.2289081.

[6] J. Baker-Jarvis, M. D. Janezic, and D. C. Degroot, "High-frequency dielectric measurements," *IEEE Instrumentation & Measurement Magazine,* vol. 13, no. 2, pp. 24-31, 2010, doi: 10.1109/MIM.2010.5438334.

[7] K. Y. You, F. B. Esa, and Z. Abbas, "Macroscopic characterization of materials using microwave measurement methods — A survey," in *2017 Progress in Electromagnetics Research Symposium - Fall (PIERS - FALL)*, 19-22 Nov. 2017 2017, pp. 194-204, doi: 10.1109/PIERS-FALL.2017.8293135.

[8] A. G. Knisely, "A Measurement Exploration of Additively Manufactured Media," presented at the Material Measurment Working Group (MMWG), Santa Rosa, CA., 2021.

[9] E. Knott and T. B. Senior, "How far is far?," *IEEE Transactions on Antennas and Propagation,* vol. 22, no. 5, pp. 732-734, 1974, doi: 10.1109/TAP.1974.1140880.

[10] R. G. Kouyoumjian and L. Peters, "Range requirements in radar cross-section measurements," *Proceedings of the IEEE,* vol. 53, no. 8, pp. 920-928, 1965, doi: 10.1109/PROC.1965.4070.

[11] J. Baker-Jarvis *et al.*, "Dielectric characterization of low-loss materials a comparison of techniques," *IEEE Transactions on Dielectrics and Electrical Insulation,* vol. 5, no. 4, pp. 571-577, 1998, doi: 10.1109/94.708274.

[12] J. Baker-Jarvis, E. J. Vanzura, and W. A. Kissick, "Improved technique for determining complex permittivity with the transmission/reflection method," *IEEE Transactions on Microwave Theory and Techniques,* vol. 38, no. 8, pp. 1096-1103, 1990, doi: 10.1109/22.57336.

[13] H. E. Bussey, "Measurement of RF properties of materials, A survey," *Proceedings of the IEEE,* vol. 56, no. 4, pp. 729-729, 1968, doi: 10.1109/PROC.1968.6359.

[14] L. F. Chen, C. K. Ong, C. P. Neo, V. V. Varadan, and V. K. Varadan, *Microwave electronics: Measurement and materials characterization*. Hoboken, NJ: Wiley-Blackwell, 2004.

[15] M. N. Afsar, J. R. Birch, R. N. Clarke, and G. W. Chantry, "The measurement of the properties of materials," *Proceedings of the IEEE,* vol. 74, no. 1, pp. 183-199, 1986, doi: 10.1109/PROC.1986.13432.

[16] A. M. Nicolson and G. F. Ross, "Measurement of the Intrinsic Properties of Materials by Time-Domain Techniques," *IEEE Transactions on Instrumentation and Measurement,* vol. 19, no. 4, pp. 377-382, 1970, doi: 10.1109/TIM.1970.4313932.

[17] W. B. Weir, "Automatic measurement of complex dielectric constant and permeability at microwave frequencies," *Proceedings of the IEEE,* vol. 62, no. 1, pp. 33-36, 1974, doi: 10.1109/PROC.1974.9382.

[18] W. Swarner and L. Peters, "Radar cross sections of dielectric or plasma coated conducting spheres and circular cylinders," *IEEE Transactions on Antennas and Propagation,* vol. 11, no. 5, pp. 558-569, 1963, doi: 10.1109/TAP.1963.1138087.

[19] L. Peters, T. Kawano, and W. G. Swarner, "Approximations for dielectric or plasma scatterers," *Proceedings of the IEEE,* vol. 53, no. 8, pp. 882-892, 1965, doi: 10.1109/PROC.1965.4067.

[20] R. Abbato, "Dielectric constant measurements using RCS data," *Proceedings of the IEEE,* vol. 53, no. 8, pp. 1095-1097, 1965, doi: 10.1109/PROC.1965.4101.

[21] C. A. Balanis, "Advanced engineering electromagnetics." Hoboken, N.J.: John Wiley & Sons, 2012, p. 661.

[22] J. D. Young, "Constitutive Parameter Measurements Using the Scattering Technique," National Aeronautics and Space Administration, Washington, D.C., 6 Feb 1967.

[23] J. S. Yu and L. J. Peters, "Measurement of constitutive parameters using the Mie solution of a scattering sphere," *Proceedings of the IEEE,* vol. 58, no. 6, pp. 876-885, 1970, doi: 10.1109/PROC.1970.7795.

[24] M. Ishikawa and H. Shirai, "Non-contacting Estimation of Complex Permittivity Using RCS Measurement," 2009.

[25] C. Hu, J. Xu, N. Li, and L. Zhang, "Signal processing techniques in high-resolution RCS measurement system," in *2009 4th IEEE Conference on Industrial Electronics and Applications*, 25-27 May 2009 2009, pp. 586-588, doi: 10.1109/ICIEA.2009.5138216.

[26] J. A. Kong, *Electromagnetic wave theory*. New York: Wiley (in English), 1986.

[27] R. E. Collin, "A Simple Artificial Anisotropic Dielectric Medium," *IRE Transactions on Microwave Theory and Techniques,* vol. 6, no. 2, pp. 206-209, 1958, doi: 10.1109/TMTT.1958.1124539.

[28] C. Eyraud, J. Geffrin, A. Litman, and H. Tortel, "Complex Permittivity Determination From Far-Field Scattering Patterns," *IEEE Antennas and Wireless Propagation Letters,* vol. 14, pp. 309-312, 2015, doi: 10.1109/LAWP.2014.2362995.

[29] E. Perret, "Permittivity characterization based on Radar Cross measurements," in *2016 URSI International Symposium on Electromagnetic Theory (EMTS)*, 14-18 Aug. 2016 2016, pp. 457-460, doi: 10.1109/URSI-EMTS.2016.7571425.

[30] H. Saleh, H. Tortel, C. Leroux, A. Coudreuse, A. Litman, and J. M. Geffrin, "Approach to Control Permittivity and Shape of Centimeter-Sized Additive Manufactured Objects: Application to Microwave Scattering Experiments," *IEEE Transactions on Antennas and Propagation,* vol. 69, no. 2, pp. 983-991, 2021, doi: 10.1109/TAP.2020.3016159.

[31] R. E. Collin, "Field Theory of Guided Waves." Institute of Electrical and Electronics Engineers: New York, 1991, pp. 749-786.

[32] Y. Hollander and R. Shavit, "Constitutive parameter extraction and experimental validation of single and double negative metamaterials," *Microwaves, Antennas & Propagation, IET,* vol. 5, pp. 84-94, 02/12 2011, doi: 10.1049/iet-map.2010.0024.

[33] J. W. Schultz, *Focused beam methods : measuring microwave materials in free space*. (in English), 2012.

[34] N. A. O'Gorman and M. J. Havrilla, "Biaxial Material Characterization Utilizing A Focus Beam System," in *2020 International Symposium on Electromagnetic Compatibility - EMC EUROPE*, 23-25 Sept. 2020 2020, pp. 1-4, doi: 10.1109/EMCEUROPE48519.2020.9245835.

[35] L. E. R. Petersson and G. S. Smith, "An estimate of the error caused by the plane-wave approximation in free-space dielectric measurement systems," *IEEE Transactions on Antennas and Propagation,* vol. 50, no. 6, pp. 878-887, 2002, doi: 10.1109/TAP.2002.1017671.

[36] M. W. Hyde, M. J. Havrilla, and H. M. Chizever, "Permittivity and Permeability Errors Due to Misalignment and Phase Aberrations Using S21 with Angle Diversity in a Free-Space Measurement System," presented at the Material Measurements Working Group (MMWG), U. S. Air Force Acedemy, 6-7 May, 2015.

[37] J. Baker-Jarvis, M. Janezic, B. Riddle, C. Holloway, N. Paulter, and J. Blendell, "Dielectric and Conductor-Loss Characterization and Measurements on Electronic Packaging Materials," in "NIST Technical Note (NIST TN)," Gaithersburg, MD, 2001. Accessed: 18 July 2021. [Online]. Available: https://doi.org/10.6028/NIST.TN.1520

[38] J. A. Berrie and G. L. Wilson, "Design of target support columns using EPS foam," *IEEE Antennas and Propagation Magazine,* vol. 45, no. 1, pp. 198-206, 2003, doi: 10.1109/MAP.2003.1189667.

[39] A. R. v. Von Hippel, "Dielectric materials and applications." Boston: Artech House, 1995, sec. Tables of Dielectric Materials.

[40] T. C. Edwards and M. B. Steer, "Foundations for microstrip circuit design." West Sussex, UK: John Wiley & Sons, 2016, p. 636.

[41] Z. Ahmad, "Dielectric material," M. A. Silaghi Ed. Rijeka, Croatia; Intech, 2012, ch. 1, p. 13.

[42] J. Rheinstein, "Backscatter from spheres: A short pulse view," *IEEE Transactions on Antennas and Propagation,* vol. 16, no. 1, pp. 89-97, 1968, doi: 10.1109/TAP.1968.1139116.

[43] H. Thal, "Exact circuit analysis of spherical waves," *IEEE Transactions on Antennas and Propagation,* vol. 26, no. 2, pp. 282-287, 1978, doi: 10.1109/TAP.1978.1141822.

[44] P. Affolter and B. Eliasson, "Electromagnetic Resonances and Q-Factors of Lossy Dielectric Spheres," *IEEE Transactions on Microwave Theory and Techniques,* vol. 21, no. 9, pp. 573-578, 1973, doi: 10.1109/TMTT.1973.1128073.

[45] D. C. Tzarouchis, P. Ylä-Oijala, and A. Sihvola, "Resonant Scattering Characteristics of Homogeneous Dielectric Sphere," *IEEE Transactions on Antennas and Propagation,* vol. 65, no. 6, pp. 3184-3191, 2017, doi: 10.1109/TAP.2017.2690312.

[46] B. M. Welsh, W. D. Muller, and B. M. Kent, "Air Force Research Laboratory advanced compact range RCS uncertainty analysis for a general target," *IEEE Antennas and Propagation Magazine,* vol. 45, no. 3, pp. 195-201, 2003, doi: 10.1109/MAP.2003.1232185.

[47] G. Wilson, W. Muller, and B. Welsh, *Approaches to Signature Measurement Uncertainty Analysis*. 2008.

[48] "IEEE Recommended Practice for Radar Cross-Section Test Procedures," *IEEE Std 1502-2020 (Revision of IEEE Std 1502-2007),* pp. 1-78, 2020, doi: 10.1109/IEEESTD.2020.9310748.

[49] S. Vijayakumaran. "Circularly Symmetric Gaussian Random Vectors.pdf." Department of Electrical Engineering Indian Institute of Technology Bombay. https://www.ee.iitb.ac.in/~sarva/courses/EE703/2013/Slides/CircularlySymmetricGaussian.pdf (accessed 21 July, 2021).

[50] W. R. Griffin, H. M. Chizever, and P. A. Zidek, "Advanced RCS Measurements Range Final Report," no. MRC-R-DN-94-005, p. 135, March 1993.

[51] B. P. Lathi, "Linear systems and signals." New York; Oxford: Oxford University Press, 2010, sec. Fourier Analysis of Discrete-Time Signals, pp. 885-889.

[52] G. J. Matyas and B. J. Kelsall. "Practical Consideration for Effective Software Gating in High Resolution RCS Measurements." Antenna Measurement Techniques Association (AMTA). https://www.amta.org/i4a/doclibrary/index.cfm?pageid=3352&showTitle=1 (accessed 22 July, 2021).

[53] M. W. Hyde, "Reproducing" Agilent E8362B Time-Domain Measurements," presented at the Material Measurements Working Group (MMWG), Michigan State University, 2016.

[54] C. W. Trueman, S. R. Mishra, C. L. Larose, and M. Flynn. "Application of Prony's Method to Software Gating." Antenna Measurement Techniques Association (AMTA). https://www.amta.org/i4a/doclibrary/index.cfm?pageid=3352&showTitle=1 (accessed 22 July, 2021).

[55] Z. Chen and Z. Xiong, "Mitigation of Band Edge Effects in Fourier Transform Based Time Domain Gating," in *2019 13th European Conference on Antennas and Propagation (EuCAP)*, 31 March-5 April 2019 2019, pp. 1-5.

[56] J. Dunsmore, "Gating effects in time domain transforms," in *2008 72nd ARFTG Microwave Measurement Symposium*, 9-12 Dec. 2008 2008, pp. 1-8, doi: 10.1109/ARFTG.2008.4804303.

REPORT DOCUMENTATION PAGE

Form Approved OMB No. 074-0188

PLEASE DO NOT RETURN YOUR FORM TO THE ABOVE ADDRESS.

1. REPORT DATE *(DD-MM-YYYY)*	2. REPORT TYPE	3. DATES COVERED *(From – To)*
16-09-2021	PhD Dissertation	October 2013 – September 2021

TITLE AND SUBTITLE

Characterization of Anisotropic Materials using Scattered Field Measurements

5a. CONTRACT NUMBER

5b. GRANT NUMBER

5c. PROGRAM ELEMENT NUMBER

6. AUTHOR(S)

Chizever, Hirsch M.

5d. PROJECT NUMBER

5e. TASK NUMBER

5f. WORK UNIT NUMBER

7. PERFORMING ORGANIZATION NAMES(S) AND ADDRESS(S)

Air Force Institute of Technology
Graduate School of Engineering and Management (AFIT/EN)
2950 Hobson Way
Wright-Patterson AFB, OH 45433-7765

8. PERFORMING ORGANIZATION REPORT NUMBER

AFIT-ENG-DS-21-S-004

9. SPONSORING/MONITORING AGENCY NAME(S) AND ADDRESS(ES)

Intentionally left blank

10. SPONSOR/MONITOR'S ACRONYM(S)

11. SPONSOR/MONITOR'S REPORT NUMBER(S)

12. DISTRIBUTION/AVAILABILITY STATEMENT

DISTRUBTION STATEMENT A. APPROVED FOR PUBLIC RELEASE; DISTRIBUTION UNLIMITED.

13. SUPPLEMENTARY NOTES

This research uses monostatic far-zone scattered field measurements to estimate the permittivity of anisotropic materials at X-band. Utilizing Radar Cross Section (RCS) measurement techniques, this effort examines the efficacy of whole-sample TEM illumination in the estimation of anisotropic permittivity, in contrast with traditional subsample illumination methods. The research examines the impact that dielectric supports have on measurement error and uncertainty in permittivity estimates. Following an incremental approach, the research first demonstrates successful estimation of permittivity for isotropic spheres followed by a Teflon isotropic cube. Finally, the method is applied to uniaxial and biaxial cubes whose anisotropic permittivity is validated through comparisons with published data. The method showed success for a material with high contrast between tensor axes but had increased uncertainty with materials of low real and imaginary permittivity. The research also indicated that uncertainty increases in lower loss tangent estimates due to mutual coupling between the dielectric support structure and the material under test. Finally, the method demonstrated that estimates of lossy biaxial permittivity is possible in a free space far-field context without the use of costly measurement facilities or complex hardware.

15. SUBJECT TERMS

Radar Cross Section (RCS), permittivity, inversion, anisotropy

16. SECURITY CLASSIFICATION OF:			17. LIMITATION OF ABSTRACT	18. NUMBER OF PAGES	19a. NAME OF RESPONSIBLE PERSON
a. REPORT	b. ABSTRACT	c. THIS PAGE			Dr. Peter J. Collins, AFIT/ENG
U	U	U	UU	125	19b. TELEPHONE NUMBER *(Include area code)* (937) 255-3636, ext 7256 (peter.collins@afit.edu)

Standard Form 298 (Rev. 8-98)
Prescribed by ANSI Std. Z39-18